### This electronic thesis or dissertation has been downloaded from the King's Research Portal at https://kclpure.kcl.ac.uk/portal/



# Development of a high-resolution, MRI-compatible PET detector using digital silicon photomultipliers

Düppenbecker, Peter Michael Jakob

Awarding institution: King's College London

The copyright of this thesis rests with the author and no quotation from it or information derived from it may be published without proper acknowledgement.

END USER LICENCE AGREEMENT



Unless another licence is stated on the immediately following page this work is licensed

under a Creative Commons Attribution-NonCommercial-NoDerivatives 4.0 International

licence. https://creativecommons.org/licenses/by-nc-nd/4.0/

You are free to copy, distribute and transmit the work

Under the following conditions:

- Attribution: You must attribute the work in the manner specified by the author (but not in any way that suggests that they endorse you or your use of the work).
- Non Commercial: You may not use this work for commercial purposes.
- No Derivative Works You may not alter, transform, or build upon this work.

Any of these conditions can be waived if you receive permission from the author. Your fair dealings and other rights are in no way affected by the above.

### Take down policy

If you believe that this document breaches copyright please contact <u>librarypure@kcl.ac.uk</u> providing details, and we will remove access to the work immediately and investigate your claim.

### Development of a high-resolution, MRI-compatible PET detector using digital silicon photomultipliers

### Peter Michael Jakob Düppenbecker

Thesis submitted for the degree of Doctor of Philosophy

King's College London Imaging Sciences & Biomedical Engineering January 2016

## Table of contents

	Abstract	5
	Acknowledgements	6
	List of figures	7
	List of tables	9
	Acronyms	10
1	<ul> <li>1.1 Hybrid imaging and the advent of simultaneous PET/MRI</li> <li>1.2 Thesis scope and structure</li> <li>1.3 Contributions</li> </ul>	<b>12</b> 12 14 15 16
2	2.1       Positron emission tomography         2.1.1       Basic measurement principle and limits	<b>19</b> 19 20 23
	2.2 Magnetic resonance imaging	$\begin{array}{c} 27\\ 27\end{array}$
	2.3Engineering challenges of simultaneous PET/MRI2.3.1Interference with the MRI static magnetic field2.3.2Interference with the MRI gradient system2.3.3Radio frequency interference between PET and MRI system2.3.4Gamma transparency2.3.5Confined construction space	30 31 32 33 34 34
	2.4 The digital SiPM	36 38 40
3	<ul> <li>3.1 Introduction</li></ul>	<ul> <li>44</li> <li>44</li> <li>48</li> <li>51</li> <li>51</li> <li>51</li> <li>52</li> </ul>

	3.5	Results	53
		3.5.1 $B_0$ distortions caused by detector stack	53
		3.5.2 $B_0$ influence on detector stack	
		3.5.3 Gradient influence on detector stack	
		3.5.4 RF interference	
	3.6	Discussion	
	3.7	Conclusion	
	0.1		00
4	Dev	elopment and characterization of a gradient-transparent	
	carb	oon fibre composite RF shield for simultaneous PET/MRI	65
	4.1	Introduction	65
	4.2	Fabrication of carbon fibre RF enclosures	68
		4.2.1 Material selection	68
		4.2.2 The lamination process	69
	4.3	Theoretical considerations of shielding efficiency and eddy currents	72
		4.3.1 Shielding efficiency	
		4.3.2 Transmission theory of shielding	73
		4.3.3 Influence of material parameters	75
		4.3.4 Eddy currents	
		4.3.5 Shielding efficiency versus eddy currents	79
	4.4	Experimental verification	
		4.4.1 Quantification of shielding efficiency in the MRI frequency range.	
		4.4.2 Materials and methods	
		4.4.3 Results	85
	4.5	Analysis and modelling	
	1.0	4.5.1 Analysis range	
		4.5.2 Modelling	
		4.5.3 Comparison to measurement data	
		4.5.4 Shielding efficiency versus sheet conductance	
	4.6	Conclusion	
	4.7	Outlook	
	1.1	Outlook	00
5	Opt	ical design of high-resolution	
	dep	th-of-interaction scintillation detectors	101
	5.1	Introduction	101
	5.2	Feasibility study of dual-layer, pixelated scintillation	
		detectors using a digital SiPM and single-sided readout	105
		5.2.1 Introduction	105
		5.2.2 Experimental investigation	106
		5.2.3 Results	
		5.2.4 Discussion	
	5.3	A method for measuring the sub-channel light distribution	
		of digital SiPM based scintillation detectors	112
		5.3.1 Introduction	
		5.3.2 Measurement method and application	
		5.3.3 Results	
		5.3.4 Discussion	
	5.4	Optical simulation of pixelated scintillation detectors	
	J. 1	5.4.1 Introduction	
		5.4.2 Main challenges of optical simulations	

		5.4.3	Practical assessment of optical simulations	123
		5.4.4	Discussion	125
	5.5	Reflect	corless pixelated scintillator arrays	127
		5.5.1	Introduction	127
		5.5.2	Methods	128
		5.5.3	Results	130
		5.5.4	Discussion	132
	5.6	Conclu	sion	134
6	Con	clusion		137
	6.1	Empiri	ical findings	137
	6.2	Furthe	r research and development prospectives	140
	6.3	Outloo	bk	141
	Bibli	iograph	у	143

### Abstract

The simultaneous integration of positron emission tomography (PET) and magnetic resonance imaging (MRI) promises to combine superior functional and anatomical information into a single examination, but poses a number of engineering challenges. In particular, the development of MRI-compatible photodetectors is a key issue to realize PET/MRI at its best.

In 2009, a novel photodetector, the so-called digital SiPM, was presented. The digital SiPM combines an array of Geiger-mode photodiodes with a direct digital readout and timestamper on a single silicon die. Its high integration and expected immunity to magnetic fields makes the digital SiPM very promising for simultaneous PET/MRI. Related to the development of the world's first digital SiPM based simultaneous PET/MRI system, this thesis focuses on three specific engineering aspects of simultaneous PET/MRI.

First, an MRI-compatible photodetector stack based on digital SiPMs has been developed, investigated and optimized. The final design is virtually immune to the MRI environment and enables the full potential of the digital SiPM to be used for simultaneous PET/MRI, including its time-of-flight capabilities. No evidence was found that the digital SiPM itself is affected by the MRI environment.

Second, based on carbon fibre composites, a novel modular radio frequency (RF) shielding concept for MRI-compatible PET detectors has been developed. In contrast to common copper based shields, carbon fibre composites are less susceptible to eddy currents because of their lower sheet conductance. It is shown, experimentally and analytically, that carbon fibre composites can provide higher RF shielding efficiency to sheet conductance ratios than conventional copper shields can do, which makes them beneficial for simultaneous PET/MRI.

Third, experimental and simulation approaches for the optical design of pixelated scintillation detectors have been assessed, in particular to improve the depth-ofinteraction encoding of pixelated scintillation detectors. A novel pixelated scintillator configuration is proposed, which avoids the use of inter-crystal reflectors.

### Acknowledgements

This thesis arose in the context of the development of the Hyperion  $II^{D}$  PET/MRI system, the world's first simultaneous PET/MRI system based on digital SiPM technology. It was a fascinating project at the cutting edge of technology that allowed unique insights into the world of medical imaging technologies. Many people contributed to the success of this project — and thus also to the success of this thesis. I would like to thank my colleagues from Philips, RWTH Aachen and King's College London, as well as external project partners for their collaboration. In particular:

Prof. Volkmar Schulz, for getting me started on this project, supervising my thesis, as well as providing me a lot of opportunities to realize own ideas. The core team, Björn Weissler, Pierre Gebhardt, David Schug, Jakob Wehner, Christoph Lerche, Benjamin Goldschmidt, Torsten Solf, André Salomon and Walter Rütten, for their fruitful collaboration and discussions, including the countless hours spent during days, night and weekends in the laboratory to push the project forward.

Wolfgang Renz and Katharina Schumacher, former Irmato Industrial Solutions, for their outstanding collaboration and support in mechanical design and detector assembly, which enabled the rapid conversion of ideas into working prototypes and gave me the opportunity to learn a lot about the pitfalls of mechanical engineering.

Sarah Lodomez, Rainald Haagen and Christopher Anderson, for their support as student worker and master students, which made it possible to investigate and work out ideas outside the project paths.

Hammam Shakhtour, Institute of High Frequency Technology, RWTH Aachen University, for its hospitality and providing most generous access to high frequency measurement equipment.

Prof. Paul Marsden, for supervising my thesis, and in particular for his constant and constructive support to finalize this thesis in the presence of changing research conditions.

Finally, my wife Anne. Your encouragement and outstanding commitment was essential to succeed. Thanks!

The presented work was partially funded by the European Union and the German federal state North Rhine-Westphalia project ForSaTum (grant z0903ht014g), by the Wellcome Trust and EPSRC (grant 088641/Z/09/Z) and the European Union FP7 project SUBLIMA (grant agreement N° 241711).

# List of Figures

2.1	Schematic of positron decay	20
2.2	True and scattered events	21
2.3	Multiple events and the time-of-flight principle	23
2.4	Impact of the parallax error on spatial resolution	25
2.5	Example of a photomultiplier tube	26
2.6	Schematic cross-section of the prevailing PET/MRI system design $\ . \ . \ .$	36
2.7	The DPC-3200-22 digital SiPM	37
2.8	The Hyperion $II^D$ PET/MRI insert	39
2.9	PET detector ring of the Hyperion $II^D$ system $\ldots \ldots \ldots \ldots \ldots \ldots$	39
2.10	Singles detection module	40
2.11	Detector stack and cooling system	41
3.1	MRI-compatible digital SiPM detector stack	45
3.2	Implementation details of the sensor tile and interface board	46
3.3	Functional overview of the detector stack	46
3.4	Test equipment on MRI table and bench top $\hdots \ldots \ldots \ldots \ldots \ldots$	50
3.5	Clocking infrastructure for synchronized laser excitation $\ldots \ldots \ldots$	51
3.6	$B_0$ test setup $\hdots \ldots \ldots$	52
3.7	$B_0$ distortion maps	54
3.8	Directional effect of a 3 T magnetic field on voltage regulators	55
3.9	Gain dependent directional effect of magnetic fields on the bias voltage $% \mathcal{A}$ .	56
3.10	Effect of an induced voltage ripple on the bias voltage $\ldots \ldots \ldots \ldots$	57
3.11	Energy resolution before, after, with and without gradients $\ldots$ .	57
3.12	Timing jitter at start of gradient test sequence	58
3.13	Spectral analysis of timing jitter	58
3.14	Clock jitter with and without gradients $\ldots \ldots \ldots \ldots \ldots \ldots \ldots$	59
3.15	Clock input jitter withhout and with gradient switching $\ldots \ldots \ldots$	60
3.16	Clock input jitter with increased slew rate	60
3.17	RF noise figure of a single detector stack	
	with and without decoupling capacitors	61
4.1	Carbon fibre composite housing fabrication steps	71
4.2	Overview of carbon fibre composites housings	72
4.3	Schematic of plane wave shielding	74

4.4	Basic model of induction
4.5	Calculated shielding efficiency versus sheet conductance
4.6	ASTM 4935-10 TEM cell test equipment
4.7	Specimen thickness and sheet conductance versus number of layers 87
4.8	Measured shielding efficiency
4.9	Analysis range
4.10	Shielding efficiency versus number of layers
4.11	Shielding efficiency per layer versus frequency
4.12	Residual reflection loss
4.13	Comparison of measured and calculated shielding efficiency 94
4.14	Residual error of shielding model
4.15	Shielding efficiency versus sheet conductance
4.16	Ratio of sheet conductance versus shielding efficiency
4.17	Comparison of reflective and absorptive shielding
5.1	Schematic view of plain, staggered and stacked scintillator arrays 106
5.2	Stacked array and definition of neighbourhood channels $\ldots \ldots \ldots \ldots 107$
5.3	Measured position histograms of plain, staggered and stacked array $~\ldots~109$
5.4	Measured position histograms of stacked array
	for both, top and bottom irradiation $\ldots \ldots \ldots \ldots \ldots \ldots \ldots \ldots \ldots \ldots 110$
5.5	Measured energy ratio of centre channel to neighbor channels $\ . \ . \ . \ . \ . \ . \ . \ . \ . \ $
5.6	Plain scintillator array and example light distribution
5.7	Digital SiPM cell logic
5.8	Example inhibit patterns
5.9	Position histogram with regular inhibit pattern and sampling pattern $$ 117
5.10	Computing principle of sub-channel photon counts
5.11	Measured sub-channel light distribution in overlay with sensor tile $\ldots$ . 118
5.12	Simulated detector geometries
5.13	Simulated position histograms
5.14	Simulated energy ratio of centre channel to neighbor channels 126
5.15	Basic operating principle of pixelated, monolithic and
	reflectorless scintillator configuration
5.16	Normalized light distribution of reflectorless arrays
	with different refractive indices and a monolithic scintillator block $\ . \ . \ . \ . \ 131$
5.17	Light spread and mean photon count values
	at different refractive indices
5.18	Light distribution of reflectorless array
	with different surface treatments
5.19	Light spread and mean photon count values
	with different surface treatments

## List of Tables

2.1	Properties of short-lived, positron-emitting isotopes used for PET 20
4.1	Survey of RF shields used in PET/MRI systems
4.2	Selected material properties of carbon fibres, epoxy matrix and copper $.69$
4.3	Functional relationship of shielding efficiency and sheet conductance 80
4.4	Measured properties of carbon fibre composite specimen
4.5	Frequency limits used to analyse measurement data 90
5.1	Overview of depth-of-interaction approaches
5.2	Review of optical simulations of scintillation detectors for PET $\ldots \ldots 121$

### Acronyms

- **APD** avalanche photodiode
- **ASIC** application specific integrated circuit
- $\ensuremath{\mathsf{CT}}$  computed tomography
- DOI depth-of-interaction
- **ENIG** electroless nickel immersion gold
- **EPI** echo planar imaging
- **FDG** <sup>18</sup>F-fluorodeoxyglucose
- ${\bf FOV}~{\rm field}{\rm -of}{\rm -view}$
- FWHM full width at half maximum
- GAGG cerium doped gadolinium aluminium gallium garnet
- **GSO** cerium doped gadolinium oxyorthosilicate
- ${\sf LOR}$  line of response
- LSO cerium-doped lutetium oxyorthosilicate
- LYSO cerium-doped lutetium yttrium oxyorthosilicate
- **MRI** magnetic resonance imaging
- **PET** positron emission tomography
- **PLL** phase locked loop
- **PMT** photomultiplier tube
- **POF** plastic optical fibre
- **PSAPD** position sensitive avalanche photo diode
- RF radio frequency
- **SDM** singles detection module

- $\ensuremath{\mathsf{SiPM}}$  silicon photomultiplier
- ${\sf SNR}$  signal-to-noise ratio
- $\ensuremath{\mathsf{SPAD}}$  single photon avalanche diode
- ${\bf SPU}$  singles processing unit
- $\ensuremath{\mathsf{TEM}}$  transverse electromagnetic
- ${\bf TOF}\ {\rm time-of-flight}$

### Chapter 1

### Introduction

### 1.1 Hybrid imaging and the advent of simultaneous PET/MRI

Since the 1970s, medical imaging made tremendous progress, in particular by the invention of computed tomography (CT), positron emission tomography (PET) and magnetic resonance imaging (MRI). All those imaging modalities have their respective strengths and weaknesses and provide different kinds of information. One ongoing research question thus is, how different imaging modalities can be combined to make best use of complementary information. This is in particular true for PET, which provides highly sensitive functional imaging, but lacks anatomical information.

In the early 1990s, first attempts were made to combine PET and CT. Initially, the idea was to combine a partial PET ring with a CT simultaneously on a common rotating gantry (Townsend 2009). Although this approach was quickly discarded because of mechanical difficulties, it triggered the sequential combination of PET and CT. A first prototype was presented in 1998. Already 3 years later, in 2001, the first commercial PET/CT scanner entered the market.

The combination of PET and CT turned out be very successfully. Within a couple of years, the market for PET only systems vanished. Although technically simple and straightforward, PET/CT was kind of revolutionary, because it completed the functional information of PET with the anatomical information of CT by a single examination. Furthermore, PET gained from the attenuation information that can be extracted from CT data. An additional transmission scan was thus avoided. PET/CT thus provided clinical benefits at shorter scan times with more convenient patient handling and higher patient throughput (Beyer and Townsend 2006), which are all important aspects to get a new modality accepted by clinicians, patients as well as health care providers. In 2009, approximately 2000 PET/CT scanners were installed in the US and about 350 system in Europe (Buck et al. 2010).

Yet, PET/CT scanners operate sequentially rather than simultaneously. A temporal co-registration, as it would be required e.g. for motion correction, is thus impeded. Furthermore, CT poses an additional radiation dose to patients. Both problems could be solved by the simultaneous combination of PET and MRI. The combination of PET and MRI appears to be very promising, in particular as MRI is a very versatile imaging

modality, which provides better soft tissue contrast than CT and additional functional imaging methods, without posing a radiation dose. However, the simultaneous combination of PET and MRI poses a number of engineering challenges.

Early investigations to combine PET and MRI into truly simultaneous, hybrid imaging systems date back to the 1990s. Most obviously, conventional PET detectors are inoperable inside an MRI, because they are based on photomultiplier tubes, which are very sensitive to magnetic fields. First investigators circumvented this hurdle by inserting long optical fibres between the scintillators and the photomultiplier tubes. Thus, the photomultiplier tubes could be operated in safe distance outside the main magnetic field (Garlick et al. 1997, Shao et al. 1997, Slates et al. 1999b). However, this approach limited itself to small prototypes, not only because the optical fibres degraded energy and time resolution, but rather because of the sheer amount of required fibres. More scalable and integrated approaches presupposed the replacement of the photomultiplier tubes by MRI-compatible photodetectors.

The next technological step was the use of avalanche photodiodes (APDs). APDs are semiconductor devices and operate well inside strong magnetic fields (Pichler et al. 1997). Numerous detector concepts were presented and multiple systems were successfully built up with this technology (Grazioso et al. 2006, Maramraju et al. 2011, Schlyer et al. 2007). In 2010, the first commercial clinical whole-body simultaneous PET/MRI system was presented by Siemens Healthcare, based on APD technology. A disadvantage of APDs, however, remains their low intrinsic gain of typically only 10 to 1000 and their high temperature dependency of about  $3.5 \,\% \,\mathrm{K}^{-1}$  (Spanoudaki et al. 2005). The resulting charge signal is in the order of only  $10^{-15} \,\mathrm{C}$  and requires a high gain and low noise charge amplifier, which makes APD-based detectors intrinsically prone to electromagnetic interference from the MRI system and special attention must be paid to electromagnetic shielding (Pichler et al. 2006). The timing resolution of current APD detectors is in the range of several nanoseconds and thus insufficient for time-of-flight PET. Furthermore, APDs commonly require a bias voltage above 100 V and so require appropriate handling of high voltages.

A modification of the APD is the position sensitive avalanche photo diode (PSAPD), which essentially is an array of APD cells connected by a network of resistors. PSAPDs provide a superior intrinsic spatial resolution combined with a low number of required readout channels, which makes them attractive for very high-resolution, small-animal PET systems. Pixelated scintillator arrays with 0.5 mm pitch could be successfully read out using PSAPDs (James et al. 2009, Stickel et al. 2007). Although PSAPDs are operational in an MRI, the resulting position histograms show deformations caused by the static magnetic field (Catana et al. 2006, Chaudhari et al. 2009).

A more advanced development of solid state photon detectors are silicon photomultipliers (SiPMs). SiPMs are composed of arrays of Geiger-mode APDs, also known as single photon avalanche diodes (SPADs). They provide a high internal amplification of 10<sup>5</sup> to 10<sup>6</sup> and fast response times. Coincidence timing resolutions well below 1 ns FWHM make them suitable for time-of-flight PET. In 2011, the first PET/MRI prototype systems based on silicon photomultipliers were presented: the Hyperion I system developed by Philips Research on behalf of the HYPERImage consortium (Schulz et al. 2012, Weissler et al. 2014) and a system developed at Seoul National University (Yoon et al. 2012). Both scanners are prototype systems intended for small animal imaging. The first commercial clinical whole-body simultaneous PET/MRI system based on SiPMs was announced by GE Healthcare in 2014. Although SiPMs have been demonstrated to work inside MRI environments, they still require external signal digitization, e.g. by an application specific integrated circuit (ASIC), and the capabilities of the digitizer used affect achievable system performance and integration substantially.

In 2009, a novel type of solid-state photodetector was presented, the so-called digital SiPM (Degenhardt et al. 2009, Frach et al. 2009). The digital SiPM enhances the idea of the common analogue SiPM by combining an array of Geiger-mode photodiodes with digital logic on a common silicon substrate. Its key feature is the detection and digitization of each individual photodiode breakdown. Thereby, the previously analogue process of energy integration becomes a digital counting process. In combination with an integrated time stamper, the digital SiPM requires no external digitization at all - recorded energy and time information is transmitted digitally for each detected event. Its high functional integration and expected immunity to magnetic fields makes the digital SiPM a very promising photodetector for simultaneous PET/MRI.

However, a successful simultaneous combination of PET and MRI requires more than the bare replacement of the photodetector. Working simultaneously, both imaging modalities have to be placed close together, which makes them susceptible to mutual interference. The identification an minimization of interference effects thus is one of the major engineering challenges implement simultaneous PET/MRI successfully.

### 1.2 Thesis scope and structure

This thesis focuses on hardware implementation aspects of simultaneous PET/MRI. In particular the design of an MRI-compatible digital SiPM based photodetector stack, an improved RF shielding with lower eddy currents and the depth-of-interaction problem of gamma detectors are addressed. Presented work is related to the development of the world's first simultaneous PET/MRI system based on digital SiPMs, the Hyperion II<sup>D</sup> system. The aim was, to achieve an utmost unimpaired performance of PET and MRI during simultaneous operation.

Chapter 1 outlines the main scope, contributions and resulting publications of this thesis.

Chapter 2 briefly introduces the basic operating principles of PET and MRI as well as the technical challenges to combine PET and MRI simultaneously. Furthermore, the key aspects of the digital SiPM as well as the design of the Hyperion II<sup>D</sup> PET/MRI system are outlined.

In chapter 3, the development, characterization and optimization of a digital SiPM based photodetector stack is presented. The presented detector stack is one of the key components of the Hyperion II<sup>D</sup> PET/MRI system. Novel methods have been implemented to measure the energy and timing performance of the digital SiPM inside and outside the MRI down to single event level, which enabled the identification and elimination of the causes of initially observed energy and timing degradations.

Chapter 4 focuses on the RF shielding and eddy current properties of carbon fibre composites. Based on carbon fibre composites, a novel modular RF shielding concept for MRI-compatible PET detectors has been developed. Beyond the fabrication of the housing, the main focus here is to characterize the RF shielding efficiency of carbon fibre composites and their sheet conductance. It is shown, that lower conductivity but thicker materials in general can provide a higher shielding efficiency to sheet conductance ratio than conventional copper shields can do, which is beneficial for simultaneous PET/MRI to reduce eddy current induced distortions. A standardized test method is used to characterize the material specific shielding properties of carbon fibre composites, compare them to analytical results and deduce a model to calculate the shielding efficiency within the MRI frequency range. Excellent agreement between measured and modelled data has been found.

Chapter 5 covers experimental and simulation methods to improve the optical design of pixelated scintillation detectors. Although the basic optical design of scintillation detectors is the same for standalone PET and simultaneous PET/MRI, the confined construction space inside an MRI increases the impact of the parallax error. Thus, a depth-encoding scintillation detector with single-sided readout is of particular interest for PET/MRI. Different approaches have been investigated and a novel approach that avoids the use of inter-crystal reflectors is proposed.

Finally, chapter 6 concludes the main findings and outlines further research and development perspectives.

### **1.3 Contributions**

This thesis arose in the context of multiple research projects, all focused around the development of the Hyperion II<sup>D</sup> digital SiPM PET/MRI insert. Although the main ideas and investigations in this thesis are original work of the author, it benefited from collaboration with colleagues at Philips Research, King's College London and RWTH Aachen University, as well as external project partners.

In chapter 3, the development of the detector stack relied on the contributions of Björn Weissler, research scientist at Philips Research, who developed the singles processing unit as well as the readout and control software, and Pierre Gebhardt, PhD student at King's College London, who developed the firmware of the detector stack. The mechanical implementation of the module housing and the cooling system was carried out in close collaboration with Wolfgang Renz, Irmato Industrial Solutions. Jakob Wehner, PhD student at RWTH Aachen University, provided the MRI gradient test sequences.

In chapter 4, many of the composites shown have been fabricated by Sarah Lodomez and Christopher Anderson during their internship and master thesis, respectively. Sheet conductivity measurements were kindly performed by Frank Jessen and Matthias Marx, GaN Device Technology, RWTH Aachen University, as well as Martin Busch, SURA-GUS GmbH, Dresden, Germany. The RF test cell and access to high frequency measurement equipment was kindly provided by Hammam Shakhtour, Institute of High Frequency Technology, RWTH Aachen University.

In chapter 5, Sarah Lodomez and Rainald Haagen supported the experimental implementation of the sub-pixel measurement. Furthermore, Rainald Haagen supported as part of his master thesis the initial setup of the Geant4/GATE simulation framework.

### **1.4 List of publications**

- Dueppenbecker, P. M., J. Wehner, W. Renz, S. Lodomez, D. Truhn, P. K. Marsden, and V. Schulz (2012a). 'Gradient transparent RF housing for simultaneous PET/MRI using carbon fiber composites'. In: *IEEE Nuclear Science Symposium and Medical Imaging Conference*. IEEE, pp. 3478–3480. DOI: 10.1109/NSSMIC.2012.6551793.
- Dueppenbecker, P. M., B. Weissler, P. Gebhardt, D. Schug, J. Wehner, P. K. Marsden, and V. Schulz (2016). 'Development of an MRI-compatible digital SiPM detector stack for simultaneous PET/MRI'. In: *Biomedical Physics & Engineering Express* 2.1, p. 015010. DOI: 10.1088/2057-1976/2/1/015010.
- Dueppenbecker, P. M., R. Haagen, S. Lodomez, P. K. Marsden, and V. Schulz (2011a). 'A method for measuring the sub-pixel light distribution of scintillation detectors with digital SiPMs'. In: *IEEE Nuclear Science Symposium and Medical Imaging Conference*. IEEE, pp. 2301–2302. DOI: 10.1109/NSSMIC.2011.6153866.
- Dueppenbecker, P. M., S. Lodomez, R. Haagen, P. K. Marsden, and V. Schulz (2011b). 'Investigation of a sub-millimeter resolution PET detector with depth of interaction encoding using digital SiPM single sided readout'. In: *IEEE Nuclear Science Sympo*sium and Medical Imaging Conference. IEEE, pp. 2252–2253. DOI: 10.1109/NSSMIC. 2011.6152490.
- Dueppenbecker, P. M., B. Weissler, P. Gebhardt, D. Schug, J. Wehner, P. K. Marsden, and V. Schulz (2012b). 'Development of an MRI compatible digital SiPM based PET detector stack for simultaneous preclinical PET/MRI'. In: *IEEE Nuclear Science Symposium and Medical Imaging Conference*, pp. 3481–3483. DOI: 10.1109/NSSMIC. 2012.6551794.

- Goldschmidt, B., D. Schug, C. Lerche, A. Salomon, P. Gebhardt, B. Weissler, J. Wehner,
  P. M. Dueppenbecker, F. Kiessling, and V. Schulz (2015). 'Software-based Real-Time
  Acquisition and Processing of PET Detector Raw Data'. In: *IEEE Transactions on Biomedical Engineering* 9294.c, pp. 1–1. DOI: 10.1109/TBME.2015.2456640.
- Schug, D., J. Wehner, P. M. Dueppenbecker, B. Weissler, P. Gebhardt, B. Goldschmidt, A. Salomon, F. Kiessling, and V. Schulz (2015a). 'PET performance and MRI compatibility evaluation of a digital, ToF-capable PET/MRI insert equipped with clinical scintillators'. In: *Physics in Medicine and Biology* 60.18, pp. 7045–7067. DOI: 10.1088/0031-9155/60/18/7045.
- Schug, D., J. Wehner, P. M. Dueppenbecker, B. Weissler, P. Gebhardt, B. Goldschmidt, T. Solf, F. Kiessling, and V. Schulz (2015b). 'ToF Performance Evaluation of PET Modules With Digital Silicon Photomultiplier Technology During MR Operation'. In: *IEEE Transactions on Nuclear Science* PP.99, pp. 1–1. DOI: 10.1109/TNS.2015. 2396295.
- Schug, D., J. Wehner, P. M. Dueppenbecker, B. Weissler, P. Gebhardt, B. Goldschmidt, T. Solf, and V. Schulz (2014). 'ToF performance evaluation of a PET insert with Digital Silicon Photomultiplier technology during MR operation'. In: *EJNMMI Physics* 1, A20. DOI: 10.1186/2197-7364-1-S1-A20.
- Schug, D., J. Wehner, B. Goldschmidt, C. Lerche, P. M. Dueppenbecker, P. Hallen,
  B. Weissler, P. Gebhardt, F. Kiessling, and V. Schulz (2015c). 'Data Processing for a High Resolution Preclinical PET Detector Based on Philips DPC Digital SiPMs'. In: *IEEE Transactions on Nuclear Science* PP.99, pp. 1–10. DOI: 10.1109/TNS.2015.
  2420578.
- Wehner, J., B. Weissler, P. M. Dueppenbecker, P. Gebhardt, B. Goldschmidt, D. Schug, F. Kiessling, and V. Schulz (2015). 'MR-compatibility assessment of the first preclinical PET-MRI insert equipped with digital silicon photomultipliers.' In: *Physics in Medicine and Biology* 60.6, pp. 2231–2255. DOI: 10.1088/0031-9155/60/6/2231.
- Wehner, J., B. Weissler, P. M. Dueppenbecker, P. Gebhardt, D. Schug, W. Ruetten, F. Kiessling, and V. Schulz (2014). 'PET/MRI insert using digital SiPMs: Investigation of MR-compatibility'. In: Nuclear Instruments and Methods in Physics Research, Section A: Accelerators, Spectrometers, Detectors and Associated Equipment 734, pp. 116–121. DOI: 10.1016/j.nima.2013.08.077.
- Weissler, B., P. Gebhardt, P. M. Dueppenbecker, J. Wehner, D. Schug, C. W. Lerche, B. Goldschmidt, A. Salomon, I. Verel, E. Heijman, M. Perkuhn, D. Heberling, R. M. Botnar, F. Kiessling, and V. Schulz (2015). 'A Digital Preclinical PET/MRI Insert and Initial Results'. In: *IEEE Transactions on Medical Imaging* 34.11, pp. 2258–2270. DOI: 10.1109/TMI.2015.2427993.
- Weissler, B., P. Gebhardt, P. M. Dueppenbecker, B. Goldschmidt, A. Salomon,D. Schug, J. Wehner, C. Lerche, D. Wirtz, W. Renz, K. Schumacher, B. Zwaans,P. Marsden, F. Kiessling, and V. Schulz (2012). 'Design concept of world's first pre-

clinical PET/MR insert with fully digital silicon photomultiplier technology'. In: *IEEE Nuclear Science Symposium and Medical Imaging Conference*. IEEE, pp. 2113–2116. DOI: 10.1109/NSSMIC.2012.6551484.

### Chapter 2

### Background

### 2.1 Positron emission tomography

Positron emission tomography (PET) is a functional medical imaging method to image the distribution of positron-emitting tracers in vivo. Depending on the kind of tracer and its application, the tracer can track metabolic, chemical or volume flow processes and thus allows PET to be used for various clinical questions. Most prominently, PET is used in oncology for cancer diagnosis and management. Furthermore, PET is used in cardiology to measure myocardial perfusion and viability, as well as in neurology in the domains of epilepsy, brain tumours and dementia. Initial attempts to use positronemitting isotopes for medical imaging date back to the 1950s (Brownell and Sweet 1953). First results obtained with modern like, ring based PET scanners were published in the 1970s by Phelps et al. (1975) and Ter-Pogossian et al. (1975). In the 1980s, PET scanners became commercially available.

PET basically measures the spatial distribution of positron annihilations in an object. During positron decay, the decaying isotope emits a positron with a kinetic energy of up to a few MeV, as illustrated in figure 2.1. In matter, the emitted positron loses its kinetic energy quickly by collisions with surrounding atoms. With decreasing kinetic energy, the probability of the positron to interact with an electron by annihilation increases. During annihilation, the mass of the positron and the electron is converted into two 511 keV gamma photons, the so-called annihilation photons. The energy of the annihilation photons corresponds to the rest energy of the electron and the positron. Momentum conservation forces both annihilation photons to be emitted in almost opposite directions. The remaining kinetic energy of the positron and the electron at the time of annihilation causes a slight acollinearity of about 0.25° FWHM. Both, the positron range and the gamma acollinearity, result in a fundamental blurring of the tracer distribution in the reconstructed images (Moses 2011).

PET tracers make use of a handful of short-lived, positron-emitting isotopes, listed in table 2.1. On the one hand, the short half-life is advantageous to keep the radiation dose low, but on the other hand it requires the isotopes to be produced nearby and on demand. The most commonly used tracer is <sup>18</sup>F-fluorodeoxyglucose (FDG), a glucose analogue, with one of the hydroxyl groups of glucose replaced by an <sup>18</sup>F atom. FDG is

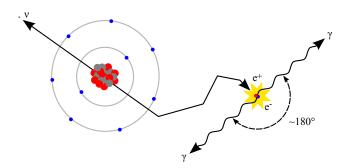


Figure 2.1 During positron decay, a proton of the nucleus is converted into a neutron, a positron and a neutrino. After losing most of its kinetic energy, the positron interacts with an electron by annihilation. During the annihilation process, the mass of the positron and the electron is converted into two almost anti-parallel 511 keV gamma photons. Strictly speaking, the emission of two gamma photons is the most likely outcome of the annihilation process. In rare cases, which are not considered for PET imaging, more than two gamma photons are emitted.

Table 2.1 Properties of short-lived, positron-emitting isotopes used for PET. The initial kinetic energy of the positron causes a slight offset between the positron of positron decay and its annihilation, whereas the remaining kinetic energy of the positron at the time of annihilation causes a slight acollinearity of the two resulting gamma photons. The isotopes <sup>11</sup>C, <sup>13</sup>N, <sup>15</sup>O and <sup>18</sup>F require a cyclotron for production, whereas <sup>68</sup>Ga and <sup>82</sup>Rb can be eluted from <sup>68</sup>Ge and <sup>82</sup>Sr generators respectively.

positron emitting isotope	$^{11}\mathrm{C}$	$^{13}\mathrm{N}$	$^{15}\mathrm{O}$	$^{18}\mathrm{F}$	$^{68}$ Ga	$^{82}$ Rb
half-life (min)	20.4	9.96	2.03	109.8	68.3	1.25
maximum positron energy $(MeV)$	0.959	1.197	1.738	0.633	1.898	3.40
mean positron range in water (mm)	1.1	1.5	2.5	0.6	2.9	5.9

Data derived from Bailey et al. 2005, p. 22

taken up like glucose, but gets trapped in cells because it cannot be fully metabolised due to the missing hydroxyl group. For a typical clinical FDG PET scan, an activity of about 100 MBq to 500 MBq is administered, resulting in an effective radiation dose of about 2 mSv to 10 mSv, which is roughly 1 to 4 times the average annual radiation dose.

#### 2.1.1 Basic measurement principle and limits

The basic operating principle of a PET scanner is to detect both annihilation photons coincidently (i.e. near simultaneously) and then reconstruct the spatial distribution of annihilation processes from a number of such events. Commonly, PET scanners are realized as a ring of gamma detector, surrounding the object. The basic approach is to localise the annihilation position of coincident detected gamma particles to a straight line between the detector elements, the so called line of response (LOR). The use of LORs can be attributed to a lack of proper gamma detectors that can measure

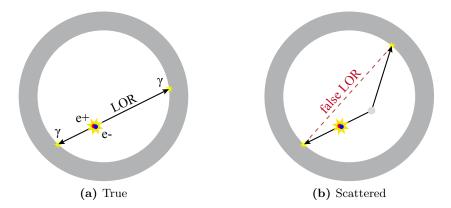


Figure 2.2 True and scattered events. (a) If both annihilations photons are detected, the LOR is determined by the two detection points. (b) Compton scattering can deviate gamma photons and thus result in false LORs. Such events can be identified and rejected based on energy filtering, because the scattered 511 keV annihilation photon lost part of its energy during scattering.

the incident photon directions sufficiently accurately. The coincident measurement principle makes PET very sensitive, since no collimator is required to determine the line of response. However, in practice a number of physical effects have to be taken into account.

First of all, the assumption of a straight LOR is hampered by the slight acollinearity of the two gamma photons, which causes a blurring of the estimated position. The effect is proportional to the diameter of the detector ring and can be estimated to be 0.22% FWHM of the detector ring diameter (Moses 2011), i.e. 1.76 mm FWHM for a 80 cm ring and 0.44 mm FWHM for a 20 cm ring. In principle, it is thus preferable to have a narrow detector ring that matches the size of the scanned object. Beyond the diameter, the geometric coverage of the detector ring and in particular its axial extent are important factors to influence the detection efficiency of a PET scanner.

The LOR estimation assumes that both gamma photons reach the detector without interacting with the scanned object or other objects within the field-of-view (FOV). The attenuation coefficient of water for 511 keV gamma photons is about 0.093 cm<sup>-1</sup> (Burger et al. 2002). Thus, while travelling 7.4 cm in water, a 511 keV gamma photon will interact with a probability of about 50 %. Naturally, if one of the gamma photons is absorbed, no LOR can be computed. Moreover, gamma photons can be deviated, in particular by Compton-scattering. During Compton-scattering the gamma photon gets deflected and loses part of its energy. Such events can be identified and rejected if the energy of the detected gamma photon is measured. Thus, the energy resolution is an important property of a PET detector to filter out scattered gamma photons. The actual impact of scattered photons on image quality depends on the probability of a photon to interact with the scanned object and increases with the size of the scanned

object. Thus, energy resolution is in general more important for human size than small animal PET systems.

Depending on the size and composition of the scanned object, the attenuation of gamma photons before reaching the detector causes a substantial loss of sensitivity. For example, only 6% of the events in the middle of a 30 cm water filled cylinder will emit two gamma photons without interacting with the water filled cylinder itself, whereas in a 3 cm water filled cylinder, the chance is about 75%. Thus, PET reconstruction software has to account for this attenuation to obtain quantitative results, which is usually done by using an attenuation map of the scanned object. An attenuation map can be acquired with an additional transmission scan, or it can be deduced from other imaging modalities, e.g. PET/CT systems derive attenuation information from a CT scan. The larger and denser the object is, the more important the attenuation map becomes, because the scattering and absorption probability increases. The attenuation map is therefore more important for human size than small animal PET systems.

During a typical PET exam, there are up to several million annihilation events per second. To uniquely assign all annihilation photons to their respective counterpart, the arrival time of each photon is measured. However, this assignment is only possible if the PET scanner can resolve the time difference between multiple events, as illustrated in figure 2.3 (a). It should be noted that the time distance between decay processes is Poisson distributed, i.e. most events occur at intervals much shorter than the mean value. For example, although an activity of 100 MBq results on average in one decay per 10 ns, the actual interval between more than 63% of the events is less than 10 ns and 9% occur at intervals shorter than 1 ns. Thus, PET scanners require a time-resolution in the order of a few nanoseconds, or preferably less.

Gamma photons propagate with the speed of light, i.e.  $300 \times 10^6 \text{ m s}^{-1}$ . Thus, if an annihilation is located not exactly halfway between two gamma detectors, one of the two gamma photons will arrive at the detector slightly earlier than the other one. For example, the arrival time difference of an 1 cm off-centre placed annihilation is about 67 ps. If known, the arrival time difference can be used to localise the annihilation position on the LOR more precisely, which is known as time-of-flight (TOF) PET (Budinger 1983). Time-of-flight PET can improve the signal-to-noise ratio (SNR) of the resulting PET images and can thus be used to reduce the scan time or the required radiation dose (Conti 2011). First commercial time-of-flight PET systems became available in 2006.

An ideal detector would measure the arrival time so precisely that the annihilation point on the LOR could be accurately determined, which essentially would eliminate reconstruction. However, real detectors have a limited temporal resolution and can thus only give an estimate of the annihilation point, as shown in figure 2.3 (b). State of the art systems achieve about 350 ps full width at half maximum (FWHM) and thus can locate the origin within 5.2 cm FWHM. The realizable advantage depends on the

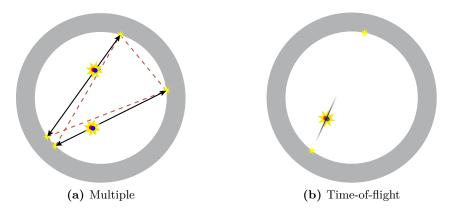


**Figure 2.3** Multiple events and the time-of-flight principle. (a) The correct LOR of multiple events can be distinguished if the PET scanner is able to identify pairs of annihilation photons correctly based on their arrival time. (b) If measured accurately, the difference in arrival time allows the calculation of the annihilation origin on the LOR. Taking into account the limited time resolution of real detectors, the origin can only be estimated.

ratio of the location uncertainty and the size of the scanned object, i.e. larger objects gain more than small objects. Thus, with the currently achievable temporal resolution, time-of-flight PET is mainly relevant for human size rather than small animal imaging.

#### 2.1.2 Gamma detectors for PET

An ideal gamma detector would detect all incident annihilation photons and measure precisely the energy, time and position of each interaction. However, real detectors can fulfil these requirements only partially.

The main problems is the high energy of the annihilation photons. Whilst the high energy is advantageous to escape the measurement object, very dense and sufficiently thick materials are required to achieve a high detection probability. In consequence, an efficient direct conversion of annihilation photons into a measurable electric signal, e.g. with common semi-conductors, is difficult. For example, about 11 cm of silicon would be required to achieve an interaction probability of 90 %.

State of the art PET detectors are based on high density, inorganic scintillators, which convert the energy of gamma photons into short showers of optical photons. Those optical photons are subsequently measured with a photodetector. Other detector approaches, for example plastic scintillators (Kapłon et al. 2014), liquid xenon detectors (Chepel 1993) or semiconductors (Vaska et al. 2005), are subject to research, but still facing a number of problems and could until now not prevail.

The primary interactions of 511 keV gamma photons with matter are Compton scattering and the photoelectric effect. Both effects eject an electron from an atom, which successively deposits its kinetic energy by collisions with surrounding atoms. In a scintillator, those collisions excite electrons from the valence band to the conduction band. During the relaxation back to the valence band, optical photons are emitted isotropically. Ideally, the amount of photons is proportional to the deposited energy.

Whilst the photoelectric effect transfers the entire energy of a gamma photon into an electron, Compton scattering results in a partial energy transfer to an electron and a scattered gamma photon with decreased energy. This scattered, lower energy photon can transfer its remaining energy by further Compton scattering or photoelectric absorption with the scintillator, but it might also escape the scintillator, resulting in an incomplete measurement. However, Compton scattering causes multiple scintillation centres and complicates the identification of the initial interaction point. Consequently, for a gamma detector, the photoelectric effect is preferred. Since the probability for photoelectric absorption increases with the atomic number of the respective nucleus, materials with high atomic numbers are preferred for scintillators.

Today's most established scintillators in PET are cerium-doped lutetium oxyorthosilicate (LSO) (Melcher 2000, Melcher and Schweitzer 1992) and cerium-doped lutetium yttrium oxyorthosilicate (LYSO). Both materials are high density, transparent single crystals with very similar properties. The light yield of LSO and LYSO is about 26000 to 32000 photons per MeV, although not fully linear with energy. Thus, a 511 keV gamma photon results in about 13000 to 16000 optical photons, an incredible small amount that is invisible with the naked eve. For comparison, a common candle emits about  $4 \times 10^{15}$  photons/s. LSO and LYSO are fast scintillators with a decay time of about 40 ns and an intrinsic energy resolution of 6% to 10%. The peak optical emission of LSO and LYSO is near 420 nm, corresponding to visible blue to violet light. The refractive index of both materials is close to 1.8, which is higher than the refractive index of most other commonly used optical materials. Both materials are very dense materials  $(7.1 \,\mathrm{g \, cm^{-3}}$  to  $7.4 \,\mathrm{g \, cm^{-3}})$ , which results in an attenuation coefficient of  $0.83 \,\mathrm{cm}^{-1}$  to  $0.87 \,\mathrm{cm}^{-1}$  at 511 keV, which is roughly 10 times higher than that of water. For example, to obtain 90 % detection efficiency for single 511 keV gamma photons, 2.6 cm of LSO are required. The ratio of photoelectric to Compton interaction probability for 511 keV gamma photons in LSO is about 52% (Shao et al. 1996).

LSO and LYSO are very expensive materials, mainly because of the high costs of lutetium, but also because of the costly fabrication process. Both scintillators are produced by slowly drawing a single crystal from a melt using the Czochralski process, with the melting point of LSO and LYSO being about 2100 °C and 2050 °C, respectively. At the time of writing, 1 cm<sup>3</sup> of LYSO cost about 30 US\$. Approximately 71 to 81 of scintillator material are required to build a state-of-the-art clinical PET scanners, which at the stated price corresponds to more than 200,000 US\$ per scanner. The scintillators are a significant cost factor of PET systems and one of the limiting factors for the development of more sensitive systems.

Beyond the selection of scintillator materials, the structuring of the scintillators and the optical read-out is crucial for the performance of a PET scanner. Most state

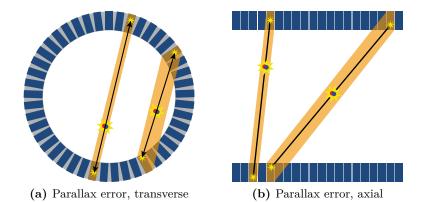


**Figure 2.4** The parallax error limits the spatial resolution of annihilations the transverse plane (a) as well as in axial direction (b). To improve the spatial resolution of a PET scanner, both the crystal pitch and the parallax error have to decreased. The actual impact of the parallax effect depends on the geometry of the scanner as well as the annihilation position, but in general increases for objects located closer to the detector and for large axial FOVs.

of the art PET scanners use two-dimensional arrays of cuboid scintillator elements, commonly referred to as crystals. A typical crystal size for clinical scanners is about  $4 \times 4 \times 20 \text{ mm}^3$ , whereas small-animal system have a crystal pitch in the order of 1 mm. Usually, all but one crystal surface are covered with a reflector and the uncovered surface is attached to a photodetector. The reflector aims to guide as much as possible scintillation light towards the uncovered surface, independent of the actual interaction position in the crystal.

Using this approach, each individual scintillator element represents the finest granularity to allocate gamma interactions. Where exactly the gamma interaction takes place in the crystal is unknown, which widens the LOR to kind of a tube of possible annihilation origins. The achievable spatial resolution of PET scanners with pixelated scintillators thus depends substantially on the granularity of the scintillator arrangement. Very obviously, the resolution of PET scanners can be improved by decreasing the crystal pitch, although there are some practical concerns, e.g. the aspect ratio, the uniformity of the light yield and the number and size of photodetector channels required.

Beyond the crystal pitch, the unknown interaction depth results in a further uncertainty, known as the parallax error, as illustrated in figure 2.4. In particular, annihilations close to the detector ring will hit the crystals laterally. Although the actual impact on image quality depends on multiple parameters, including the system geometry as well as the size and position of the scanned object (Thoen et al. 2013), the parallax error is one of the key issues limiting the spatial resolution of PET scanners.

The parallax error can be reduced if the interaction position is measured more precisely. This approach is commonly known as depth-of-interaction (DOI) measurement. Although subject to research for many years, up to now no fully satisfactory approach



**Figure 2.5** Example of a PMT with a diameter of about 25 mm, as used for conventional PET detectors. The light enters the PMT at the right side and hits on a photocathode. Emitted electrons are successively accelerated and amplified by a series of dynodes. While flying from dynode to dynode, electrons can be easily deviated by the presence of magnetic fields.

to implement depth encoding has been found. An overview of such approaches will be given in chapter 5. Virtually all of them incorporate a trade-off with other performance parameters.

Beyond the parallax effect, depth-of-interaction becomes also increasingly important for time-of-flight PET systems. As the time resolution of time-of-flight PET systems approaches 100 ps (1.5 cm) and less, the impact of the optical path inside the scintillator increases and should be accounted for (Brunner et al. 2013). However, the actual impact of the optical transition time is non-trivial, since at least part of the optical transition time is compensated by the correspondingly longer or shorter trajectory of the gamma particle. Actually observed effect thus might be dominated by a depth-dependent light yield.

Ideally, each scintillator element is coupled one-to-one to a photodetector channel. Thus, the amount of measured light can be uniquely assigned to the respective scintillator element and crystal identification becomes trivial. Practically, however, one-to-one coupling is often thwarted by imperfect optical isolations between scintillator elements and the lack of suitable fine pitched photodetectors. Most pixelated scintillator designs thus incorporate, intentionally or not, a certain amount of light sharing.

In many cases, the pitch of the photodetector is larger than the pitch of the scintillator elements, which makes it impossible to uniquely assign photodetector channels to scintillator elements. To overcome this, the light of each scintillator element has to be shared between multiple photodetector channels. In the most simple case, this is achieved by a glass or plastic plate between the scintillator and the photodetector. Subsequently, the measured light distribution is used to calculate the position of the hit scintillator element.

The optical scintillation photons have to be converted into an electrical signal by means of a photodetector. They key properties of photodetectors for PET are a high photon detection efficiency, low signal-to-noise ratio and a fast response time. Up to now, most commercial PET scanners still use photomultiplier tubes (PMTs). An example of a PMT is shown in figure 2.5. Advances in solid-state photodetectors have recently led to the advent of new kinds of photodetectors, i.e. APDs, SiPMs, and most recently the digital SiPM, which is subject to this thesis.

### 2.2 Magnetic resonance imaging

In medicine, magnetic resonance imaging (MRI) is used for in-vivo anatomical and functional imaging. MRI is based on the effect of magnetic nuclear resonance, in which a nuclei with non-zero spin in a magnetic field absorbs energy by an alternating electromagnetic field. During subsequent relaxation, part of the energy is re-emitted and measured. In contrast to PET, MRI is free of ionizing radiation and is considered as very safe. In principle, all nuclei having a non-zero spin can be imaged with MRI. However, the most commonly used nuclei for MRI is hydrogen (<sup>1</sup>H), because it shows a strong magnetic nuclear resonance response and is the most abundant nuclei in the body. Thus, normal tissue can be imaged without requiring any pretreatment. Depending on the imaging sequence used, MRI contrast can be adjusted to image a wide variety of anatomical structures, tissue properties and functional processes, which makes MRI to the most versatile medical imaging modality.

The basic MRI techniques have been developed in the 1970s, with major contributions by Paul Lauterbur and Peter Mansfield, who shared in 2003 the Nobel Prize in Physiology or Medicine. The first commercial MRI scanner was manufactured in 1980. Since then, MRI became widespread clinical practice and one of the most important medical imaging modalities. In 2008, worldwide more than 25000 MRI units have been installed, with an estimate of 80 million exams per year (Cosmus and Parizh 2011).

#### 2.2.1 Basic physics

Spin angular momentum, or simply spin, is a property of nuclei, which can be considered as a constant rotation of the nucleus that results in a magnetic moment. The spin of a nucleus is determined by its number of protons and neutrons and can take only integer and half-integer values, including zero. The fundamental properties and interaction mechanisms of spin can only be explained with quantum mechanics. However, most effects related to MRI can be described by classical mechanics.

By default, spins are randomly oriented, resulting in a zero net magnetization of materials on a macroscopic level. In a magnetic field  $B_0$ , nuclei with non-zero spin start to precess with a constant frequency around the field vector of the applied magnetic field. The axis of precession is aligned either parallel or anti-parallel to  $B_0$ . Since there is a difference in energy for parallel and anti-parallel alignment, which depends on the strength of the applied magnetic field as well as temperature, the ratio of parallel and anti-parallel oriented precessing spins varies, resulting in a macroscopic net magnetization  $M_0$  parallel and proportional to  $B_0$ . For example, the net magnetization caused by hydrogen nuclei in water at room temperature is about  $3.4 \times 10^{-10}$  times the main magnetic field (Bloch 1946), i.e. roughly 1 nT in a 3 T MRI<sup>1</sup>. This is significantly less

<sup>&</sup>lt;sup>1</sup>The actually observed external susceptibility of water and most human tissues is dominated by the water molecule and slightly negative with a susceptibility of about  $-9 \times 10^{-6}$  (Schenck 1996).

than the earth magnetic field  $(25 \,\mu\text{T} \text{ to } 65 \,\mu\text{T}, \text{ Finlay et al. 2010})$  and as static field hardly measurable.

The frequency of the precession depends on the strength of the applied magnetic field  $B_0$  and the gyromagnetic ratio  $\gamma$ , which is a constant for each nuclei. This frequency is known as Lamour or resonance frequency.

$$\omega_0 = \frac{\gamma B_0}{2\pi}.\tag{2.1}$$

For example, the gyromagnetic ratio of the hydrogen nuclei is 42.58 MHz T<sup>-1</sup>, resulting in a resonance frequency of about 128 MHz at 3 T.

The precessing nuclei can absorb energy from a rotating electromagnetic excitation field  $B_1$ , perpendicular to  $B_0$ , if the frequency of the applied field equals the Lamour frequency, i.e. the exciting field is in resonance with spin precession. By taking up energy, the ratio of parallel and anti-parallel oriented precessing nuclei varies slightly. Furthermore, precessing nuclei align in phase, which results in a rotating net magnetic field component with the frequency  $\omega_0$  and perpendicularly aligned to  $B_0$  and  $B_1$ . This rotating, transverse magnetic field component can be measured and constitutes the basic MRI signal. After removing the excitation field  $B_1$ , the precessing nuclei will successively relax to their initial state. During relaxation, the initial magnetization is recovered and its transverse component diminishes. In consequence, also the measurable signal decays, which is known as free-induction decay.

The decay of the transverse magnetization is caused by an energy transfer to the surrounding lattice as well as spin-to-spin interactions of neighbouring nuclei. Both transfers are exponential decay processes that are characterized the time constants T1 and T2. T1 and T2 are characteristic material / tissue properties and are used as image contrast in MRI. Part of the signal decay is caused by field inhomogeneities, causing a slightly different precession frequencies and thus a de-phasing over time. However, there exist various methods to revert this de-phasing at least partially, which results in so called echoes, one of the fundamental principles of MRI.

To implement spatial encoding, MRI makes use of additional magnetic gradient fields that are superimposed to the static magnetic field. The gradient fields are used to vary the Lamour frequency spatially. Thus, specific volumes can be excited and the de- and re-phasing of nuclear spins as well as their precession frequency can be altered.

The measured MRI signal is a sum of all received RF signals. A direct allocation of RF signals to a spatial position is thus impossible. Usually, gradient based phase encoding and a Fourier transformation is used to convert a series of measured signals into an image.

#### 2.2.2 MRI equipment

The main component of an MRI system is the magnet for the static magnetic field  $B_0$ . Nowadays human size MRI scanners are operated at 1.5 T to 9.4 T. Such high field strengths are hardly realizable with permanent magnets or resistive electromagnets, thus virtually all state-of-the-art MRI systems are based on superconducting electromagnets.

Only few superconducting materials can be reasonably be used to build such magnets. Most commonly, niobium-titanium alloys with a critical temperature of about 10 K  $(-263 \,^{\circ}\text{C})$  are used. However, this very low critical temperature requires a cryogenic cooling system to ensure superconductivity, which is us usually realized by a liquid helium cryostat with a boiling point of 4.15 K. Recently, so-called cryogen free magnets have been presented for small animal MRI systems, which avoid the use of liquid helium by placing the superconductors in a vacuum. However, this requires excellent thermal shielding and continuous cooling and is currently only available for small animal MRI systems.

The length of the magnet for a human size system is typically about 1 m to 1.5 m, which is mainly required to achieve a homogeneous magnetic field within the FOV. Because of its superconducting cryogenic construction, the main magnet is one of the most expensive components of an MRI system. Therefore, it is usually attempted to keep the magnet as small as possible and adjust the bore diameter to the size of the scanned object.

Most MRI systems use solenoid magnet coils in which the scanned object is inserted. The diameter of the coil must be large enough to fit the scanned object as well as the other MRI components. Common magnet bore diameters for clinical systems are 70 cm to 80 cm, whereas small animal systems usually have diameters of about 10 cm to 30 cm. Within the FOV, usually about  $40 \times 40 \times 40 \text{ cm}$  to  $50 \times 50 \times 50 \text{ cm}$  for human size scanners, the homogeneity of the B<sub>0</sub> field is crucial for MRI, since any field deviation leads to a deviation of the resonance frequency. Commonly, the field is required to deviate not more than a few parts per million within the FOV.

The MRI gradient system is composed of an arrangements of multiple coils to generate linear magnetic gradient fields in x-, y- and z-directions. Usually, the gradient coils are made of copper strands, embedded with a liquid cooling system in a fibre reinforced composite tube, which fits the bore size of the main magnet. Reliable cooling is essential, because the gradient coils are resistive coils and and generate a lot of heat during operation. Furthermore, the strong electrical currents in the coil interact with the main magnetic field because of the Lorentz force, which causes strong mechanical vibrations and noise. This makes certain MRI scans very loud and mechanical vibrations constitute a reliability issue for nearby components. Naming and specification of gradient fields refers solely to the resulting z-component, although MRI-gradients also inevitably generate x- and y-components, because of the solenoid property of magnetic fields.

Common clinical MRI systems achieve gradient strengths of up to about  $0.1 \,\mathrm{T\,m^{-1}}$ . Beyond the gradient strength, the obtainable gradient slew rate is of special interest, because the gradient slew rate determines how fast the gradients can be switched. Clinical MRI systems achieve gradient slew rates up to about  $200 \,\mathrm{T\,m^{-1}\,s^{-1}}$ , which allows the switching of gradients in less than 1 ms.

Inside the gradient coil is the RF coil. Common whole body RF coils are mainly made of copper structures on fibre reinforces cylinders. In addition, passive and active electronic components are placed on the cylinder, i.e. for frequency tuning, preamplification and digitization. A single coil can be used for transmitting the excitation pulse and receiving the MRI signal, but also dedicated transmit and receive coils can be used.

Since the MRI signal is very weak, precisely tuned RF coils and sensitive RF receivers are required. One of they main issues of MRI is to obtain a high SNR. Longer sampling and repeated sampling in principle can be used to improve the SNR, but this also increases the scan time and thus impairs patient throughput as well as patient convenience. However, systematic distortions, e.g. at a constant frequency, cannot be filtered out. The operating frequency of common MRI systems is in the range of 50 MHz to 500 MHz, a frequency range, which falls in a frequency range that is used by many kinds of electronic devices, e.g. medium to high frequency radio broadcasting and communication. Most clinical MRI scanner thus have to be placed in a Faraday cage like RF shielded room, e.g. by covering all walls, the floor and the ceiling with copper foil. Any door, window or feed through requires special attention not to impair the shielding. Most electrical components of the MRI system itself are placed outside the shielded room in a nearby technical room, e.g. amplifiers, cooling pumps and computers.

Only selected electronic equipment is allowed to be used inside an MRI room. Of course, this also affects the combination of a PET and MRI scanner. The following section will outline the interference effects that have to be considered.

### 2.3 Engineering challenges of simultaneous PET/MRI

The simultaneous combination of PET and MRI poses a number of engineering challenges. The following section gives an overview and discusses their impact on simultaneous PET/MRI system design. This thesis focus on the hardware aspects of the simultaneous combination of PET and MRI. Consequently, only hardware aspects are discussed here, although there are further challenges, e.g. for attenuation correction, motion correction and general work flow.

#### 2.3.1 Interference with the MRI static magnetic field

The static main magnetic field  $B_0$  is the basic component of every MRI system. It is used to align nuclear spins and thus is a fundamental prerequisite for MRI. Most stateof-the-art MRI systems are operated at 1.5 T to 7 T, which is roughly 100 000 times stronger than the earth's magnetic field. Being present to all components inside an MRI, the main magnetic field is the most obvious cause of interference. Furthermore, the main magnetic field of common MRI systems with superconducting magnets is permanently on, because ramping up and down is a time-consuming process.

Very obviously, the main magnetic field attracts para- and ferromagnetic objects. Improper fixed or accidentally introduced objects can thus become a serious thread during regular use for patients and operators, but also for technical staff during service and development. For example, the vast majority of commonly used tools contain iron and are thus troublesome to use in an MRI environment.

The main magnetic field exerts force not only on magnetic objects but also on charged particles in motion. According to the Lorentz force law, magnetic fields deviate charged particles in motion from their initial trajectory. In photomultiplier tubes this disturbs the process of electron multiplication, which was the primary motivation to replace them by solid-state detectors for simultaneous PET/MRI. Path lengths in solid-state detectors are much shorter, so that they can remain functional even within strong magnetic fields, although they still can be affected, e.g. by magnetoresistance. Numerous electronic components, like resistors, capacitors and air coils, are empirically known to operate well within magnetic fields, however others, e.g. ferrite coils, lose most of their functionality, because of ferromagnetic saturation.

The other aspect of the main magnetic field is its influence on MRI image quality. Besides the field strength, the field homogeneity within the FOV is crucial for MRI image quality, because any field inhomogeneity shifts the resonance frequency locally and results in signal loss and image artefacts. This becomes especially obvious for gradient echo based imaging sequences, as phase recovery gets distorted and distortions accumulate for multiple echoes (Brown and Semelka 2010). Consequently, common MRI systems require a very homogeneous main magnetic field that deviates not more than a few parts per million within the FOV. Field inhomogeneities can be caused by any change in magnetic susceptibility within the main magnetic field, but ferromagnetic materials, which obtain a very high and non-linear magnetic susceptibility, are especially problematic (Schenck 1996).

The common primary design strategy is to minimize field inhomogeneities by proper material selection, in particular by eliminating ferromagnetic materials. In principle, it is possible to compensate field inhomogeneities at least partially by passive and active shimming. However, this adds additional complexity to the system. A further source of field inhomogeneities are stray magnetic fields caused by electrical currents. Even though their existence is unavoidable, the influence of stray magnetic fields can be minimized by placing supply and return currents close together, so that resulting fields cancel out, e.g. by using a strict star topology, careful circuit board routing, and the use of twisted pair or coaxial cables.

Finally, the dimensions of the main magnet restrict the available construction space. To avoid attenuation and scattering of gamma photons, at least the gamma sensitive part of an MRI compatible PET detector has to be placed inside the bore. However, increasing the bore size is very expensive and only possible to a limited extend. Thus, a PET detector should be as flat as possible to integrate well into an MRI system. Furthermore, regular MRI magnets are accessible only from the front and rear opening. All connections to the outside of the MRI bore (power supply, signal lines, cooling pipes) thus have to pass through the front and rear opening of the MRI bore.

#### 2.3.2 Interference with the MRI gradient system

MRI spatial encoding is based on shifting the resonance frequency spatially and temporally by superimposing magnetic gradient fields to the static main magnetic field. Although the absolute field strength of MRI gradients is about two orders of magnitude lower than the static magnetic field, they can cause major interference effects, because the gradients are switched very rapidly, up to several hundred times per second. According to Faraday's law of induction, a change in magnetic flux causes a reverse induced current in closed electrical paths, so-called eddy currents.

Eddy currents can influence electronic components, cause heating and vibrations. In consequence, any conductive material within the sphere of the gradient system is subject to eddy currents, including the cryostat and the RF coils. Problems arising from eddy currents accompany the development of MRI from the very beginning. Eddy currents result in a reverse magnetic field that alters the intended gradient form and strength. Initial issues with eddy currents arose from the cryostat and led to the invention of actively shielded gradients. Later on, the RF coil and screen, both usually made of copper, had to be structured to reduce eddy currents. The different sources, conductivity and mutual inductance of eddy currents cause a multi-exponential decay of eddy currents, which makes it difficult to compensate for, e.g. by gradient shimming. Thus, it is preferable to avoid conductive structures within an MRI system.

Eddy currents alter the intended MRI magnetic field locally and temporarily. Thus resulting image distortions are influenced not only by the amplitude of the eddy current but also the decay time is important. However, there are countless MRI sequences. Not all of them will be affected by eddy currents in equal manner. In particular, MRI phase distortions depend on the integral field deviation over time. This aspect is very important for MRI imaging, as gradient time integral is crucial for re-phasing in many MRI sequences. In particular, fast gradient echo based MRI sequences, which are very popular because of their short scan time, are susceptible to eddy current induced phase distortions.

To minimize eddy currents and gradient distortions, conductive structures should be avoided or, if they are required, the extent of conductive loops and planes should be minimized, either by geometry or by the selection of low conductivity materials.

Common MRI systems contain gradient systems for x, y, and z encoding. Naming and specification of MRI gradients refers solely to the axial component of the resulting magnetic field. However, because of the solenoidal property of magnetic fields, the MRI gradient system generates additional radial field components. Those radial components are usually negligible for MRI imaging, but they have to be considered for MRI compatibility. Typically, PET electronics are located tangential to the FOV and are thus perpendicularly aligned to radial field components. This is especially true for the z-gradient along the axial direction, which is commonly generated by an antiparallel pair of Helmholtz coils. This coil configuration generates additional radial magnetic components with comparable magnitude alike the intended axial field component.

The strength of the eddy currents depends on the gradient slew rate and the material conductivity. Within the FOV, the magnetic fields generated by MRI gradients increase with distance to the MRI isocentre. Consequently, the change in magnetic flux density over time and resulting gradient interference effects depend on position and increases with distance.

#### 2.3.3 Radio frequency interference between PET and MRI system

Electromagnetic interference is a ubiquitous issue in electrical engineering. However, it is of particular importance for PET/MRI, since MRI systems entail very sensitive receivers as well as strong transmitters of electromagnetic radiation. MRI systems thus commonly require costly shielded rooms and only selected electrical equipment is allowed to be operated inside an MRI room. In case of a highly integrated simultaneous PET/MRI system, the electronics of an entire PET detector shall be operated not only inside the MRI room, but within the MRI bore, next to the MRI RF transmitter and receiver. This requires careful system design and shielding to minimize electromagnetic interference between both systems.

RF interference between the PET and the MRI system can occur in both directions. On the one hand, RF excitations pulses generated by the MRI might couple into the electronics of the PET detector and disturb or damage it. On the other hand, the PET detector will emit RF radiation during operation, which could couple into the receive chain of the MRI. Electromagnetic shielding of the PET detector is a possible solution. However, common RF shields are based on high conductivity materials, e.g. copper foil, which are in turn problematic in that they can result in gradient interference. Thus, the primary goal is to minimize RF emission by following good engineering practice and avoid the propagation of high frequency voltage and current variations as well as antenna-like structures. At the same time this reduces the risk of coupling RF power from the MRI into the PET detector.

The relevant frequency range of the MRI is determined by the field strength and the Larmor frequency of the nucleus being imaged. The centre frequency for protons at 3 T is 127.28 MHz. This frequency is of the same order as the clock frequency of many digital circuits, e.g. the clock of the digital SiPM is by default supplied at 200 MHz and most digital processing is done at 100 MHz. Furthermore, harmonics from lower frequency switching, e.g. caused by a switch mode power supply (Wehner et al. 2014), can also interfere with the MRI system. Thus also the selection of operating frequencies influences RF interference.

#### 2.3.4 Gamma transparency

PET imaging relies on the coincident detection of 511 keV gamma photon pairs, originating from positron annihilation. Ideally, the LOR is a straight line between two coincident detected gamma interactions, crossing the origin of positron annihilation. However, if gamma photons are scattered or absorbed before being detected, this assumption is violated, which decreases the signal-to-noise ratio and sensitivity.

To avoid scattering and attenuation of gamma photons, the space between the scanned object and the gamma sensitive part of the PET detector should be as transparent as possible for gamma photons. Practically, this means that there should be as less as possible material between the scanned object and the PET detector. In particular, high density materials with a high interaction probability should be avoided. However, even for PET only systems this is not entirely feasible, e.g. the patient table and some detector covers are required.

Multiple components of an MRI system are very massive components, in particular the main magnet and the gradient coils. In consequence, those part have to be kept out of the sensitive volume of a PET scanner.

#### 2.3.5 Confined construction space

Most MRI systems are based on superconducting, cryogenic magnets with a cylindrical opening. The dimensions of the cylindrical opening determines the available construction space within an MRI. It is very expensive to increase the bore diameter, because this requires a larger cryostat and higher magnetic flux. The costs can thus roughly be expected to increase with a power of two of the diameter. In order to make best use of the available space, all components within the MRI bore should thus be as thin as possible. This affects the design of the MRI gradient and RF coil, but of course also any additional equipment, i.e. an integrated PET detector. This is a special requirement for PET/MRI and very different to PET/CT or PET only systems.

Moreover, the confined construction space inside an MRI bore limits the diameter of the PET ring and the distance of the PET detector to the scanned object. Although a narrow PET ring is in principle advantageous, because the effect of acollinearity is decreases and less sensitive area is required to cover the same solid angle, it rises the parallax error.

A further challenge is the mounting of components within the MRI bore. A direct fastening of components inside the bore is difficult, because usually the gradient coil is next to the magnet. The gradient coil itself is subject to strong vibrations during operation and thus unsuitable for the attachment of sensitive devices. Furthermore, in the case of small bore systems it is difficult to work inside the bore. Thus, there remain the front and rear opening of the magnet to insert and mount additional equipment. However, this also implies that the PET detector itself is self-supporting within the MRI bore.

Having a self-supporting PET detector that is only attached at the opening of the MRI bore has a further advantage, because it simplifies the possibility to take out the PET detector out of the bore, e.g. for service, but also during development.

#### 2.3.6 Prevailing simultaneous PET/MRI system design

Caused by the previous mentioned restrictions, basically one simultaneous PET/MRI system design is prevailing. As illustrated in figure 2.6, the prevailing approach is to place the PET detector between the gradient and the RF coil. Thus, the main magnet and gradient coil basically remain unmodified, whereas the diameter of the RF coil has to be reduced. Since the RF coil is placed in front of the PET detector, the RF coil should be as gamma transparent as possible within the FOV of the gamma detectors.

There are different design approaches for simultaneous PET/MRI. For instance, Olcott et al. (2015) report on using battery powered, electrically floating PET modules within the RF transmit coil. At the University of Cambridge, a split magnet / split gradient approach was developed (Poole et al. 2009, Shaw et al. 2005). A comprehensive review system design is summarized by Vandenberghe and Marsden (2015).

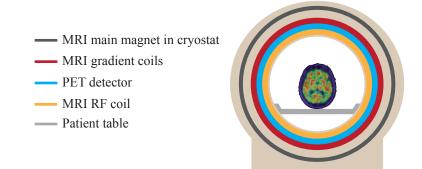


**Figure 2.6** Schematic cross-section of the prevailing PET/MRI system design. The PET detector is placed between the gradient and RF coil of the MRI system. Thus, the high gamma attenuation of the gradient coil is avoided, but RF radiation can pass to the scanned objects without obstacles. From an PET point of view, it would be desirable to have the PET detector innermost to avoid gamma attenuation because of the RF coil. The gamma attenuation of the RF coil should thus be incorporated in the design process and eventually minimized by proper material selection and component placement.

# 2.4 The digital SiPM

The investigations presented in this thesis and the development of the Hyperion II<sup>D</sup> system are based on the DPC-3200-22 digital SiPM from Philips Digital Photon Counting. Currently, the DPC-3200-22 is the only commercially available digital SiPM. The DPC-3200-22 was optimized for human size time-of-flight PET systems. In 2014, the first commercial digital SiPM based PET/CT scanner, the Philips Vereos, was introduced to the market.

The DPC-3200-22, as shown in figure 2.7 (a), consists of a  $7.8 \times 7.2 \text{ mm}^2$  silicon die and combines four digital SiPM channels on a common silicon substrate. Each channel covers an active area of  $3.8 \times 3.2 \text{ mm}^2$  and is composed of 3200 SPADs, arranged in an array of 64 rows and 50 columns. The DPC-3200-22 is sensitive for photons with a wavelength of 380 nm to 700 nm, reaching a peak photon detection efficiency of roughly 40% at 420 nm. By default, the DPC-3200-22 is a self triggering device that starts a readout process as soon a certain amount of SPADs broke down. The DPC-3200-22 contains a digital time stamper, which records the time difference between a trigger signal and a reference clock. The intrinsic coincidence time resolution of the DPC-3200-22 is below 60 ps FWHM (Degenhardt et al. 2010) and therefore well suited for time-of-flight PET.

The DPC-3200-22 is mounted with conductive glue on circuit boards. Electrical contacts are made with up to 48 bond wire connections at the top and bottom edge of each die. The nominal bias voltage of the DPC-3200-22 is  $27.0 \pm 0.5$  V. Usually, multiple DPC-3200-22 devices are combined on a circuit board to form a sensor tile, as shown in figure 2.7 (b). For mechanical protection of the silicon die and the bond wires, a 100 µm glass plate is glued on top of each sensor tile.

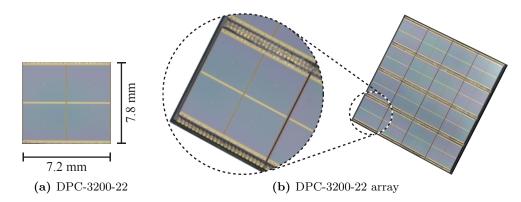


**Figure 2.7** The DPC-3200-22 digital SiPM. (a) The DPC-3200-22 combines four digital SiPM channels on one silicon die. (b) A  $4 \times 4$  array of DPC-3200-22 devices composes a 64-channel digital SiPM array with 4 mm pitch. In this photograph, the  $3.8 \times 3.2 \text{ mm}^2$  sensitive area of each digital SiPM channel appears bluish, whereas the remaining areas appear golden because of metal layers.

The DPC-3200-22 outputs data via two digital data lines, each commonly operated at 100 MHz data rate. The used data protocol is proprietary. Basically, the data stream contains the number of hit cells and the measured time stamp.

A number of settings of the digital SiPM can be configured via a standard JTAG interface, e.g. the trigger threshold, the validation threshold and the integration time. The trigger threshold defines the criterion when to start the time stamper, whereas the validation threshold defines the criterion when to start an integration and subsequent readout process. The trigger threshold can be set to  $1, \geq 2, \geq 3$  or  $\geq 4$  photons. However, the actual trigger threshold is affected by statistical variations since the trigger threshold is a logical tree structure. The first level of this tree structure is a logical conjunction of SPADs within sub-pixel areas. Subsequent, programmable logical con- and disjunctions form the final trigger signal. The trigger threshold is thus subject to statistical variations, including the distribution of incident light. Similar restrictions apply to the validation threshold. More detailed information is explained by Frach et al. (2010).

A peculiarity of the DPC-3200-22 is that four digital SiPM channels not only share the same silicon die, but also the same readout, control and time-stamping unit. Thus, all four channels are always read out, resulting in four photon count values but only one time-stamp value. For the same reason, all four digital SiPM channels are mutually affected by each dark count, unintended trigger and related dead time.

Each SPAD of the DPC-3200-22 can be individually en- and disabled by reprogramming. This functionality is primarily intended to reduce the dark count rate of the digital SiPM. Therefore, the dark count rate of each SPAD is measured by successively enabling each individual cell for a certain amount of time. Based on this measurement, the noisiest cells can be identified and deactivated. Commonly 5% to 20% of the most noisy cells are disabled. However, there always is a trade-off between reducing the dark count rate and maintaining sensitivity, because disabling cells decreases the sensitive area of the chip. Regularly, the cell activation pattern is programmed each time after powering up the DPC-3200-22, but it can also be utilized to program any arbitrary pattern later on, which can be utilized for a novel measurement approaches, as will be shown in chapter 5.3.

Like the conventional analogue SiPM, the digital SiPM is expected to be unaffected by strong magnetic fields. Furthermore, its intrinsic digitization and high functional integration should make it less prone to electromagnetic interference and facilitate system integration. The evaluation of the MRI-compatibility of the digital SiPM and its suitability for simultaneous PET/MRI is one of the key aspects of this thesis and contributed to the development of the world's first digital SiPM based PET/MRI system, the Hyperion II<sup>D</sup> PET/MRI insert. In the following section, the key aspects of the Hyperion II<sup>D</sup> system will be outlined.

# 2.5 The Hyperion II<sup>D</sup> PET/MRI system

The Hyperion  $II^D$  PET/MRI system is an MRI-compatible PET insert, designed to be used in combination with a regular Philips Achieva 3T/60 cm bore diameter MRI system. It is kind of a successor of the Hyperion I system (Weissler et al. 2014), but contains a number of major improvements. In particular, it is the first PET/MRI system based on digital SiPM technology.

Figure 2.8 shows the Hyperion  $II^D$  system, right before the PET detector is inserted into the MRI. The core of the Hyperion  $II^D$  system is an MRI-compatible PET detector ring as shown in figure 2.9, spanning a FOV of 209.6 mm diameter and 96.6 mm axial length. The Hyperion  $II^D$  system utilized the regular MRI gradient system in combination with distinct RF transmit-receive coils located inside the PET ring. Three different MRI transmit-receive coils are currently available: a  ${}^{1}H/160$  mm diameter, a  ${}^{1}H/46$  mm diameter and a multi-nuclei  ${}^{1}H/{}^{19}F/100$  mm diameter coil. The development of Hyperion  $II^D$  system was led by Philips Research, with major contributions from King's College London and RWTH Aachen University.

The objectives of the Hyperion  $II^D$  system are twofold: On the one hand, it is designed to be a fully functional imaging device for small animal imaging. Therefore, much effort was spent on improving the handling of the system. Whereas the Hyperion I system was bulky and required multiple persons to install, the Hyperion  $II^D$  system is mounted on a trolley and uses the regular patient handling system to be inserted into the MRI. Thus, the installation of the system can be done by a single person in a couple of minutes. On the other hand, the Hyperion  $II^D$  system is intended as technology demonstrator to evaluate the feasibility of digital SiPMs for simultaneous PET/MRI - for small-animal imaging, as well as for human whole body simultaneous PET/MRI.

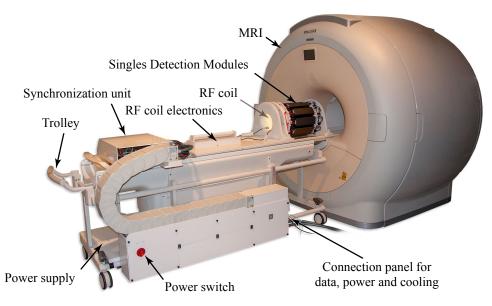
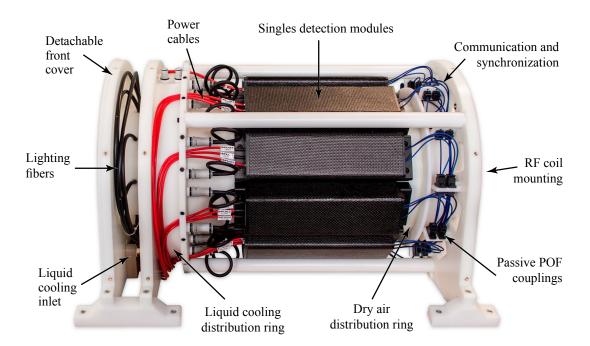
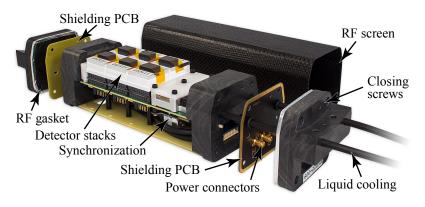


Figure 2.8 The Hyperion  $II^{D}$  PET/MRI insert, right before the PET detector is inserted into the MRI bore. The whole system is mounted on a trolley that fits to the patient handling system of the MRI scanner. Thereby, the system can be easily installed and removed within short time. Figure adapted from Weissler et al. (2015) / CC BY 3.0.



**Figure 2.9** PET detector ring of the Hyperion  $II^D$  system, composed of 10 SDMs and a plastic gantry. The routing of power, data, liquid cooling and pressurized air is included in the gantry. To ease the assembly and the maintenance of the system, all connections can be released at or near the SDM. Figure adapted from Weissler et al. (2015) / CC BY 3.0.



**Figure 2.10** Singles detection module (SDM). Each SDM hosts up to six detector stacks. The RF screen is made of carbon fibre composites and slid over the other components. At the front and the rear, two additional shielding PCBs complete the shielding of the SDM. Picture adapted from Weissler et al. (2015) / CC BY 3.0.

In total, three similar copies of the Hyperion  $II^{D}$  system were build up. A detailed overview and first results of in-vivo imaging studies of the Hyperion  $II^{D}$  system are presented by Weissler et al. (2015).

#### 2.5.1 Main components of the PET detector

The Hyperion II<sup>D</sup> PET detector is composed of a ring of ten detector modules, socalled singles detection modules (SDMs), as shown in figure 2.10. Each SDM is a self-containing gamma detector unit. Its main components are a singles processing unit (SPU), six MRI-compatible digital SiPM detector stacks with pixelated scintillator arrays, a set of cooling pipes and a housing.

The SPU is kind of a motherboard, which collects and forwards all data from and to the detector stacks. Furthermore, it distributes power, contains a number of environmental sensors and controls the overall operation of the SDM. The SPU was designed to minimize MRI interference, in particular  $B_0$  distortions, and is presented in detail by Weissler et al. (2012b).

Electrical power is supplied via three coaxial connectors at the front side of the SDM. On the same side are two feedthroughs for the cooling. Data is transmitted and received via two gigabit plastic optical fibres (POFs) on the opposite side. Likewise, the synchronization and clock signal is supplied. This side also contains an inlet for pressurized air, integrated into the housing of the SDM.

Six detector stacks, as shown in figure 2.11 (a), are contained in one SDM. Each detector stack contains an array of  $8 \times 8$  digital SiPM channels with 4 mm pitch, optimized for MRI-compatibility, reliable cooling and integration into the SDM. The development of the digital SiPM detector stack is one of the main subjects of this thesis and is presented in detail in chapter 3.

Each detector stack is equipped with a  $30 \times 30$  crystal LYSO scintillator array with 1 mm pitch. The size of each crystal is  $0.9225 \times 0.9225 \times 12 \text{ mm}^3$ . Individual crystals

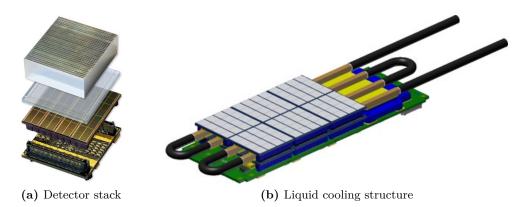


**Figure 2.11** (a) Detector stack with scintillator array and light guide. Figure adapted from Weissler et al. (2015) / CC BY 3.0. (b) The liquid cooling structure, composed of rectangular brass pipes connected by a flexible tubing. The detector stacks and the main components of the SPU are directly coupled to the cooling structure.

are separated by a 65 µm specular reflector film (Vikuiti ESR, 3M), which is full face bonded with an optical clear adhesive to the side and top surfaces of each crystal. Since the crystal pitch is smaller than the photodetector pitch, a structured, 2 mm thick light guide is mounted between the scintillator array and the digital SiPM array. The light guide spreads the light of single crystals to multiple digital SiPM channels and thus allows the calculation of the position of hit crystals. To improve the separability of crystals along the edges, the light guide is structured by four white-filled slits along the edges.

The power dissipation of each SDM is approximately 30 W. Since it is an enclosed module, heat must be dissipated via a cooling system. The primary cooling system of each SDM is a liquid cooling system, as shown in figure 2.11 (b). It dissipates the heat of the detector stacks as well as the SPU. The design of the cooling system was mainly driven by the requirement to cool the digital SiPMs reliably. It is composed of four rectangular brass tubes, which are connected by flexible plastic tubing. The cooling pipes are connected to a liquid cooling system with a monoethylene glycol and water mixture using non-spill and non-magnetic connectors. In addition, each module has a connection for pressurized air, which can be used for additional cooling, but its main intention is to flood the module box with dry air to lower the dew point and thus allow lower cooling temperatures without causing condensation inside the SDM.

#### 2.5.2 Modular housing and RF shielding concept

Each SDM is enclosed by a housing, which has to fulfil multiple purposes:

First of all, the housing constitutes the mechanical enclosure of each SDM. Second, it should be highly transparent for gamma radiation towards the field-of-view, because it encapsulates the gamma detectors. Third, it should be light-tight, because the photodetectors inside are very sensitive to light. Fourth, it should provide RF shielding and thus minimize RF interference between the PET and the MRI system. Finally, it should be a type of material that does not interfere with the MRI gradient system because of eddy currents. In particular, the last two aspects led to the design of a carbon fibre composite based housing, which combines good RF shielding properties with lower eddy current distortions, which will be discussed in detail in chapter 4.

For comparison, the housings of the Hyperion I system were made of a ceramic filled resin using stereolithography and were galvanically coated with 18 µm copper (Weissler et al. 2014). Using stereolithography, almost any shape can be produced, but the resulting housings were brittle, expensive and difficult to post process. Furthermore, the copper coating was anticipated as suboptimal for MRI compatibility because of its high conductivity.

The basic idea of the Hyperion  $II^{D}$  housing is to have a tubular carbon fibre reinforced shell, in which all other components are slid in. The tubular shell constitutes the main mechanical structure and the RF shield at the same time. Because of the mechanical strength of carbon fibre composites, thin walled (< 1 mm) but stiff tubes can be fabricated. Furthermore, it is advantageous that carbon fibre composites have a low density of about  $1.5 \text{ g cm}^{-3}$ . The gamma attenuation coefficient of carbon fibre composites at 511 keV is about  $0.13 \text{ cm}^{-1}$ , roughly 35% higher than that of water. Thus, only about 1% of the annihilation photons interact with a 0.8 mm carbon fibre shell, as it is used for the Hyperion II<sup>D</sup> housings.

A further advantage of carbon fibre composites is its mechanical strength and robustness. During operation, the gradient system is subject to strong vibrations because of Lorentz force interaction with the main magnetic field. Also the conductors of the gradient coils are embedded in a fibre reinforced composites. However, the gradient coils are based on electrical isolating fibres, e.g. glass fibres, rather than carbon fibres. Moreover, carbon fibre composites contain mainly pure carbon, which makes them throughout black and advantageous to construct a light-tight housing.

The mechanical structure of the SPU is supported by a fibre reinforced backplate. Both are attached with screws to the two inner end caps of the module. To ensure proper alignment, the SPU and the end caps of the module are fixed with dowel pins. This structure contains basically all electronic components of a SDM and is slid into the housing shell. The outer and the inner part of the end caps are screwed together with plastic screws.

On each side, a printed circuit board is placed between the inner and the outer end cap of the module. These circuit board are covered by a 18 µm copper plane and are mainly intended to complete the RF shielding of the SDM. Additional RF gaskets are used to connect the shielding circuit board with the carbon fibre shell electrically. To improve the electrical contact to the carbon fibre shell, the respective areas of the carbon fibre shell were roughened by sanding to break up the non-conductive epoxy matrix. On the front side, the shielding boards take a further functionality, as they host the connectors for the power cables and some capacitors for filtering.

The implementation of feedthroughs can be intricate if the construction space is limited. Here, the use of plastic optical fibres (POFs) simplified the design significantly, because they can be cut to length with a simple mechanical tool. The bare fibre ends can be directly clamped into the connectors of the transceivers, without requiring a special connector assembly. Thus, all feedthroughs could be realized as cylindrical holes, matched to the size of the respective cable or tubing (e.g. 6 mm for the liquid cooling and 2.2 mm for the POF). Cavities with sealing rings ensure the light-tightness of each feedthrough. Furthermore, openings in the RF screen of the shielding board could thus be minimized.

# **Chapter 3**

# Development of an MRI-compatible digital SiPM detector stack

#### **Copyright notice**

The following chapter is published in similar form under the creative commons license CC BY 3.0, Dueppenbecker et al. 2016.

# 3.1 Introduction

Advances in solid-state photon detectors paved the way to combine Positron Emission Tomography (PET) and Magnetic Resonance Imaging (MRI) into highly integrated, truly simultaneous, hybrid imaging systems. Based on the most recent digital SiPM technology, an MRI-compatible PET detector stack was developed, intended as a building block for next generation simultaneous PET/MRI systems.

The combination of its high performance, functional integration and expected MRI compatibility makes the digital SiPM a very promising device for building simultaneous PET/MRI systems. In this work, Philips Digital Photon Counting DPC 3200-22 digital SiPMs were used to develop an MRI-compatible detector stack to build up small animal simultaneous PET/MRI systems. The following section introduces the design of the detector stack, followed by an in-depth characterization and optimization of its MRI compatibility.

# 3.2 Design of the digital SiPM detector stack

The detector stack is composed of three assembly groups: the sensor tile, the interface board and two cooling pipes, as shown in figure 3.1. The sensor tile contains the digital SiPMs, whereas the interface board acts as a data acquisition and control unit with an interface to the singles processing unit (SPU) presented by Weissler et al. (2012b).

The top side of the sensor tile contains an array of  $8 \times 8$  digital SiPM channels with 4 mm pitch using Philips Digital Photon Counting DPC 3200-22 devices. The DPC 3200-22 combines four digital SiPM channels on one silicon die, the four channels sharing a common trigger, time stamping and communication unit. Each silicon die is



**Figure 3.1** MRI-compatible digital SiPM sensor tile, interface board and assembled detector stack with cooling pipes. The edge length of the quadratic sensor tile is 32.7 mm.

mounted with conductive glue onto the sensor tile and up to 48 bond wires along the top and bottom edge of each die connect the power and signal lines. All digital SiPMs on one sensor tile share the same bias voltage and are preselected for equal breakdown voltages. Each DPC 3200-22 die is connected to a dedicated clock and a synchronization line, which allows the configuration of a fine grained trigger and clocking network. A JTAG daisy chain connects all 16 dies for configuration. Data, clock, synchronization and configuration lines are single-ended 1.8 V CMOS lines. On the bottom side the sensor tile is equipped with decoupling capacitors, a digital temperature sensor, a 16 Mbit flash memory, and two 80-pin connectors. The Flash memory is used to store a unique identifier and calibration data for each sensor tile. Both connectors connect the sensor tile to the interface board with a stacking height of 6 mm. The sensor tile is split into two galvanically isolated halves to avoid a conductive loop through the connectors and the interface board. Although similar in functionality and dimensions compared to a conventional digital SiPM tile as presented by Degenhardt et al. (2010), the here developed sensor tile is an entirely new design, optimized for MRI compatibility and reliable cooling.

The central component of the interface board is a Xilinx Spartan 6 XC6SLX45 FPGA. It collects all measurement data, distributes clock and synchronization signals, configures the digital SiPMs and controls the supply voltage regulators. Because the digital SiPMs transmit all output data digitally, they are directly connected to the FPGA without any additional digitization or logic level adoption. Communication and forwarding of acquired data from the interface board to the singles processing unit uses low voltage differential signal (LVDS) lines. The interface board contains a digitally adjustable voltage regulator for the bias and reset voltage and a fixed 1.8 V regulator for the supply of the detector stack. In course of optimization, a fixed 1.2 V regulator for the FPGA core voltage was later on added to stabilize the supply voltage during gradient switching. The bias and reset voltage can be adjusted in 256 steps from 15 V to 34 V and 3 V to 4 V, respectively. Additionally, both supplies can be switched on/off and include a voltage and current monitor, as well as a hard-wired current limiter to protect the digital SiPMs in case of malfunction. The remaining space on the interface board is occupied by decoupling capacitors.

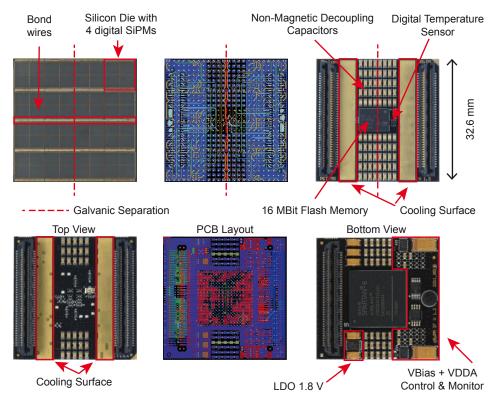


Figure 3.2 Implementation details of sensor tile (top row) and interface board (bottom row).

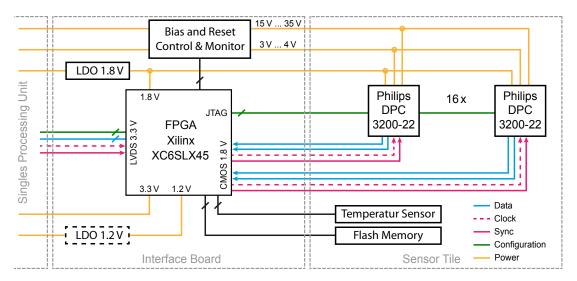


Figure 3.3 Functional overview of the detector stack. The sensor tile contains the digital SiPMs, a digital temperature sensor and a Flash memory. Data acquisition, configuration and power supply is controlled by the interface board. Acquired measurement and control data is bundled into one communication stream and forwarded to the singles processing unit. The low-drop voltage regulator (LDO) for the 1.2 V supply was added during optimization of the detector stack.

A functional overview of the whole detector stack is given in figure 3.3. Further implementation details of the sensor tile and the interface board are presented in figure 3.2. The data readout platform and firmware of the detector stack is described in Gebhardt et al. 2012.

The detector stack is intended to operate in enclosed module boxes. This mandates a reliable cooling system, if only for the reason to prevent overheating and keep the digital SiPM within its recommended operating temperature of 0 °C to 40 °C.

Beyond that, the performance of the digital SiPM depends on temperature. Although the temperature dependency of the digital SiPM is in principle lower than that of analogue SiPMs (Frach et al. 2009), temperature directly affects the breakdown voltage, the dark count rate (doubles every 7.5 K) and the switching characteristics, and thus also influences the photon detection efficiency  $(-0.33\%)^{\circ}$ C in the range of 15 °C to 25 °C), the dead time and the velocity of the integrated time stamper of the digital SiPM. For this reason, the design of the detector stack incorporated a liquid cooling system from the very beginning.

The basic elements of the cooling system are two rectangular brass pipes between the interface board and the sensor tile. Thermal pads couple those brass pipes to dedicated cooling surfaces on the interface board and the sensor tile. The cooling pipes are connected to a liquid cooling system with a monoethylene glycol and water mixture using non-magnetic and non-spill connectors, which allow disconnecting the filled cooling pipes without loosing coolant. More than 600 vias through the circuit board of the sensor tile improve thermal coupling between the the digital SiPMs and the cooling pipes. All voltage regulators are placed directly opposed to the cooling pipes on the bottom side and are connected via thermal vias to the cooling surfaces. The cooling system is intended to operate at temperatures above the dew point to avoid condensation.

A major concern was to minimize  $B_0$  distortions by avoiding ferromagnetic components. However, the majority of electronic components contain nickel in their surface finishes or iron in their lead frames. The availability of dedicated non-magnetic components is very limited and custom-made, non-magnetic components are in many cases impracticable because of high development costs, especially for small lot sizes. Wherever possible, non- to weakly magnetic standard components were used. The selection process was primarily based on screening components with permanent magnets and acquiring  $B_0$  field maps by MRI measurements, because information about magnetic properties, e.g. from data sheets, is very limited. Only the connectors and most capacitors are explicitly non-magnetic components.

Capacitors play a twofold role in MRI-compatible electronic design: They are required to provide a stable power distribution network and thus can influence RF interference, but they are also a major source of  $B_0$  distortions, because the electrodes of today's commonly used multi layer chip capacitors (MLCC) are usually made of nickel. Only few vendors offer non-magnetic capacitors and available case sizes, or rather capacitance density, is severely limited compared to standard components. Large case sizes are undesirable, not merely because of construction space, but rather because of increased lead inductance, which dominates net component impedance at higher frequencies. Wherever possible, non-magnetic capacitors in the smallest available package were used. However, the interface board still contains some high-capacity magnetic capacitors in the smallest available case size, because suitable non-magnetic capacitors were unavailable.

Another source of ferromagnetic material is the surfaces finish of the circuit boards. Both circuit boards are fabricated with an electroless nickel immersion gold (ENIG) finish, which is an established and widely used surface finish in electronic industry and provides a very reliable surface for wire bonding. Having a reliable surface for wire bonding is crucial, because all signal and power lines of the digital SiPM are wire-bonded and a single bond fault can cause malfunction of an entire sensor tile. Although selected suppliers offer nickel free surface finishes, these were not verified for wire-bonding of the digital SiPM at design time.

Most types of components used for the detector stack were known by experience to be basically operational inside strong magnetic fields, but almost no information about possible performance degradations or limitations was available. Besides the digital SiPMs, also the FPGA, voltage regulators, Flash memory, temperature and voltage sensors are active semiconductor devices and thus potentially susceptible to magnetic fields. However, actual effects are difficult to determine in advance, because the devices must be in operation to observe effects. Thus the investigation of interference effects had to be done gradually during the development of the detector stack.

Both circuit boards are designed with particular care to reduce electromagnetic interference. Return paths for signal and power lines are placed close together, including the pin assignment of the connectors. Where possible, signal lines are routed on inner layers. Low impedance connection of decoupling capacitors and power pins to the supply planes took highest priority during all design phases.

## 3.3 Experimental setup

For testing, the detector stack is mounted on a singles processing unit (Weissler et al. 2012b), which supplies power and provides the communication interface to exchange data via an optical gigabit Ethernet link with a data acquisition and control computer. Furthermore, the singles processing unit distributes the reference clock signal from an optically-connected external clock source. Raw detector and status data, including data from the temperature sensor and voltage monitors, is stored on disk and post-processed with Java and Matlab. To reduce the dark count rate and dead time, 20% of the most

noisy digital SiPM cells were disabled. All measurements were carried out with 2.5 V overvoltage and the cooling temperature was set to approximately  $10 \,^{\circ}\text{C}$ .

Measurements inside the MRI were performed on a 3 T Philips Achieva MRI scanner with 60 cm bore diameter. The detector stack and the singles processing unit are therefore mounted in a PET module on a gantry, as shown in figure 3.4 (a), resulting in the detector stack being positioned approximately 11 cm above the isocentre of the MRI. Measurements outside the MRI were performed with a detector stack mounted on a bare singles processing unit in a light-tight cabinet and, to simplify the installation of test equipment, the connector between the detector stack and the singles processing unit was extended with an extension board, as shown in figure 3.4 (b). The extension board is a straightforward extension of all connector pins between the singles processing unit and the detector stack and does not contain any active components.

To be independent of a specific scintillator configuration, the detector stack was illuminated with short laser pulses instead of scintillation light. There is no known reason to anticipate any influence of the MRI environment on the scintillation process or the light transport. The use of laser pulses eliminates the randomness of radioactive decay from our experiments and a second detector as timing reference becomes redundant. Furthermore, the use of laser pulses with a fixed frequency constitutes a uniform sampling in time. This not only allows a direct time domain analysis down to single events, but also offers the opportunity for frequency domain analysis using Fourier transformation, which is not possible with random events generated by radioactive decay.

As illustrated in figure 3.5, laser pulses are generated by an Advanced Laser Diode Systems EIG1000D 410 nm pulsed picosecond laser and are coupled into a 25 m long optical fibre. At the opposite end of the fibre, laser pulses are coupled out and attenuated 10 times by a neutral density filter to achieve photon count values similar to scintillation light. A Thorlabs ED1-S20 microlens diffuser widens the laser pulses before they hit the detector. To illuminate the detector stack inside a closed PET module, a 30 mm hole was milled into the housing and a fixture to hold the optical fibre, the attenuator and the diffuser was attached to it.

Each laser pulse is triggered by an electrical trigger signal. Measurements presented in this work were performed with a trigger rate of 100 kHz to prevent saturation of the data readout chain, whereas the reference clock for the digital SiPMs is supplied at 100 MHz to the singles processing unit and is later on doubled to 200 MHz inside the FPGA of the interface board. Consequently, any jitter or drift between the trigger signal and the digital SiPM reference clock will directly influence measured timestamps. Because a suitable low-jitter, dual-frequency clock generator was not available, a Xilinx SP605 FPGA evaluation board was programmed to generate the trigger signal and the reference clock. Both signals are derived with a counter from the same on-board oscillator and run synchronously with a fixed phase relationship. Measured jitter between the reference clock and the trigger signal was 22 ps FWHM. The trigger signal

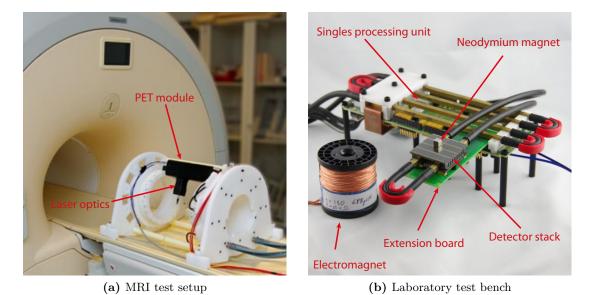


**Figure 3.4** Test equipment on MRI table and bench top. (a) For testing purposes the detector stack is mounted in a PET module on a gantry. The black build-up contains the laser optics and is connected via an optical fibre to the laser unit outside the MRI room. (b) Test bench with detector stack, extension board and singles processing unit. Shown magnets were used to simulate static and dynamic magnetic fields, without requiring an MRI system. The extension is a straight-forward connection of all connector pins between the interface board and the singles processing unit to simplify the installation of test equipment. It was only used for experiments outside the MRI.

for the laser is directly connected to the trigger input of the laser unit, whereas the reference clock signal is connected to a Firecomms EDL 1000T-EVB POF converter and transmitted via plastic optical fibres (POF) to the singles processing unit.

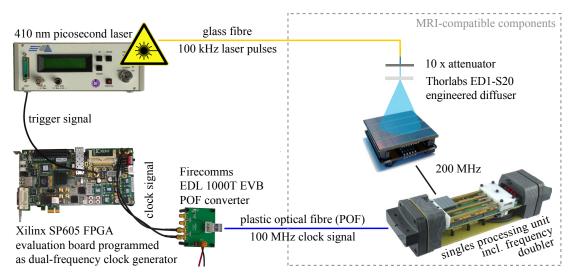


**Figure 3.5** Clocking infrastructure used for synchronized laser excitation of the detector stack. The FPGA evaluation board is used as low-jitter, dual-frequency clock generator to generate the reference clock and the trigger signal. Optical fibres allow the operation of the laser and clock generator safely outside the MRI room.

# 3.4 Methods used to measure PET/MRI interference

# 3.4.1 Quantification of B<sub>0</sub> distortions

Quantification of  $B_0$  distortions followed the phase imaging technique as described in the ACR MRI Quality Control Manual (Weinreb et al. 2004). Test objects were placed centred on a cylindrical, oil-filled image quality phantom with an inner height of 10 cm and a diameter of 38 cm (figure 3.6). The alignment of test objects was consistent to their intended mounting position on a PET ring. Presented images are transverse 5-mm-thick slices centred through the device under test with a pixel size of  $1.76 \times 1.76 \text{ mm}^2$ . Presented investigations are independent of a specific field of view and focus on the spatial extent of distortions of single components. Thus, presented figures show and compare plain field maps, but are corrected for distortions caused by the phantom itself by subtraction of a reference scan of the phantom without any test object placed on it.

### 3.4.2 B<sub>0</sub> influence on detector stack

To investigate the influence of static magnetic fields, the detector stack was operated inside a 3 T Philips Achieva MRI system. Although straight forward, this approach makes it difficult to identify critical components, because the large extent of the main magnetic field allows no selective exposure. On the other hand, testing of individual components in operation within an MRI is restricted because of component interdependencies. Thus, to identify components that are sensitive to static magnetic fields, tiny neodymium magnets with edge lengths of 4 mm to 10 mm were used to expose



**Figure 3.6** Setup to measure  $B_0$  distortion maps. Test objects are placed centred on an oil filled MRI phantom.

components of electronic assemblies selectively to high magnetic fields. The measured field strengths of the magnets used were about 0.5 T at the poles and 0.25 T along the sides. This is clearly lower than in a 3 T MRI system and consequently achievable effects will also be weaker. However, this is secondary for this purpose, because the aim of using permanent magnets is the identification of critical components rather than the quantification of interference effects. The use of small permanent magnet is thus intended as method to amend the investigation inside an MRI and not to substitute them.

#### 3.4.3 Gradient influence on detector stack

In previous experiments, the z-gradient caused the strongest interference effects (Wehner et al. 2014). Therefore, the investigation focused on the influence of the z-gradient. An echo planar imaging (EPI) sequence with artificially high z-gradient switching served as a worst-case scenario to emphasize interference effects. Obtained z-gradient slew rate of the test sequence is  $198 \,\mathrm{Tm^{-1} \, s^{-1}}$  at a maximum gradient strength of  $30 \,\mathrm{mT \, m^{-1}}$ . Echo and repetition time are set to  $TE = 12 \,\mathrm{ms}$  and  $TR = 24 \,\mathrm{ms}$ , the shortest possible values. The EPI factor is set to 49, which results in an almost continuously switching of the readout gradient during the whole sequence. This sequence is solely intended to create a worst-case scenario to investigate the influence of gradient switching on the detector stack. It does not produce any valuable MRI images.

Inside an MRI system, the installation of measurement equipment and the selective exposure of individual components is difficult. Similar to the use of permanent magnets, a simple solution to emulate locally limited magnetic gradient fields without requiring an MRI system was required. Therefore, an electromagnet with 190 turns of copper strand on a 20 mm core was built up, driven by an audio power amplifier and a signal generator. The coil carrier contains an axial hole with 10 mm diameter, which allows the illumination of a small area of the detector stack through the coil. This configuration produces slew rate amplitudes up to  $260 \,\mathrm{T \, s^{-1}}$  using a 10 kHz, 2.5 A RMS, sinusoidal waveform. In close proximity to the core of the coil, the change in magnetic flux is thus even higher than the MRI system used can provide, but the spacial extend is very limited, as intended. The achieved absolute field strength is only about 4 mT.

#### 3.4.4 Radio frequency interference

RF interference measurements were performed using the spurious signal sequences provided by the service tools of Philips Achieva MRI systems. This sequence is a modified spin echo imaging sequence with disabled gradients and RF power reduced to a minimum. Essentially, the MRI system is used as a receiver only. Image data was exported as DICOM data and post processed with MATLAB to extract the noise distribution as a function of frequency.

The RF investigations presented in this work are intended to demonstrate the significance of a proper decoupled power distribution network for RF interference with the MRI system. Therefore, all decoupling capacitors of a sensor tile were removed and the resulting RF noise figures were compared to a fully equipped sensor tile. To emphasis the effect, the RF shielding of the detector module was replaced by an RF-transparent glass fibre housing. The MRI coil used was a local transmit and receive, 12-leg-birdcage resonator, identical as described in Wehner et al. 2015.

# 3.5 Results

#### 3.5.1 B<sub>0</sub> distortions caused by detector stack

Figure 3.7 summarizes the results of the  $B_0$  distortion quantification. As shown in figure 3.7 (a-c), the MRI-compatible sensor tile and interface board cause considerably less  $B_0$  distortion than a conventional digital SiPM tile, that was not optimized for MRI compatibility. A subsequent detailed analysis obtained by disassembling multiple sensor tiles and rescanning individual components revealed that the remaining distortions are dominated by the bare circuit boards, though the amount of distortion varies for different batches, as shown in figure 3.7 (d, e). By design, the ENIG surface finish used contains a nickel layer and was thus suspected of causing the distortions. Figure 3.7 (f) confirms this assumption: after grinding the ENIG layer off, the remaining circuit board with bare copper traces caused no ferromagnetic distortions any more. In fact, remaining distortions are slightly diamagnetic.

Figure 3.7 (g) shows the  $B_0$  distortions caused by an assembled detector stack, composed of an interface board and a sensor tile. The distortions of the detector stack are

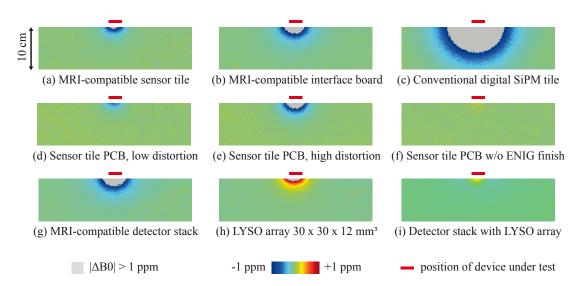
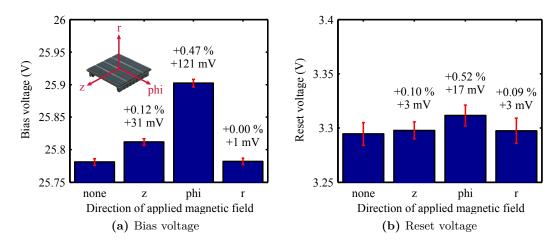


Figure 3.7  $B_0$  distortion maps. Shown are the deviations of the main magnetic field caused by the respective device under test in the transverse plane. For proper visualization and ease of comparison, the colour coding range is limited to +/-1 ppm and distortions stronger than 1 ppm are greyed.

clearly dominated by ferromagnetic materials. In contrast, common scintillator materials for PET – in particular BGO and LSO – are diamagnetic (Yamamoto et al. 2003). Verification of LYSO by scanning a pixelated  $30 \times 30 \times 12 \text{ mm}^3$  LYSO array, as shown in figure 3.7 (h), confirmed that LYSO behaves diamagnetically as well and causes distortions with the opposite sign. In their intended application, the detector stacks will be placed on top of the scintillator array and thus both effects will superimpose. Figure 3.7 (i) shows the net B<sub>0</sub> distortions caused by the detector stack in combination with the LYSO array. In this particular configuration both distortions almost cancel out.

#### 3.5.2 B<sub>0</sub> influence on detector stack

Operating the detector stack inside the main magnetic field of the MRI revealed slightly decreased photon count values, as reported in Dueppenbecker et al. 2012b. This effect could be traced back to a shift of the bias voltage, which directly influences the photon detection efficiency of the digital SiPM. As shown in figure 3.8 (a), the effect is directional. Depending on the alignment, the originally set bias voltage of 25.78 V shifted by up to 121 mV (0.47 %), although the shift in the default installation position is comparable low with 31 mV (0.12 %). In particular, magnetic fields parallel to the circuit board cause a voltage shift, whereas perpendicular magnetic fields show no significant effect. The same voltage regulator is used to control the reset voltage and measurements presented in figure 3.8 (b) confirm a similar behaviour. Although the observed absolute shift is about eight times smaller, the relative change is comparable and suggests a gain dependency.



**Figure 3.8** Directional effects of a 3 T magnetic field on voltage regulators of (a) the bias voltage and (b) the reset voltage. Whereas magnetic fields perpendicular to the circuit boards (r-direction) cause almost no effect, magnetic fields parallel to the circuit boards (z- and phi-direction) do. The given directions relate to the cylindrical coordinate system of the MRI and the PET module installed in default position. Actual measurement data were obtained by rotating the PET module inside the MRI bore. Red bars indicate the standard deviation of the measured voltage noise floor.

Probing individual components with small permanent magnets partially reproduced the effects measured above and identified the low drop voltage regulators as being sensitive to magnetic fields. Measurements with different gain settings and magnet orientations, shown in figure 3.9, confirmed that the observed voltage shift scales with the set gain of the voltage regulator and depends on applied field direction.

#### 3.5.3 Gradient influence on detector stack

#### Gradient influence on bias voltage and energy resolution

As previously reported (Wehner et al. 2014), the energy resolution of PET measurements decreased during MRI gradient switching. This effect correlates with an instability of the bias voltage during gradient switching and is explained by the direct impact of the bias voltage on photon detection efficiency. The same effect is reproducible in lab by means of simulating MRI gradients with an electromagnet. Repeating the measurement at different bias voltage levels, as presented in figure 3.10 (a), revealed a linear relationship between the set bias voltage and the voltage ripple. This indicates, that the ripple is injected into the control loop of the voltage regulator and thus gets amplified, depending on the set bias voltage.

Based on this finding, the control loop of the regulator was redesigned and stabilized with an additional feedforward capacitor. This reduced the voltage ripple significantly and stabilized energy resolution. Measured energy resolution with laser excitation using the unmodified interface board was 10.6% without gradient switching and degraded to

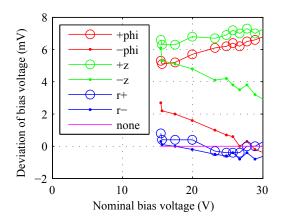


**Figure 3.9** Gain dependent effect of magnetic fields on the bias voltage, measured with a Prema 5017 digital multimeter. A small permanent magnet was placed directly on the voltage regulator. Although the absolute deviation is less than achievable within an 3 T MRI system, the magnet is sufficiently strong to reproduce measurable effects on individual components. The effect shows an offset and a directional, gain dependent component. The gain dependency indicates that the initial distortion is amplified and thus might be caused by shifted voltage or comparator deviation.

11.0% during application of the MRI gradient sequence (figure 3.11). The improved interface board showed 10.5% energy resolution in both cases. A spectral analysis of photon counts over time during MRI gradient switching points out the effect more clearly, as shown in figure 3.10 (b). The unmodified interface board shows a main peak at 1120 Hz, which corresponds to the main switching frequency of the readout gradient. After stabilising, the main peak is reduced by more than  $27 \, dB$  and close to the noise level.

Although the reset voltage regulator is based on the same topology as the bias voltage regulator, the amplification factor and thus the resulting voltage ripple is about eight times lower and no consequences could be attributed to that. Nevertheless, for reasons of precaution the reset voltage controller was redesigned in the same way.

#### Gradient influence on timing

The test environment offers for the first time the possibility to measure the timing jitter of individual events, and this both inside and outside the MRI. The red curve of figure 3.12 shows the timing jitter of a single digital SiPM channel during the start of the gradient test sequence. It reveals that individual timestamps deviate up to 250 ps during MRI z-gradient switching and that the jitter directly correlates with the gradient pulses. This behaviour is also reflected in the frequency domain as a clear peak according to the main gradient switching frequency of the MRI sequence used, as shown by the red curve in figure 3.13.

Simulated sinusoidal gradient fields with an electromagnet reproduced similar effects. Repeated measurements at different positions showed, that the magnitude of timing

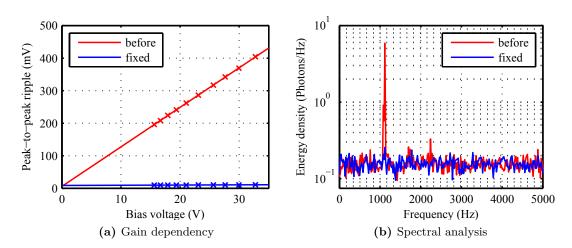


**Figure 3.10** Effect of induced voltage ripple on the bias voltage. The voltage ripple has been induced with an electromagnet. (a) Measured voltage ripple before and after stabilizing the voltage regulator at different output voltages. The gain dependency of the ripple indicates, that induced voltage variations get amplified by the voltage regulator. (b) Spectral analysis of photon count values over time during MRI gradient test sequence. The main peak at 1120 Hz corresponds to the main gradient switching frequency of the used MRI test sequence. After stabilising, the main peak is reduced by more than 27 dB.

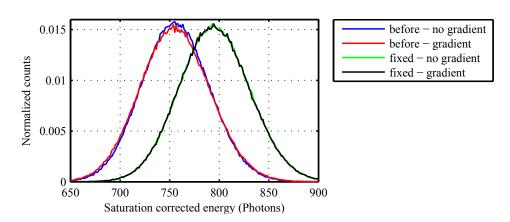
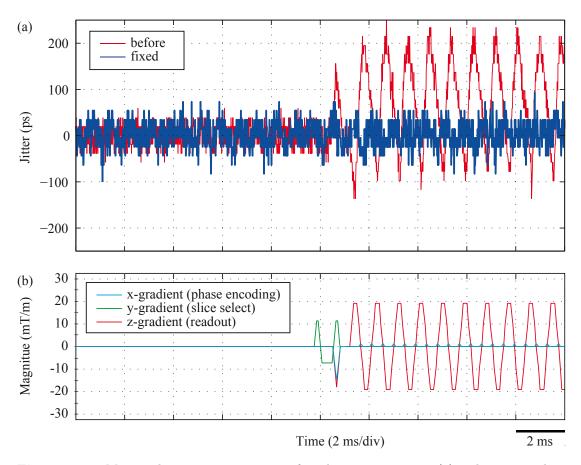
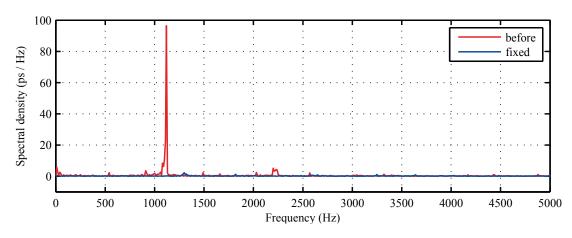


Figure 3.11 Energy resolution saturation corrected before, after, with and without gradients. Measured energy resolution with laser excitation using the unmodified interface board was 10.62% and 11.01% with and without MRI gradient sequence, with a mean of 756 and 755 photons, respectively. The improved interface board showed 10.53% and 10.51% energy resolution with and without gradient switching with a mean energy of 795 photons under both conditions. The energy resolution is mainly limited by photon counting statistics and the different mean photon count values are caused by disassembling and reassembling the experimental setup.



**Figure 3.12** Measured timing jitter at start of gradient test sequence (a) and corresponding gradient sequence diagram (b). The initial design was affected by timing jitter up to 250 ps and the time course of jitter is directly correlated with the gradient sequence. In contrast, the improved interface board with local core voltage control operates stable during gradient switching.



**Figure 3.13** The spectral analysis of timing jitter clearly reveals the main gradient switching frequency of the MRI gradient test sequence. The fixed interface board with an additional voltage regulator for the core voltage supply of the FPGA is immune to this effect.

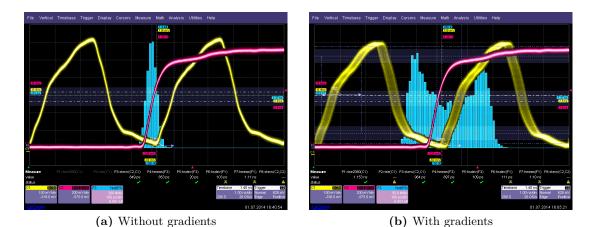
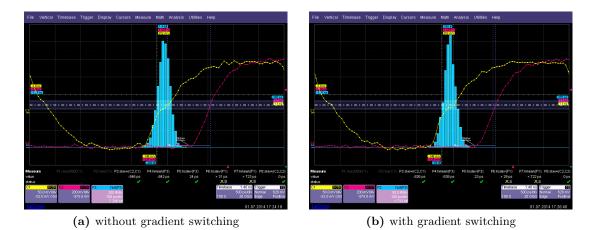


**Figure 3.14** Clock jitter measured at the connector of the interface board without (a) and with gradients (b). The red curve shows the trigger signal of the picosecond laser and the yellow curve is the measured clock output signal at the connector of the interface board. The shape and magnitude of the clock signal is preserved during gradient switching, but the signal is shifted in phase. The blue histogram shows the jitter distribution. Gradients were applied with a small electromagnet. The time scale is 1 ns per division for the clock and trigger signal and 100 ps per division for the histogram data.

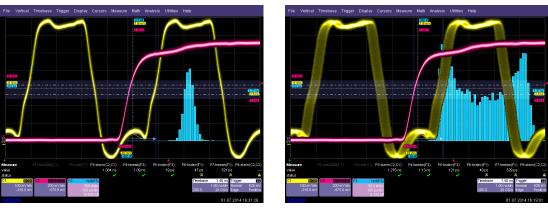
jitter varies with the position of the electromagnet. The timing jitter was strongest when the electromagnet was placed on the extension board, rather than directly on the detector stack. This indicated, that the primary source of timing jitter is not induced in the detector stack itself but in the supporting infrastructure, and subsequently propagates, e.g. via the power rails or the clock signal.

Figure 3.14 shows the output clock signal, measured with an oscilloscope at one of the connectors towards the sensor tile. It clearly depicts, that the output clock is affected by phase jitter during gradient switching, but the shape and the amplitude of the clock signal are preserved. However, an examination of the input clock signal revealed, that the clock signal enters the interface board cleanly (figure 3.15). Also a change of the slew rate settings of the clock output drivers showed no effect (figure 3.16). Altogether, this suggests that the distortion of the clock signal happens inside the core logic of the FPGA. The FPGA output drivers for the clock signals are powered by the 1.8 V supply rail, whereas the internal logic of the FPGA is powered by the 1.2 V rail supplied by the singles processing unit. For testing purpose, the 1.2 V supply was bypassed and directly supplied by an external laboratory power supply. This eliminated the previously observed timing jitter.

To verify this achievement inside the MRI, a dedicated voltage regulator for the 1.2 V supply had to be integrated onto the interface board, which required a slight redesign and a new production run of the circuit boards. Following measurements inside the MRI confirmed previous laboratory measurements: the timing resolution remains stable, even during heavy and continuous gradient switching, as proven by the blue curve in figure 3.12. A spectral analysis as shown in figure 3.13 reveals the effect



**Figure 3.15** Clock input jitter without (a) and with (b) gradient switching. The yellow trace represents the clock signal measured at the input of the interface board and the red trace the trigger signal of the clock generator, both on a timebase of 500 ps per division. The blue bar plot represents the respective jitter histogram on a timebase 100 ps per division. Gradient switching did not influence the clock jitter at the input of the interface board. Thus, the degradation of the clock must happen on the interface board.



(a) without gradient switching

(b) with gradient switching

**Figure 3.16** Clock output jitter with increased slew rate without (a) and with (b) gradient switching. The yellow trace represents the clock signal at the output of the interface board and the red trace the trigger signal of the clock generator, both on a timebase of 1 ns per division. The blue bar plot represents the histogram of timing jitter on a timebase of 100 ps per division. Increasing the slew rate showed no effect on timing jitter and could not solve observed timing degradations during gradient switching.

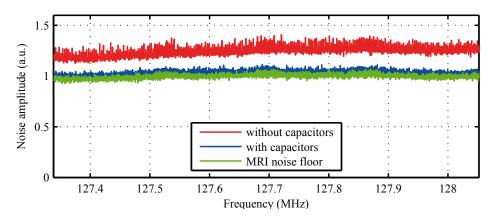


Figure 3.17 RF noise figure of a single detector stack with and without decoupling capacitors. To emphasis the effect, the detector stack was mounted on a PET module without RF shielding.

even more clearly: whereas the jitter spectrum of the initial design (red curve) shows a clear peak corresponding to the main gradient switching frequency, the improved design (blue curve) shows an almost flat jitter spectrum.

Another initially suspicious component was an FPGA-internal phase locked loop (PLL), which is used to buffer, double and filter the clock signal. This PLL uses internally a voltage controlled oscillator, which makes it potentially susceptible to supply voltage variations. The PLL is powered by the 3.3 V rail, which is supplied by the singles processing unit, likewise the 1.2 V supply initially was. However, a modified firmware with a direct clock forwarding scheme that omitted the PLL didn't show any indication that the PLL is influenced by gradient switching.

#### 3.5.4 RF interference

In figure 3.17, the noise floor of a regular sensor tile in operation is compared to a sensor tile with all decoupling capacitors removed. Without decoupling capacitors, the noise floor increased by about 25% and digital noise patterns became visible. The measurement was carried out with a single detector stack on a PET module without radio frequency shielding to demonstrate the effect more clearly.

# 3.6 Discussion

 $B_0$  distortions caused by the detector stack are significantly reduced compared to a conventional design. Apart from most capacitors and connectors, the improvements were mainly achieved by careful selection of non- to weakly-magnetic standard components. Especially for small batches, the use of standard components is beneficial to control costs and lead times. Remaining ferromagnetic distortions attributable to the sensor tile are dominated by the surface finish of the circuit boards and could be further reduced in future designs, either by using a nickel-free surface finish or by reducing the

amount of gold-plated areas. However, the amount of nickel contained in the surface finish varies because of process variations and is difficult to predict.

The fact that nowadays common PET scintillators are diamagnetic can be used to compensate for distortions caused by ferromagnetic materials. In the shown example, the diamagnetic effect of LYSO compensates to a great extent for the distortions caused by the detector stack. The complete avoidance of ferromagnetic materials for an MRI-compatible PET detector with BGO, LSO or LYSO scintillators is therefore not essential and a certain amount of ferromagnetic components is actually desirable, which makes it difficult to predict and control resulting  $B_0$  distortions.

Easing the strict requirement for non-magnetic materials could be particularly beneficial for capacitor selection. As shown, capacitors have a two-fold impact on MRI compatibility: they influence  $B_0$  distortions and RF interference. Selected suppliers offer non-magnetic capacitors, but available capacity densities are very limited and they are expensive. If carefully used, standard capacitors with nickel electrodes in the smallest available packages might be a viable choice to reduce construction space, costs and lead times. MRI compatibility thus clearly benefits from the trend to miniaturization of electronic components. Yet, for commercial production this approach remains troublesome until the magnetic properties are clearly specified and monitored. The approach of tightly specifying magnetic properties of all components may sound obvious, but the required effort should not be underestimated. Adapted passive shimming by either additional diamagnetic, paramagnetic or ferromagnetic materials might be a possible solution to compensate for variations, although it introduces additional complexity and might be field strength and temperature depended because of ferromagnetic saturation. In the end, a combination of both approaches might provide the most viable and cost-effective solution.

Magnetic fields caused voltage regulators to drift, but the drift does not affect detector performance itself, because it can be easily compensated for by performing detector calibration inside the MRI, e.g. determination of breakdown voltage and operating point. However, the observed effects depend on detector orientation and are likely to increase at higher field strengths and should therefore be carefully considered for future developments. The results presented here do not reveal the underlying physical effects to explain the observed deviations. To correctly interpret the directional dependency, it would require detailed information of the internal circuit layout. According to the data sheets, both voltage regulators use an internal 0.6 V voltage reference. Considering the observed gain dependency, it suggests that the magnetic field directly impacts the voltage reference or the corresponding comparator circuit. Consequently, a very broad range of devices could be susceptible to magnetic fields, e.g. all devices using a voltage reference or comparators. All such devices might in principle remain operational inside an MRI, but their operating range and performance could be affected. Gradient-induced voltage variations influenced the detector stack most seriously, although the induction itself took place in the supporting infrastructure and propagated via the power rails to the detector stack. In particular, the effect on the FPGA core logic is remarkable. Variations of the supply voltage affected the switching characteristics of the FPGA core logic and led to phase jitter. Here the effect was identified because there was a very special interest in timing resolution. However, changing switching characteristic will reduce the jitter margin of any digital logic and could thus cause various malfunctions. In practice, actual effects might be more concealed, e.g. increased bit error rates on data links.

Inexpensive magnets - tiny permanent magnets and a self-wound electromagnet turned out to be efficient ways of investigating  $B_0$  and gradient interference. Both allow the induction of interference effects without requiring access to an MRI, which usually is a very expensive and scarce resource, and thus help to shorten development cycles. The field range of both magnets is small compared to an MRI and thereby allows selective testing and identification of critical components. Furthermore, working with small magnets on a test bench allows the use of test equipment without worrying about MRI interference or safety issues.

The synchronized excitation with laser pulses proved to be very powerful. It allows the measurement of effects at a single event level, enables frequency domain analysis and thus reveals effects that are otherwise hard to measure. In particular, frequency domain analysis can be very sensitive and useful to trace back characteristic frequency components. The presented measurement setup is MRI-compatible, because only passive, optical components enter the MRI room. This is a huge advantage compared to electrical test equipment, e.g. an oscilloscope with active probes, which is subject to MRI interference itself. Beyond PET/MRI interference characterization, the synchronized laser excitation method could also be used to support the development of future time-of-flight PET systems: as time resolution strives towards 100 ps and below (Schaart et al. 2010), clock jitter, caused by whatever source, becomes increasingly important.

Being able to measure the effect at a single event level opens up entirely new possibilities: here this knowledge was used to optimize and eliminate initially observed degradations, but it could also be used to calculate the influence on single events caused by specific MRI sequences. This potentially offers the opportunity to compensate interference effects during post-processing, e.g. in case that interference effects are unresolvable or too costly to fix.

# 3.7 Conclusion

The developed detector stack allows the operation of digital SiPMs simultaneously and stably inside a 3 T MRI system. Based on the gained experience, the digital SiPM

simplifies system integration and MRI compatibility, because it requires no external digitization and directly interfaces to an off-the-shelf FPGA. This reduces the risk to couple in electromagnetic distortions, saves - potentially magnetic - components as well as construction space. Furthermore, the low and positive bias voltage of about only 30 V allows the design of a very compact bias voltage supply with standard components and tight circuit board routing.

The development of the here presented detector design follows a very aggressive approach to integrate as much as possible detector infrastructure inside the MRI. This gives the advantage of less cabling and scales more easily with increasing system geometries and requirements. Although the MRI is a very challenging environment to operate electronic equipment, the here presented results show that it is possible without sacrificing detector performance. The required detector electronics do not necessarily have to be more complex compared to conventional ones, but careful design and verification is required.

Observed  $B_0$  effects on voltage regulators are notable, but do not impact detector performance. Most severe interference effects were caused by gradient-induced supply voltage variations and initially caused a degradation of energy and timing resolution. The root cause of both effects was identified and after optimization the detector stack operates very stably without performance degradations, even during heavy and continuous gradient switching. All observed MRI interference effects could be ascribed to the detector infrastructure. In particular, no evidence was found that the performance of the DPC 3200-22 digital SiPM itself is degraded by the MRI system.

The detector stack was developed to facilitate good system integration and was already used to build three preclinical PET/MRI systems (Weissler et al. 2012a). The systems are in use to evaluate the performance and PET/MRI interference of the digital SiPM on system level (Schug et al. 2015a,b,c, Wehner et al. 2015), including preclinical imaging studies (Weissler et al. 2015), and further research is ongoing.

The next development steps of the detector stack should focus on reducing the overall stack height, which is important for further integration into small animal as well as whole body clinical systems. This could, for example, be achieved by an integration of the interface board with the singles processing unit and could reduce the total height of the PET detector electronics to less than 10 mm. Although the detector stack was developed for PET/MRI, the presented design is also suitable for SPECT/MRI or PET only systems.

Future PET/MRI system designs might position the PET detector closer to the MRI gradient and RF systems, and eventually also to higher field strengths. It is likely that this will emphasise interference effects and may requires further optimization. The methods presented here should provide the right tools to support those developments.

# Chapter 4

# Development and characterization of a gradient-transparent carbon fibre composite RF shield for simultaneous PET/MRI

The simultaneous combination of PET and MRI entails numerous engineering challenges. A very specific one is the construction of MRI-compatible RF enclosures, which shield electromagnetic interference between the PET and the MRI system whilst at the same time minimizing gradient-induced eddy currents. In contrast to conventional copper screens, carbon fibre composites promise to fulfil this requirement - and even some more. The focus of the following chapter is to characterize the RF shielding efficiency of carbon fibre composites and to investigate if carbon fibre composites can outperform conventional copper based shielding for PET/MRI.

# 4.1 Introduction

Electromagnetic interference is a ubiquitous issue in electrical engineering. However, it is of particular importance for PET/MRI, since MRI systems entail very sensitive receivers as well as strong transmitters of electromagnetic radiation. Furthermore, the MRI gradient system presents a source of strong, time varying magnetic fields and thus interacts with conductive materials by inducing eddy currents.

Common RF shielding approaches are predominantly based on high conductivity materials, in particular metals. Among all metals, copper is usually the most popular shielding material, because of its high conductivity, good processability, availability and reasonable cost. Naturally, copper was also the initial choice for most PET/MRI systems, as listed in table 4.1, although its high conductivity poses the problem of eddy currents.

The problem of eddy currents is well known and has accompanied MRI from the very beginning. In order to reduce the formation of eddy currents, there are essentially two approaches: on the one hand, minimizing the thickness of the shields to reduce conductance, and on the other, structuring the shield to break up conductive paths.

Multiple studies (Peng et al. 2014, Weissler et al. 2014, Yoon et al. 2012) determine the thickness of the shield based on the skin depth, i.e. usually 3 to 5 times the skin depth are argued to be sufficient for RF shielding, although there is the opinion that less than one skin depth would be optimal from an MRI point of view to reduce the influence of eddy currents (Carlson 1994). The skin depth characterizes the exponential decrease of current density in a material. In a good conductor, the skin depth  $\delta$  is approximately reciprocal to the square root of the frequency f, conductivity  $\sigma$  and permeability  $\mu$  of the material:

$$\delta = \frac{1}{\sqrt{\pi f \sigma \mu}} \tag{4.1}$$

In copper the skin depth is  $9.3 \,\mu\text{m}$  at  $50 \,\text{MHz}$  and  $3 \,\mu\text{m}$  at  $500 \,\text{MHz}$ . The proposed values of 3 to 5 times the skin depth corresponds to  $26 \,\text{dB}$  to  $43 \,\text{dB}$  of attenuation. Consequently,  $18 \,\mu\text{m}$  to  $29 \,\mu\text{m}$  of copper should be sufficient for a  $3 \,\text{T}$  PET/MRI system, whereas the same criterion is met by  $11 \,\mu\text{m}$  to  $19 \,\mu\text{m}$  of copper for a  $7 \,\text{T}$  PET/MRI system. Coincidentally, copper foils of  $10 \,\mu\text{m}$  to  $35 \,\mu\text{m}$  are very commonly used in industry for printed circuit board fabrication and are thus easily and inexpensively available, which is likely to have influenced actual design decisions. Considerably thinner layers would be difficult to realize as foil and would require more complex fabrication techniques, e.g. electroplating, sputtering or vacuum deposition.

Structuring the shields is intended to break up the eddy current flow paths and thus reduce the formation of eddy currents from the outset. Whereas the aim of structuring is very clear, the criteria for structuring are not that clear from the previously mentioned studies, which suggest that material structures were probably determined by experience as well as trial and error approaches.

Some studies mention the use of aluminium and gold instead of copper (Hong et al. 2013, Maramraju et al. 2012), but without a clearly apparent reason or benefit.

During recent years, carbon fibre composites have caught the attention of PET/MRI engineers. Catana et al. 2006 mentions the use of a carbon fibre composite tube as structural support for a 7 T preclinical PET/MRI insert at UC Davis, but initially still used copper foil as the RF shield. The system was successively improved to incorporate two concentric carbon fibre tubes for electromagnetic shielding and placing the PET detector in-between (Peng et al. 2014, Peng 2011). Both tubes are specified as "carbon fiber shielding (purchased from CST Composites, Caringbah, NSW, Australia)" and have a wall thickness of 1.5 mm. Unfortunately, the kind of carbon fibre composite is not further specified, but the figures shown suggest that filament wound tubes were used. In the course of the above mentioned studies, the length of the tubes was varied and was shown to influence shielding efficiency significantly.

Independently of this development, the idea of using carbon fibre shielding as RF enclosure also evolved during the development of the Hyperion II<sup>D</sup> system (Dueppenbecker et al. 2012a, Wehner et al. 2014, Weissler et al. 2012a). Here, however, the approach is to use custom made module boxes instead of carbon fibre tubes. Both

**Table 4.1** Survey of RF shields used in PET/MRI systems. Most PET/MRI systems use highly conductive metallic foils for RF shielding, in particular copper foils. The common approach to reduce eddy currents is to minimize the shield thickness and to break up eddy current flow paths by structuring.

System and technology <sup>1</sup>	RF shielding	Reference	
UC Davis PSAPD + optical fibres, OBD, 7 T	17.5 µm copper foil, double layer	Wu et al. 2009	
University Tübingen APD, OBD, 7 T	10 μm copper foil, double layer	Judenhofer et al. 2007	
Brookhaven RatCAP/MR APD, IBD, 9.4 T	thin sheets of segmented copper	Maramraju et al. 2011	
University Tübingen APD, 7 T	9 μm copper foil, double sided, sliced	Wehrl et al. 2013	
University Seoul SiPM, OBD, 7 T	18 μm copper foil, dual layer	Yoon et al. 2012	
University Eulji SiPM, OBD, 3 T	$18\mu\mathrm{m}$ copper foil	Hong et al. 2012	
University Kobe SiPM, OBD, 0.15 T	copper foil	Yamamoto et al. 2012	
University Sogang SiPM, OBD, 3 T	gold plated fabric and mesh type aluminium	Hong et al. 2013	
FP7 Hyperimage, Hyperion I SiPM, IBD, 3 T	18 μm galvanic copper on silver paint, split areas	Weissler et al. 2014	
Siemens AG, Human brain insert APD, $3 T + 9.4 T$	$10\mu\mathrm{m}$ copper foil	Kolb et al. 2012	
Siemens AG, Biograph mMR APD, IBD, 3 T	copper elements	Delso et al. 2011	
UC Davis APD, OBD, 7 T	carbon fibre composites, two concentric tubes	Peng et al. 2014	
Philips, Hyperion II <sup>D</sup> digital SiPM, IBD, 3 T	carbon fibre composites, module boxes	Weissler et al. 2012a	

 $^1$  Kind of photodetector, off-bore-digitization (OBD) or in-bore-digitization (IBD), field strength of the MRI system used

approaches indicate that carbon fibre composites can provide a sufficient amount of RF shielding for PET/MRI systems while reducing eddy currents.

Previous studies are predominantly based on empirical approaches and investigate the shielding efficiency on a whole system level. A major drawback of whole system investigations is the large number of parameters that influence shielding efficiency. In particular the heterogeneous mix of PET and MRI technologies makes it difficult to compare the benefits of the respective solutions. Therefore, the results obtained do not reflect the bare material shielding properties, but the application of a specific system configuration. On the one hand this is reasonable, because finally the performance of the whole system is decisive, but on the other hand it hinders systematic understanding, optimization and comparison of shielding materials.

The previously mentioned shortcomings motivated the study presented here, in particular, the question: how good is the shielding efficiency of carbon fibre composites and can carbon fibre composites outperform conventional shielding materials for PET/MRI? The approach here is to investigate the shielding efficiency and eddy current properties of carbon fibre composites independently of a specific PET/MRI system. Nevertheless, this work has a direct practical relevance, as the presented carbon fibre composite shielding is implemented in the Hyperion II<sup>D</sup> PET/MRI system.

In contrast to a pure and homogeneous material like copper, carbon fibre composites are comprised of a plurality of material compositions and related fabrication techniques. Thus, the following section describes the specific kind of carbon fibre composite and fabrication technique used. After that, shielding theory and PET/MRI specific restrictions are discussed, followed by experimental investigations. Based on this, a model to calculate the shielding efficiency of the used carbon fibre composites is developed and used to compare shielding efficiency and eddy current effects quantitatively.

# 4.2 Fabrication of carbon fibre RF enclosures

Carbon fibre composites represent a very diverse class of composite materials. They all contain carbon fibres embedded in a matrix, but as well as the variety of applications, there exists a wide variety of fibre types, matrix materials and manufacturing processes. This section describes the materials and fabrication process of the carbon fibre composites used for the Hyperion II<sup>D</sup> PET/MRI system.

#### 4.2.1 Material selection

The RF shielding of the Hyperion II<sup>D</sup> system are made of multiple layers of biaxial, plain woven carbon fibre fabrics embedded in an epoxy matrix.

Single carbon fibre filaments have a diameter of  $5 \,\mu\text{m}$  to  $7 \,\mu\text{m}$  and are not directly suitable for weaving. Thus, usually several thousand carbon fibre filaments are bundled

	Tenax HTA-40 E13	Epoxy	Copper
Electrical conductivity	$62.5\times 10^3{\rm Sm^{-1}}$		$58\times10^6\mathrm{Sm^{-1}}$
Density	$1.77{ m gcm^{-3}}$	$1.1\mathrm{gcm^{-3}}$	$8.92\mathrm{gcm^{-3}}$
Filament diameter	$7\mu{ m m}$		_

**Table 4.2** Selected material properties of carbon fibres, epoxy matrix and copper. The TenaxHTA-40 E13 fibre was used for the fabrication of the laminates used in this study.

into a so-called roving, which is then used for weaving. Woven fabrics have the advantage of being manually well processable, thus minimising tooling investments. The kind of carbon fibre used, the number of fibres contained in the roving and the amount of fibres used per area unit are the key properties of these fabrics.

There is a very wide range of woven carbon fibre fabrics available on the market. For material selection, it was important that the electrical properties of the fibres were known and that the weaving structure was fine enough to produce laminates with smooth surfaces, i.e. height variations of the thickness because of the weaving structure should be minimized. The other selection criteria for the Hyperion II<sup>D</sup> system were primarily pragmatic, meaning the material should have good availability and be reasonably priced. Finally, the choice fell on a biaxial, plain woven fabric made of Tenax HTA-40 E13 with 3000 filaments per roving and a mass of 160 g m<sup>-2</sup>.

The epoxy resin and hardener was a type L epoxy from R&G Faserverbundwerkstoffe GmbH, Germany, a standard kind of epoxy for hand lamination, easy to apply and curable at room temperature. To improve the light-tightness of the composite, 5 % black colourant was added to the otherwise transparent epoxy mixture. The epoxy is electrical non-conductive.

An overview of selected material properties is given in table 4.2.

#### 4.2.2 The lamination process

The carbon fibre housings were fabricated using a hand lay-up with a vacuum bagging process. This process uses vacuum pressure to compress the wet laminate and to drain off excessive resin. It thus allows the fabrication of high-grade laminates with high and reproducible fibre volume ratios. The main advantage of this process is its flexibility with respect to the choice of materials and its low tooling investments. In the following, the most important fabrication steps are presented.

An anodized aluminium mandrel as shown in figure 4.1(a) gives the form of the housing. The cross section of the mandrel should be concave and constant over the entire length of the mandrel to ensure proper lamination and release of the laminate later on. To prevent sticking, the mandrel is treated with a release agent and polished before each lamination.

Before starting the lamination process, all required carbon fibre fabrics and auxiliary materials are cut into dimensions and prepositioned, as shown in figure 4.1(b). Following this step, the epoxy is mixed.

The lamination process itself starts by impregnating the carbon fabric gradually with the epoxy mixture, laying it up on the mandrel and slightly pressing it down, as shown in figure 4.1(c). Simultaneously, the mandrel is stepwise rotated to achieve the desired number of layers. The fabric should be well saturated with the epoxy mixture to avoid pinholes. Excessive epoxy will get drained off during the subsequent vacuum bagging process.

After finishing the lay-up, the wet laminate is covered with a separation and a bleeding layer, figure 4.1(d). The separation layer is a perforated, self-releasing polyethylene film. It prevents the bleeding layer sticking to the laminate, but it allows the resin to pass through. The bleeding layer itself is a synthetic fleece and fulfils two purposes: on the one hand it absorbs the excessive epoxy mixture, on the other hand it supports air flow while building up the vacuum.

Subsequently, the wet laminate is placed in the vacuum bag. The vacuum bag is an air-tight sealed polyethylene film bag (figure 4.1(e)), connected to a vacuum pump. The pump evacuates the air out of the bag and builds up a vacuum of approximately 0.7 bar, which compresses the laminate evenly and from all sides. During vacuum pressing, excessive resin gets drained out of the laminate into the bleeding layer.

The laminate cures within the vacuum bag. Depending on the resin, hardener and temperature, curing takes about 6 h to 24 h. Subsequently, the laminate is tempered in an oven at about 80 °C. The heat treatment fulfils multiple purposes: It completes the curing of the epoxy resin and thus improves the mechanical stiffness and thermal stability, but furthermore it simplifies the release of the laminate from the mandrel. Aluminium has a positive temperature coefficient, whereas carbon fibre has a negative one. Thus, during the heat treatment the aluminium mandrel expands and the composite shrinks, whereas during cooling down the mandrel shrinks and the composite expands. This simplifies the release of the composite from the mandrel. If the tempering is done properly, the laminate can be easily released from the mandrel after cooling down, as shown in figure 4.1(f).

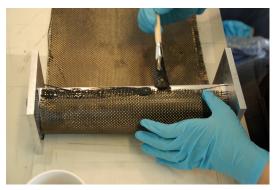
The process described is very versatile and allows the fabrication of a variety of different laminates. The number of layers, kind of fabric and matrix material can be easily adjusted, including the incorporation of other materials, e.g. additional metal layers. Furthermore, the process can be adapted to use fibre winding techniques instead of using hand lay-up, which allows the direct processing of fibre rovings and a more automated fabrication. Figure 4.2 presents some example laminates that were fabricated during the project.



(a) Aluminium mandrel



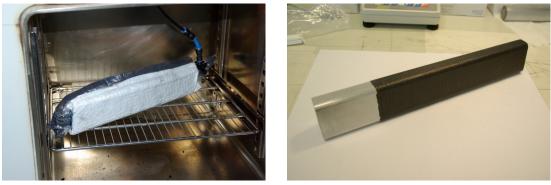
(b) Materials



(c) Hand lay-up



(d) Vacuum bagging preparation



(e) Vacuum bag in oven

(f) Release from mandrel

**Figure 4.1** Carbon fibre composite housing fabrication steps. (a) The shape of the housing is determined by an anodized aluminium mandrel. Before starting the lay-up, the mandrel is treated with a release agent. (b) The fabric and auxiliary materials are prepared. (c) Successively, the fabric is impregnated with the epoxy mixture and laid up on the mandrel. (d) Afterwards, the wet laminate is covered by a release and bleeding layer. (e) The laminate is cured within the vacuum bag and tempered in an oven. (f) Finally, the cured and tempered laminate can be slid off the mandrel.



**Figure 4.2** Overview of carbon fibre composite housings produced during the Hyperion II<sup>D</sup> development. Various mandrels target the specific geometric requirements of different housing approaches. In addition to pure carbon fibre fabrics, multiple laminates were fabricated with alternative materials, e.g. fibre glass, metal layers and coated fibres. Furthermore, the feasibility of carbon fibre winding was demonstrated.

# 4.3 Theoretical considerations of shielding efficiency and eddy currents

This section introduces the theoretical considerations of shielding efficiency and eddy currents. First, shielding efficiency is defined and the transmission theory of shielding is outlined, followed by a closer look at available design parameters and their impact on shielding efficiency. Thereafter, eddy currents and parameter dependences are discussed. The insights gained finally lead to a comparison of shielding efficiency versus eddy currents at given material parameters.

The theory presented here focuses on plain and homogeneous materials. At first glance, this may sound inconsistent, because fibre composites are of course non-homogeneous materials. However, as it will become apparent, it facilitates the analysis of experimental data and correlates materials properties to shielding efficiency and eddy currents. It explains if and how carbon fibre composites can outperform conventional copper shielding for PET/MRI.

## 4.3.1 Shielding efficiency

In general, the shielding efficiency SE of a shield is defined as the ratio of power received with and without the shield being present at constant incident power. It is usually expressed in decibels:

$$SE = 10 \log_{10} \left( \frac{P_{unshielded}}{P_{shielded}} \right)$$
(4.2)

Although shielding efficiency can be finally attributed to only two physical processes – reflection and absorption, their interaction and thus the obtainable shielding efficiency depends on numerous parameters. Those parameters are material parameters, e.g. electrical conductivity, but also geometric parameters, e.g. shape, structure and size of the shield, as well as the properties of the surrounding environment and the kind of incident wave. In consequence, shielding efficiency is not an independent material property, but is rather application specific. Furthermore, the application specific shielding efficiency can be easily influenced by unincorporated propagation paths, e.g. signal leakage at feedthroughs, which complicates the comparison of different shielding materials.

To facilitate analytical considerations and to allow direct comparisons, it is necessary to reduce the number of parameters and specify a standardized test environment. For this purpose, it is very convenient to investigate transverse electromagnetic (TEM) waves that incident perpendicularly on an infinite, planar shield of thickness d. In this case the unshielded wave corresponds to the incident wave, and the shielding efficiency can be expressed as

$$SE = 10 \log_{10} \left( \frac{P_{incident}}{P_{shielded}} \right).$$
 (4.3)

TEM waves are relevant in practice, because they approximate the radiation pattern in the far-field and near field properties can be derived from it. Furthermore, the propagation and shielding of TEM waves is at least in linear, isotropic and homogeneous media analytically well understood and established. Based on the common transmission line theory, the following section introduce the transmission theory of shielding to calculate and analyse the shielding efficiency of such shields.

## 4.3.2 Transmission theory of shielding

The transmission theory of shielding makes use of transmission line theory to describe the TEM shielding efficiency of infinite, planar shields. Referring to Schelkunoff (1943) and Schulz et al. (1988), this section outlines the fundamentals of the transmission theory of shielding, required to calculate the shielding efficiency of homogeneous and isotropic, planar shields. For illustration purpose, figure 4.3 summarizes the relevant processes.

TEM waves are characterized by the fact that their electric and magnetic field vectors are perpendicular to each other and to the direction of propagation. The ratio of the electric field E and the magnetic field H is determined by the characteristic impedance Z of the transmission medium. Within a homogeneous transmission medium of permittivity  $\epsilon$ , permeability  $\mu$  and conductivity  $\sigma$ , the characteristic complex impedance at the angular frequency  $\omega = 2\pi f$  is calculated as

$$Z = \frac{E}{H} = \sqrt{\frac{j\omega\mu}{\sigma + j\omega\epsilon}}, \qquad (4.4)$$

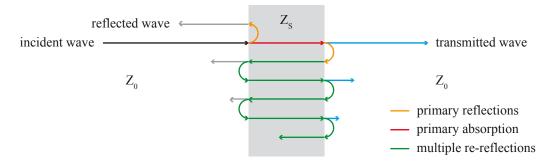


**Figure 4.3** Schematic of plane wave shielding. Part of the incident wave passes the shield and gets attenuated by absorption. The primary reflections at the entry and exit surface return part of the wave back. Whereas the wave at the entry surface is reflected back to infinity, the reflected wave at the exit surface is reflected back into the shield and is subject to multiple re-reflections at both surfaces. The overall shielding efficiency is defined as the total power ratio of the incident to transmitted power. Physically, the reflections appear at the surface and reflected and transmitted wave components overlap.

where  $j = \sqrt{-1}$  denotes the imaginary unit.

The propagation constant  $\gamma$  of a TEM wave within such a medium is defined as

$$\gamma = \alpha + j\beta = \sqrt{j\omega\mu(\sigma + j\omega\epsilon)}, \qquad (4.5)$$

where the real part of  $\gamma$  denotes the attenuation constant  $\alpha$  and the imaginary part the phase constant  $\beta$ . Thus, while travelling the distance d, the amplitude of the wave decays due to absorption to  $|e^{-\gamma d}|$ . For a single pass of the wave through the shield, this results in the absorption specific shielding efficiency

$$A = 20 \log_{10} \left| e^{\gamma d} \right|. \tag{4.6}$$

However, not the entire incident wave is able to enter and to exit the shield at all. If a TEM wave passes a planar boundary perpendicularly from a medium of impedance  $Z_1$  to a medium of impedance  $Z_2$ , part of the wave will be reflected. The corresponding reflection coefficient r and transmission coefficient t (both related to the electrical field component) are

$$r = \frac{Z_2 - Z_1}{Z_2 + Z_1}, \quad t = \frac{2Z_2}{Z_1 + Z_2}.$$
(4.7)

Considering the model of a planar shield of impedance  $Z_S$  surrounded by a medium of impedance  $Z_0$ , the incident wave passes two impedance boundaries, first when it enters the shield and second when it exits the shield. Both reflections are referred to as primary reflections. By straightforward multiplication, the combined transmission coefficient p of the primary reflections is

$$p = \frac{2Z_S}{Z_0 + Z_S} \cdot \frac{2Z_0}{Z_0 + Z_S} = \frac{4Z_0 Z_S}{(Z_0 + Z_S)^2} \,. \tag{4.8}$$

In consequence, only the fraction |p| of the incident wave passes both boundaries of the shield and the shielding efficiency related to primary reflections is

$$R(dB) = 20 \log_{10} \frac{1}{|p|} = 20 \log_{10} \left| \frac{(Z_0 + Z_S)^2}{4Z_0 Z_S} \right|.$$
 (4.9)

So far this model neglects the returning waves of the primary reflections. Whereas the reflected wave at the entry surface is reflected back to infinity, the reflected wave at the exit surface is reflected back into the shield and is subject to multiple re-reflections at both boundaries of the shield, as well as absorption while travelling through the shield forth and back. The full mathematical derivation requires an impedance transformation over a lossy transmission line to describe this behaviour. With reference to the full derivation by Schulz et al. 1988, the shielding efficiency because of multiple re-reflections can be described by an additional term

$$B(dB) = 20 \log_{10} \left| 1 - \frac{(Z_S - Z_0)^2}{(Z_S + Z_0)^2} e^{-2\gamma d} \right|.$$
(4.10)

The term B is often referred to as correction factor, as it corrects the straight forward primary shielding efficiency for multiple reflections. It should be noted, that B depends on both reflective and absorptive properties, and that B can be positive as well as negative, because the interference of primary and higher-order transmitted waves can be constructive or destructive. The factor two of the expression  $e^{-2\gamma d}$  can be attributed to the two times observed attenuation while travelling back and forth. In consequence, successive re-reflections can increase or decrease shielding efficiency. However, in many practical situations, if the primary absorption exceeds approximately 15 dB, the term B can be neglected, because the multiple reflected wave recedes quickly.

In summary, the plane wave shielding efficiency of a planar shield with impedance  $Z_S$ , propagation constant  $\gamma$  and thickness d, surrounded by a medium of impedance  $Z_0$ , calculates as

$$SE = A + R + B$$
  
=  $20 \log_{10} \left| e^{\gamma d} \right| + 20 \log_{10} \left| \frac{(Z_0 + Z_S)^2}{4Z_0 Z_S} \right| + 20 \log_{10} \left| 1 - \frac{(Z_S - Z_0)^2}{(Z_S + Z_0)^2} e^{-2\gamma d} \right|,$  (4.11)

whereby the impedances as well as the propagation constant are determined by the electrical conductivity, electrical permittivity and magnetic permeability of the medium.

## 4.3.3 Influence of material parameters

In many real-world applications RF shields are surrounded by air. As air is a very poor conductor with an electric and magnetic susceptibility close to zero, the impedance of air equals approximately the impedance of free space. Thus, in this case the impedance of the surrounding media can be approximated as

$$Z_0 \simeq \sqrt{\frac{\mu_0}{\epsilon_0}} \simeq 377 \,\Omega \,.$$
 (4.12)

By restricting the properties of the surrounding media, merely the properties of the shield and the frequency of the incident wave remain to influence shielding efficiency. As deduced in the previous section, the properties of the shield are determined by its conductivity, permeability, permittivity and thickness.

Taking into account the PET/MRI application-specific requirements, those parameters can be further restricted. As MRI systems require a very homogeneous main magnetic field, which can be easily distorted by changes in magnetic permeability, the susceptibility of materials used within the MRI bore should be close to zero. This limits the magnetic permeability of possible shielding material to

$$\mu \simeq \mu_0 \,. \tag{4.13}$$

Furthermore, shielding materials are assumed to be good electrical conductors. If  $\sigma \gg \omega \epsilon$ , the impedance and the propagation constant are dominated by electrical conductivity and the influence of the permittivity diminishes:

$$Z_{S} = \sqrt{\frac{j\omega\mu}{\sigma + j\omega\epsilon}}$$

$$\simeq \sqrt{\frac{j\omega\mu}{\sigma}}, \quad \sigma \gg \omega\epsilon$$
(4.14)

$$\gamma = \alpha + j\beta$$
  
=  $\sqrt{j\omega\mu(\sigma + j\omega\epsilon)}$   
 $\simeq \sqrt{j\omega\mu\sigma}, \quad \sigma \gg \omega\epsilon$  (4.15)

In consequence, conductivity determines absorption in a good conductor. However, conductivity also decreases the wavelength within the transmission medium. Applying the good conductor assumption on the propagation constant in equation 4.5, the wavelength in a good conductor calculates as

$$\lambda = \frac{2\pi}{\beta} = 2\pi \sqrt{\frac{2}{\omega\mu\sigma}} \,. \tag{4.16}$$

The wavelength in a good conductor is thus considerably lower than in free-space. Up to frequencies of 1 GHz, materials with a conductivity higher than  $1000 \,\mathrm{S}\,\mathrm{m}^{-1}$  and reasonable high susceptibility (below 100) can be expected to fulfil the good conductor approximation.

In many practical applications, the impact of multiple reflections can be neglected if absorptive shielding exceeds 15 dB, because the multiple times reflected wave inside the shield diminishes quickly (Schulz et al. 1988). This simplification separates absorptive and reflective shielding properties and is thus very useful to analyse them more independently. However, one has to be aware of the possibility of multiple reflections and they can affect shielding efficiency if absorption is low.

Combining all those assumptions, the equation for shielding efficiency simplifies to

$$SE_{simp} = A_{simp} + R_{simp}$$
  
=  $20 \log_{10} |e^{\gamma d}| + 20 \log_{10} \left| \frac{Z_0}{4Z_S} \right|$   
=  $20 \log_{10} \left| e^{\sqrt{j\omega\mu_0\sigma}d} \right| + 20 \log_{10} \left| \frac{\sqrt{\frac{\mu_0}{\epsilon_0}}}{4\sqrt{\frac{j\omega\mu_0}{\sigma}}} \right|$   
=  $\frac{20}{\log 10} \sqrt{\omega\mu_0\sigma}d + 10 \log_{10} \frac{\sigma}{16 \omega\epsilon_0}$ . (4.17)

Under the aforementioned conditions, the shielding efficiency at a given frequency solely depends upon the conductivity and thickness of the shield. From equation 4.17 follows, that the shielding efficiency related to primary absorption increases linear with the thickness and the square root of conductivity, whereas the shielding efficiency because of primary reflections increases only logarithmically with conductivity. Thus, a decrease in conductivity can be compensated by an increase in thickness.

In order to determine a beneficial trade-off for PET/MRI, the impact of conductivity and thickness on eddy currents must be considered.

## 4.3.4 Eddy currents

Eddy currents are circular currents induced by time varying magnetic fields into conductive materials. During gradient switching, MRI systems are a major source of timevarying magnetic fields. In contrast to the MRI RF system, the frequency range of the MRI gradients is significantly lower, merely in the kilohertz range. Thus, most eddy current effects caused by MRI gradient systems can be considered as quasi-stationary electromagnetic processes.

A basic model to illustrate the induction of eddy currents is shown in figure 4.4. An arbitrary shaped conductive loop with the electrical resistance R and self-inductance L encloses the magnetic flux  $\Phi$ . According to Faraday's law of induction, a change of the magnetic flux  $\Phi$  induces the circular voltage

$$U_{ind} = -\frac{\partial \Phi}{\partial t} \tag{4.18}$$

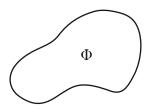


Figure 4.4 Basic model of induction. An arbitrary shaped conductive loop encloses the magnetic flux  $\Phi$ . According to Faraday's law of induction, a change in magnetic flux induces a voltage into the loop that causes a current to flow. This so called eddy current results in a reverse oriented magnetic field, counteracting the change in magnetic flux. The amplitude, rise and decay of the eddy current is determined by the resistance R and inductance L of the loop.

into the loop. Neglecting the self-inductance of the loop, this would immediately result in the eddy current

$$I_{eddy} = -\frac{1}{R} \frac{\partial \Phi}{\partial t} , \qquad (4.19)$$

which in turn causes a reverse magnetic field, counteracting the original gradient field. However, because of the self-inductance of the loop, this value can only be reached asymptotically. The actual response is modelled by an RL series circuit, composed of the resistance and self-inductance of the loop, and is characterized by the time constant

$$\tau = \frac{L}{R}.$$
(4.20)

The RL series circuit acts as low-pass filter with the time-constant  $\tau$ . In the case of pulsed gradients, this leads to an exponential rise and decay of eddy currents. Both, the amplitude and the time constant are relevant to reduce the influence of eddy currents on MRI, because the time integral of gradient field distortion determines the resulting phase error of the MRI signal. In consequence, the self-inductance and conductivity of loop structures are the key design parameters to minimize eddy currents and related imaging distortions.

Whereas the electrical resistance is determined by the geometry and conductivity of the loop, the inductance solely depends on the geometry of the loop. In consequence, at a given geometry, eddy currents can only be reduced by decreasing the conductivity of the material. Thereby, decreasing the conductivity has a twofold impact on eddy currents: it linearly reduces the amplitude as well as the time constant of eddy currents. Resulting eddy currents are thus not only weaker in amplitude, but also decay faster.

The single loop model can now be transferred to planar shields. Under the assumption that a shielding is electrical thin to MRI gradients, the skin effects is negligible and the shield can be considered as an infinite thin plane with the sheet conductance

$$\sigma_{sq} = \sigma \cdot d \,. \tag{4.21}$$

Such a shield can be modelled as a sum of infinite conductive loops located in the plane of the shield. The resistance and time constant of each loop l depends on the bulk material conductivity  $\sigma$  and the thickness d of the shield:

$$R_l \propto \frac{1}{d \cdot \sigma} = \frac{1}{\sigma_{sq}} \tag{4.22}$$

$$\tau_l = \frac{L_l}{R_l} \propto d \cdot \sigma = \sigma_{sq} \tag{4.23}$$

Analogous to the single loop model, the effect is twofold, as decreasing conductivity or thickness reduces the amplitude and time constant of the eddy currents at the same time. The integral effect of all loops and respective eddy currents within the shield determine the overall observed field distortions. As all loops are assumed to lie in the plane of the shield, the integral effect solely depends on the bulk material conductivity and the thickness of the shield.

In summary, the amplitude and time constant of eddy currents are both proportional to the product of conductivity and thickness of the shield, rather known as sheet conductance. Sheet conductance thus is the key design parameter to control eddy currents and related effects.

As sheet conductance is a well defined, easy to calculate and measurable property, it is very convenient to use sheet conductance as measure of eddy currents, knowing full well that the dependency of related effects on MRI are stronger than linear in many applications. The following section will use sheet conductance as measure of eddy currents to correlate shielding efficiency and eddy currents.

## 4.3.5 Shielding efficiency versus eddy currents

As shown in the previous section, RF shielding efficiency and eddy currents are both determined by the conductivity and thickness of the shield. The design goal thus is to maximise shielding efficiency and minimize sheet conductance by adjusting conductivity and thickness of the shield.

Table 4.3 summarises the functional relationship of shielding efficiency and sheet conductance related to bulk material conductivity, thickness and frequency. As absorptive shielding is more strongly influenced by thickness than conductivity, a decrease in conductivity can be compensated for by an increase in thickness.

Based on equation 4.11, figure 4.5 shows the calculated shielding efficiency versus sheet conductance for copper and two hypothetical carbon materials for reasonable sheet thicknesses at three typical MRI frequencies. From this figure it becomes clear, that thicker but lower conductive materials are beneficial for PET/MRI, because they result in higher shielding efficiency at lower sheet conductance and hence reduce eddy current related effects. The advantage increases with frequency, as absorptive shielding

	$\operatorname{conductivity}$	thickness	frequency
absorptive shielding (dB)	$\sqrt{\sigma}$	d	$\sqrt{\omega}$
reflective shielding (dB)	$\log \sigma$		$-\log \omega$
sheet conductance	$\sigma$	d	

Table 4.3Functional relationship of shielding efficiency and sheet conductance versus bulkelectrical conductivity, thickness and frequency, based on equation 4.17 and 4.21.

increases by the order of  $\sqrt{\omega}$  whereas reflective shielding decreases only by the order of  $\log \omega$ .

Yet, all consideration so far are based on the assumption of homogeneous planar shields. Carbon fibre composites are of course non-homogeneous material compositions. Thus, such a simple theoretical description is not necessarily suitable to model the actual shielding efficiency of carbon fibre composites.

The next section will thus focus on the experimental verification of the shielding efficiency of carbon fibre composites, and evaluate to what extent the theoretical advantage of lower conductivity materials for PET/MRI can be realized. Thereby, the theoretical foundation of the different shielding processes and their parameter dependencies will be utilized to analyse measurement data.

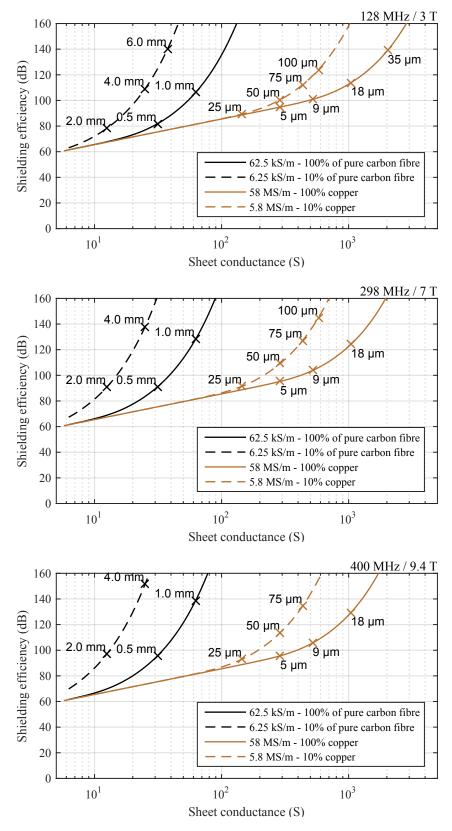


Figure 4.5 Calculated shielding efficiency of copper and two hypothetical materials with 10 % and 100 % of the conductivity of pure carbon fibre versus sheet conductance at the common MRI frequencies 128 MHz / 3 T (top), 298 MHz / 7 T (middle) and 400 MHz / 9.4 T (bottom). Lower conductive but thicker materials show higher shielding efficiency at lower sheet conductance, which makes them interesting for PET/MRI RF shielding to reduce eddy current related distortions.

## 4.4 Experimental verification

As explained in section 4.3.1, shielding efficiency in general is determined by numerous parameters, including material parameters, but also application specific properties as well as geometry. The consideration of TEM waves and planar infinite shields surrounded by air reduced the number of parameters to properties of the shield only and simplified analytical calculations. The following work has the objective to investigate the fundamental advantage of carbon fibre composites for PET/MRI RF shielding, independent of a specific PET/MRI system, and evaluate to what extent carbon fibre composites match the theoretical predictions. Therefore, the following experimental investigation are focused on the TEM shielding efficiency of planar shields rather than a specific shielding configuration for a PET/MRI system. However, this requires an experimental set-up that reflects the previously made assumptions.

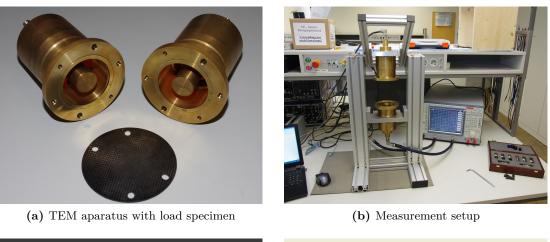
## 4.4.1 Quantification of shielding efficiency in the MRI frequency range

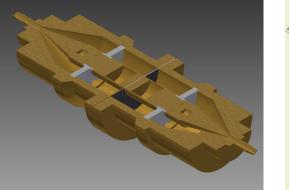
The main frequency range of interest for PET/MRI depends on the field strength of the MRI and the nucleus being imaged. As the gyromagnetic ratio of hydrogen is  $42.58 \text{ MHz T}^{-1}$  and most nowadays human size MRI systems operate at 1.5 T to 9.4 T, the main frequency range of interest for PET/MRI is approximately in the range of 50 MHz to 500 MHz. Thus, the corresponding free-field wave lengths range from 0.6 mto 6 m. This puts several challenges to characterize the shielding efficiency in the MRI frequency range. Straight forward approaches, e.g. using two antennas and installing a shield in-between, require measurement arrangements and samples sizes in the order of the wavelength. Furthermore, appropriate antennas covering the frequency range of interest as well as environmental interference and the dynamic range of the test equipment represent further challenges, which makes it very cumbersome to apply such approaches in the MRI frequency range.

A convenient method to overcome this problem is the use of TEM cells. The idea of a TEM cell is to insert a test sample into a wave guide, where transverse electromagnetic fields can be achieved within small dimensions. One of such a test method is specified by the ASTM D4935-10 (2010) standard.

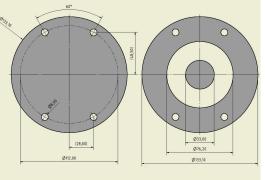
### TEM test cell according to ASTM D4935-10

The ASTM D4935-10 standard specifies a test apparatus and procedure to measure the shielding efficiency of planar materials for plane transverse electromagnetic waves. Its main component are two brass flanges as shown in figure 4.6, forming a coaxial transmission line. Both flanges are screwed together and clamp a test specimen inbetween. The device is connected to an RF transmitter and receiver, e.g. a network analyzer, and thus measures the insertion loss caused by the test specimen.





(c) CAD half section of TEM cell



(d) Load and reference specimen

Figure 4.6 ASTM 4935-10 TEM cell test equipment used to perform the shielding efficiency measurements. (a) Both flanges are screwed together with plastic screws to clamp the test specimen in-between. The flanges are made of brass and together they weigh more than 13 kg. (b) To ease handling they were thus mounted in a mechanical support. (c) CAD half section of the TEM cell. At the sample side, the outer diameter of the inner conductor is 33.1 mm and the inner diameter of the outer conductor is 87.8 mm. (d) Dimensions of the load and reference specimen.

Each flange is approximately 190 mm long and composed of an inner and outer conductor, forming a coaxial transmission line. The ratio of the inner and outer diameter is matched to result in a constant line impedance of  $50 \Omega$  over the entire length of each flange, whereby the diameter of the inner and outer conductor varies over the length of the flange. On the connector side it fits an N-connector and on the sample side the outer diameter of the inner conductor is 33.1 mm and the inner diameter of the outer conductor is 87.8 mm, to achieve an appropriate sample size.

Each measurement requires a reference and a load specimen, as shown in figure 4.6 (d). The reference and the load specimen shall be of the same material and thickness. In particular the thickness of the specimen is crucial, as it influences the capacitive coupling and displacement current between the two flanges. The ASTM 4935-10 standard specifies, that the difference in average thickness shall be less than 25  $\mu$ m and the variation within and between specimens less than 5%. The shielding efficiency is calculated as the difference between the reference and the load measurement.

Because of the dimensions of the test cell, the ASTM 4935-10 test method is valid within the frequency range of 30 MHz to 1500 MHz. The lower bound originates from the capacitive coupling between both flanges, which causes a decreasing displacement current at decreasing frequencies and thus weaker coupling. The upper bound is to prevent the propagation of higher modes and is determined by the maximum diameter of the coaxial structure of the flanges. Both limits are not exact, e.g. the capacitive coupling also depends on the thickness of the sample. The frequency range of the ASTM 4935-10 standard covers the frequency range of interest for PET/MRI and was thus chosen as measurement method.

## 4.4.2 Materials and methods

### Preparation of test specimen

Test specimen were produced using the same woven carbon fabric, epoxy and vacuum bagging method as described in section 4.2, but instead of laminating the composites on a mandrel, flat sheets of carbon fibre composites were laminated on planar plates. From the cured laminates, the reference and load patterns were cut out with a CNC milling machine.

A series of eight samples with one to eight layers of carbon fibre fabric were produced. The weaving pattern of all layers were equally aligned. In addition, a 1 mm copper specimen was used to determine the dynamic range of the measurement set-up.

#### Measurement of shielding efficiency

Measurements presented in this work were performed with an ASTM 4935-10 TEM cell and a Rohde & Schwarz ZVRE 1127.8551.51 network analyzer. The TEM cell used differs slightly from the original ASTM 4935-10 specifications, as it was build with metric instead of imperial threads and the surfaces of the flanges are uncoated. Furthermore, commercial off-the-shelf N-connectors were used instead cutting N-connector threads on the device itself and some outer dimensions varied, but the dimensions of the coaxial structure itself were preserved. Both flanges and the test specimen were screwed together with four plastic screws. All screws were gradually tightened with approximately 1.5 Nm plus a quarter turn.

The frequency range of the network analyzer was set to 10 MHz to 1000 MHz with 1601 points per measurement, using a linear sweep. The receiver bandwidth was set to 100 Hz. A full two port calibration was performed, with the reference plane at the N-connectors of the flanges.

#### Measurement of sheet conductance

Sheet conductance was measured inductively with non-contact resistivity measurement systems (Kitec M-RES 2000 and Suragus EddyCus TF lab2020)<sup>1</sup>. The measurement principle is based on inducing eddy currents into the test specimen and measuring the resulting magnetic field. Because of the eddy currents, the resulting field depends on the sheet conductance of the test specimen, as described in the analysis above.

The advantage of this method is that no electrical contact with the specimen is required. Making reliable and repeatable electrical contact with carbon fibre composites is difficult, because the epoxy matrix is non-conductive. Moreover, the inductive measurement method emulates the intended design case in an MRI system.

#### Measurement of specimen thickness

The specimen thickness was measured in two different ways. First, specimen thickness was measured directly with a calliper. However, a direct measurement of specimen thickness with a calliper is error prone, because in case of surface irregularities it is upward biased towards the maximum thickness of the specimen. Thus, specimen thickness was additionally calculated based on measuring the mass per unit area and the specified density of carbon fibre and epoxy.

## 4.4.3 Results

#### **Mechanical properties**

Table 4.4 summarizes the properties of the produced carbon fibre composites. The average calculated thickness of each layer is 0.15 mm. Visual and tactile inspection of the specimen reveal surface imperfections, in particular on the surfaces facing the release

<sup>&</sup>lt;sup>1</sup>Two different measurement systems were used because of limited access to the systems. The one, three and five layer specimens were measured with the Kitec M-RES 2000 and the two and four layer specimen were measured with the Suragus EddyCus TF lab2020.

film and the bleeding layer during vacuum bagging. Those surfaces are patterned with the structure of the carbon fibre fabric and the release film. Furthermore, specimens thinner than 3 layers show air gaps in the composite structure. In line with this, the specimen thickness measured with a calliper, as shown in figure 4.7, exceeds the calculated thickness on average by 0.18 mm. With respect to planarity, the test specimens miss the strict ASTM 4935-10 specifications. This might cause measurement errors. The appendix X1.3 of the ASTM 4935-10 specifications mentions that in particular rough surfaces can cause random and hard to reproduce errors. The evaluation of the results should therefore be given appropriate care.

The calculated fibre volume ratio of the composites is on average 61%. Thinner specimens tend to have slightly higher fibre volume fractions than thicker ones, which may be attributed to the fact that thicker layer structures impede the extraction of excess resin during vacuum bagging. The high fibre volume ratio of the single layer specimen is caused by numerous air gaps in the composite structure.

## Sheet conductance

As shown in figure 4.7, the measured sheet conductance increases linearly with the number of layers and is on average 2.333 S per layer. Because of mechanical restrictions (the samples were too thick to fit into the measurement device) and the skin effect, measurements could only be performed for specimens up to five layers thick. Based on the computed thickness, the average material conductivity calculates as  $16181 \,\mathrm{S\,m^{-1}}$ , which is about 25 % of the bulk conductivity of pure carbon fibre and about 3000 times lower than that of copper.

This result fits well within the predicted conductivity range of 10 % to 100 % of the raw conductivity of carbon fibres  $(6.25 \text{ kS m}^{-1} \text{ to } 62.5 \text{ kS m}^{-1})$ , as used in figure 4.5. It also indicates that the carbon fibre composites used fulfil the good conductor approximation within the MRI frequency range, i.e. the conductivity of the carbon fibre composites of  $16181 \text{ S m}^{-1}$  is clearly higher than the required value of  $1000 \text{ S m}^{-1}$  as calculated in section 4.3.3. However, it should be noted, that the calculated conductivity is a purely hypothetical value, as in general the conductivity of fibre composites is neither isotropic nor homogeneous.

## Shielding efficiency

Figure 4.8 summarizes the measured shielding efficiency of the test specimen. The shielding efficiency of the 1 mm copper disk indicates the dynamic range of the measurement set-up to be about 120 dB. The measured shielding efficiency of the carbon fibre composites ranges from 49 dB to the dynamic limit. As expected, shielding efficiency increases with the number of layers and tends to increase with frequency.

<b>Table 4.4</b> Measured properties of carbon fibre composite specimen: number or layers $n$ ,
calculated thickness $\tilde{d}$ , mass per unit area $m_A$ , fibre volume ratio $V_f$ , sheet conductance $\sigma_{sq}$ ,
sheet conductance per layer $\sigma_{sq}/n$ and calculated conductivity $\tilde{\sigma}$ .

	n	$\tilde{d} \ (\mathrm{mm})$	$\frac{\tilde{d}}{n}$ (mm)	$m_A \left(\frac{\mathrm{g}}{\mathrm{m}^2}\right)$	$V_f$ (%)	$\sigma_{sq}$ (S)	$\frac{\sigma_{sq}}{n}$ (S)	$\tilde{\sigma} \left(\frac{S}{m}\right)$
L1	1	0.14	0.14	222	67	2.317	2.317	17069
L2	2	0.29	0.29	433	62	4.790	2.395	16445
L3	3	0.45	0.15	666	61	6.954	2.318	15580
L4	4	0.58	0.15	900	62	9.468	2.367	16191
L5	5	0.73	0.15	1111	62	11.351	2.270	15619
L6	6	0.93	0.16	1391	58			
L7	7	1.09	0.16	1637	58			
L8	8	1.23	0.15	1847	59			
Ø		—	0.15		61		2.333	16 181

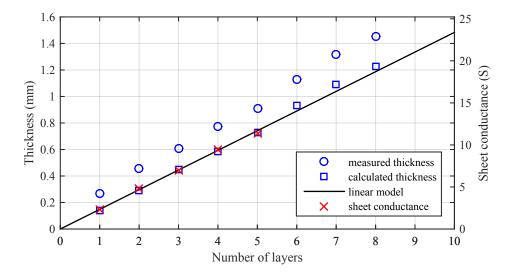


**Figure 4.7** Specimen thickness and sheet conductance versus number of layers. Surface imperfections bias the calliper-measured thickness towards the maximum specimen thickness. The calculated thickness is deduced from the mass per unit area and specific density of carbon fibre and epoxy. The amount of carbon fibre is known by the number layers and the mass per unit area of the fabric. Because of the systematic bias of the measurement, favour was given to the calculated value to deduce the conductivity of the composite. However, because of the inhomogeneous and anisotropic nature of carbon fibre composites, conductivity remains a hypothetical value. If possible, it is thus more convenient to relate to the number of layers.

Striking, however, are the peaks and following decrease in measured shielding efficiency for samples with six and more layers above approximately 85 dB and the slight dip of the five layer specimen near 500 MHz. This behaviour contradicts the expected physical behaviour.

The measurements have been repeated several times and various attempts have been made to eliminate the measurement artefacts, e.g. improving the sample planarity by grinding, replacing measurement cables, cleaning contact surfaces and connectors, as well as adjusting the torque of the connection screws. None of them could eliminate the observed anomalies.

Thus, the observed anomalies are considered to be an artefact of the measurement set-up, e.g. caused by resonance or propagation of higher modes within the TEM cell or the specimen. The excitation of higher modes and surface imperfections are known to cause measurement artefact (Badic and Marinescu 2002, Catrysse et al. 1992). Observed artefacts might be stimulated by impedance discontinuities. For example, the length of the flanges of 190 mm corresponds approximately to one-quarter wavelength (214 mm at 350 MHz) of the first peak, whereby the effective length of the flange can be expected to be slightly longer because of the widening of the coaxial structure and the N-connector. But also the specimen itself might impact those artefacts. Surface imperfections might cause inhomogeneous coupling to the test apparatus. Furthermore, the wavelength in the carbon fibre composites is expected to be considerable lower than in free-space. Using equation 4.16 and assuming a homogeneous and isotropic conductivity of 15000 S, the wavelength at 350 MHz is only 1.38 mm. This is in the order of the specimen thickness and thus might promote the excitation of higher modes.

The observed artefacts limit the measurement range significantly and prohibit reliable measurements with more than approx. 85 dB of shielding. In consequence, a direct experimental comparison of carbon fibre composites to typical copper foil thickness is hampered. To overcome this, the following section focuses on modelling the shielding efficiency of the carbon fibre composites using the valid data range.

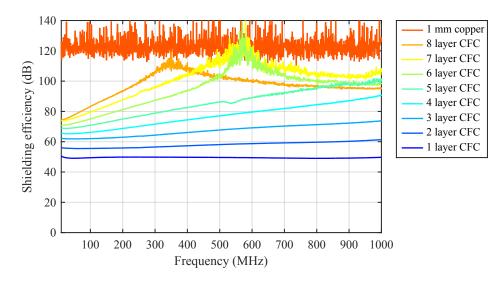


**Figure 4.8** Measured shielding efficiency of carbon fibre samples and 1 mm copper specimen. The copper specimen indicates the dynamic range of the measurement set-up to be about 120 dB. The shielding efficiency of the carbon fibre composites tends to increase with frequency as expected. Striking, however is that measurement data above 85 dB is affected by peaks and dips, which can not be explained by the shielding theory.

## 4.5 Analysis and modelling

Based on the transmission theory of shielding, measurement results shall be analysed and compared to model predictions. It ultimately aims to model the TEM shielding efficiency of carbon fibre composites with any number of layers within the MRI frequency range.

## 4.5.1 Analysis range

As stated in the previous section, the applicable dynamic range of the measurement set-up is limited to about 85 dB. In principle, data above 85 dB might be valuable to investigate the source of measurement artefacts in more detail. However, this would also require an appropriate model of the artefacts, including the test apparatus, sample imperfections and higher modes. Thus, further analysis includes only measurement results below 85 dB.

In addition, multiple reflections shall be neglected to simplify analysis. However, multiple reflection are not directly observable and thus have to be estimated a priori. As argued in section 4.3.2, the influence of multiple reflections usually can be neglected if absorption exceeds 15 dB. Assuming that carbon fibre composites can be reasonably well approximated as a homogeneous medium, absorption can be estimated based on equation 4.17. Using an average calculated thickness of 0.15 mm per layer and a downward estimated conductivity of 15 000 S, the 15 dB multiple reflection limit was calculated. The respective limits are summarized in table 4.5.

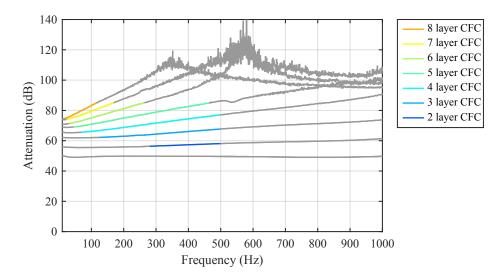


Figure 4.9 Coloured marked analysis range used for further calculations. The single layer sample is entirely excluded because of too low expected attenuation. Thinner samples are mainly limited by the attenuation limit, whereas thicker samples are limited by the empirical 85 dB limit to exclude region with unpredicted peaks and dips.

**Table 4.5** Frequency limit used to analyse measurement data. As the simplified model of shielding efficiency neglects multiple reflections, data which is expected to be affected by multiple reflections is excluded. This results in a lower frequency limit. Because of the observed peaks and dips, data above 85 dB is excluded and causes and upper frequency limit. Furthermore, analysis is limited to the MRI frequency range 50 MHz to 500 MHz.

	L1	L2	L3	L4	L5	L6	L7	L8
85 dB attenuation limit (MHz)				819	463	265	169	116
multiple reflection limit (MHz)	1119	280	124	70	45	31	23	17

Furthermore, the frequency range shall be limited to the MRI frequency range, namely 50 MHz to 500 MHz. In combination, those restrictions limit the analysis range as shown in figure 4.9. The single layer specimen is entirely excluded, because of too low attenuation, whereas the range of the thinner samples is limited by the attenuation limit and the range of the thicker samples is mainly limited by the dynamic range of the measurement set-up.

## 4.5.2 Modelling

It must be taken into account, that the theoretical considerations in section 4.3 are based on homogeneous and isotropic transmission media, whereas carbon fibre composites are in general inhomogeneous and anisotropic. Thus, the theoretical considerations and its parameters must be applied with caution. In particular, the conductivity of fibre composites is poorly defined and the significant composite thickness is troublesome to specify and measure. Therefore, it is preferable to substitute conductivity and thickness by a better quantifiable parameter. In contrast to conductivity and thickness, the number of carbon fibre layers is precisely specified. The number of layers determines the specimen thickness and the amount of conductive material. For modelling, the number of layers is thus preferred over conductivity and thickness.

In the following, the measurement data is analysed to extract the functional relationship of shielding efficiency and the number of layers. Therefore, it is convenient to separate absorptive and reflective shielding.

#### Absorptive shielding

Following the simplified shielding model of equation 4.17, absorption increases proportionally with the specimen thickness, whereas reflective shielding is independent of it. Thus, at a given frequency, overall shielding efficiency is expected to increase linearly with the number of layers.

Figure 4.10 shows the increase of measured shielding efficiency versus the number of layers at distinct frequencies within the MRI frequency range, including a linear regression for each frequency. It confirms, that the measured shielding efficiency increases linearly with the number of layers, wherein the individual slopes correspond to the absorption per layer at the respective frequency. Furthermore, the measured slope and thus the absorption per layer increases with frequency.

According to equation 4.17, absorption increases with the square root of frequency. Exactly this functional relationship is shown in figure 4.11, plotting the attenuation per layer versus the square root of frequency.

Following from this, the absorption of the *n*-layer carbon fibre composites at frequency f calculates as

$$A(n,f) = n \cdot \sqrt{\frac{f}{100 \,\mathrm{MHz}}} \cdot 4.2555 \,\mathrm{dB} \,.$$
 (4.24)

## **Reflective shielding**

The simplified shielding model excludes multiple reflections and thus shielding efficiency is determined by the absorptive term A and reflective term R only. In consequence, the difference between measured shielding efficiency and modelled absorption is expected to equal the amount of reflective shielding.

According to equation 4.17, reflective shielding is independent of the specimen thickness and is expected to decrease logarithmically with frequency. Figure 4.12, showing the residual shielding efficiency versus frequency for each specimen, confirms this assumption. Hence, the functional relationship of reflective shielding versus frequency calculates as

$$R(f) = 49.43 - 15.13 \log_{10} \frac{f}{100 \,\mathrm{MHz}} \,. \tag{4.25}$$

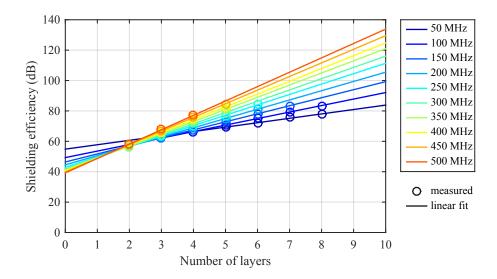
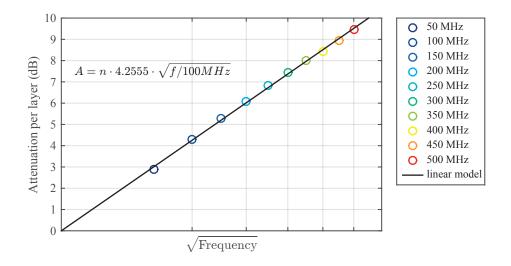
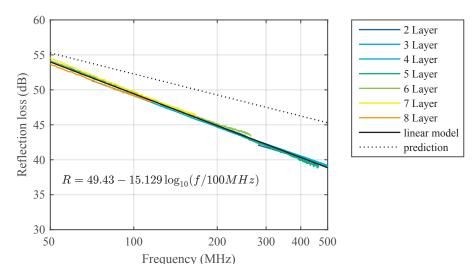


Figure 4.10 Shielding efficiency versus the number of layers at selected frequencies within the analysis range. Data shown is based on the measurement data of figure 4.9. At constant frequency, the shielding efficiency increases linearly with the number of layers. This matches the predicted behaviour of the simplified shielding equation for homogeneous conductors. The slope of each line corresponds to the shielding efficiency per layer and increases with frequency. The y-intercepts at n = 0 indicate the amount of reflective shielding. As predicted by theory, the amount of reflective shielding decreases with frequency.



**Figure 4.11** The measured shielding efficiency per layer versus frequency is proportional to the square root of frequency, as predicted by the simplified attenuation equation 4.17. The attenuation of carbon fibre composites per layer increases linearly with the number of layers and the square root of frequency.



**Figure 4.12** Residual reflection loss remaining after subtraction of modelled absorption loss from measured shielding efficiency. The shielding model predicts that the reflective loss is independent of the number of layers and decreases logarithmically with frequency. Both assumptions are met. However, the slope of the logarithmic decrease is steeper than predicted in the homogeneous model.

Remarkably, the slope of decrease is steeper than predicted by the shielding efficiency model of planar, homogeneous materials. This may be attributed to the fact, that the conductivity of fibre composites is neither isotropic nor homogeneous. Because of the woven structure, all carbon fibres are aligned almost parallel or orthogonal to each other. Thus, the effective conductivity of the specimen is likely to be a tensor with preferred directional conductivity correlated to the fibre alignment. In principle, also a systematic measurement error is possible. An explicit measurement of the reflectivity could clarify this.

## **Combined model**

In summary, the shielding efficiency of the carbon fibre composites calculates as:

$$SE(n,f) = A(n,f) + R(f)$$
  
=  $n \cdot 4.2555 \cdot \sqrt{\frac{f}{100 \text{ MHz}}} + 49.43 - 15.13 \log_{10} \frac{f}{100 \text{ MHz}}$  (4.26)

The model neglects multiple reflections. It should thus be only applied if attenuation exceeds 15 dB of attenuation, but the amount of absorption may be calculated using the model.

## 4.5.3 Comparison to measurement data

Figure 4.13 shows the measurement data superposed with the model calculations. It confirms, that the model reproduces the measurement data within the analysis range

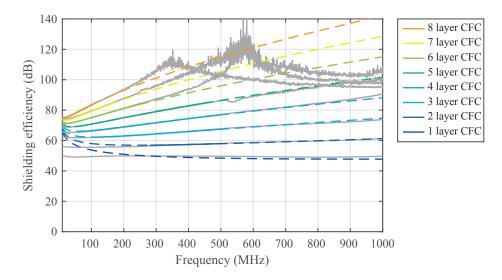


Figure 4.13 Comparison of measured and calculated shielding efficiency. Solid lines indicate data within the analysis range and dashed lines indicate data outside the analysis range. Coloured lines are model data, grey curves show measurement data.

very well. Even the single layer specimen, which was excluded from analysis, and the frequency range 500 MHz to 1000 MHz is well approximated.

The residual errors within the analysis range are summarized in figure 4.14. Within the analysis range, the model fits the measurement data within 0.8 dB, the standard deviation of the residual being 0.23 dB. The thinnest specimen within the analysis range, the two layer specimen, deviates clearly more at lower frequencies, thus indicating a remaining influence of multiple reflections. Thicker specimen, in particular the five and six layer specimens, tend to deviate more at higher frequencies, thus indicating that even measurement below 85 dB might be affected by measurement artefacts. However, the upper as well as the lower analysis limits are no hard limits and are based on estimates. Observed model deviations are thus expected.

The model deduced from measurements data neglects multiple reflections. In consequence, model predictions and measurement data deviate at frequencies below the analysis range. As a matter of fact, this effect is more pronounced for thinner specimen. However, the comparison confirms, that multiple reflections can be neglected if absorption exceeds 15 dB, which is the case for composites with more than four layers at frequencies above 50 MHz. Thus, no attempts were made to extend the model for multiple reflections.

## 4.5.4 Shielding efficiency versus sheet conductance

Based on the developed model, shielding efficiency can now be easily compared to sheet conductance, even beyond the limitations of the available measurement data. Respective results at three typical MRI frequencies (128 MHz, 298 MHz and 400 MHz are presented in figure 4.15.

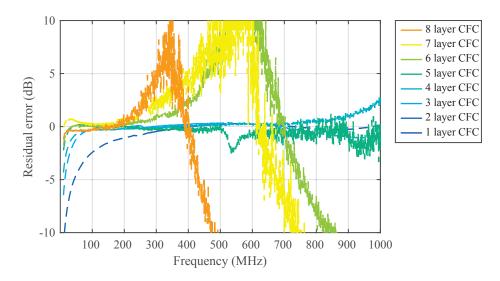


**Figure 4.14** Residual error between shielding model and measurement data. Within the analysis range, model predictions match measurement data better than 0.8 dB. At frequencies below the analysis range, the model deviates mainly because of multiple reflections, which are not included in the model. High attenuation data deviates, because of measurement artefacts.

The comparison proves that carbon fibre composites offer higher shielding efficiency at several times lower sheet conductance compared to copper. It thus confirms the theoretical predicted advantage of shielding materials with a lower specific conductivity for PET/MRI, at the cost of higher material thickness.

Furthermore, the comparison shows that the results match the range predicted in section 4.3.5. This is remarkable, as it implies that the shielding efficiency and sheet conductance of carbon fibre composites can be reasonably well approximated as homogeneous and isotropic transmission media.

The advantage of carbon fibre composites increases with frequency as the ratio of shielding efficiency to sheet conductance increases, but also because the required material thickness decreases with frequency. As shown in figure 4.16, the advantage of the ratio of shielding efficiency to sheet conductance ranges from less than five times at 70 dB to more than fifty times at 160 dB. This reflects merely the advantage in sheet conductance. As argued in section 4.3.4, the effect on eddy currents and related distortions can be expected to be much stronger than linear.

The frequency dependence is strongest at about 100 dB. This can be attributed to the different composition of the shielding efficiency of carbon fibre composites and copper. An exemplary composition of shielding efficiency of a 10 layer carbon fibre composite and a 10 µm copper foil is shown in figure 4.17. Whereas copper based shielding is dominated by reflection, carbon fibre composite based shielding strongly depends on attenuation and at about 100 dB absorption starts to dominate shielding efficiency.

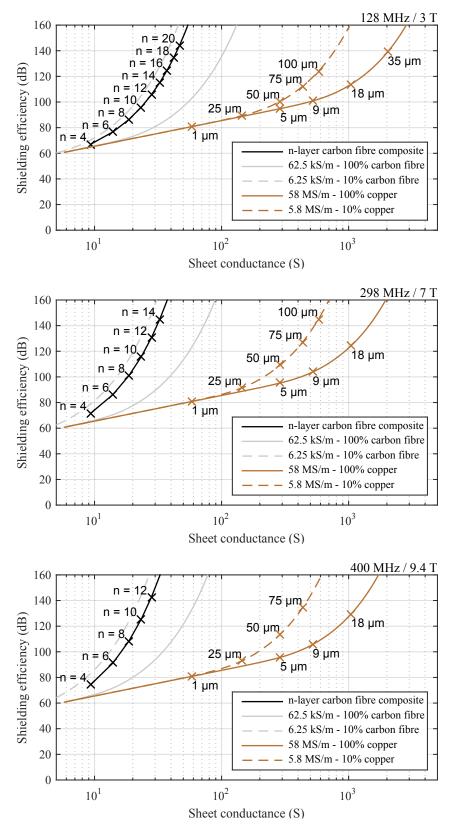


**Figure 4.15** Comparison of shielding efficiency versus sheet conductance. Lower conductive materials provide a higher shielding efficiency to sheet conductance ratio, but require a higher material thickness. Shown data for carbon fibre composite is based on the model derived from measurement data. The shielding efficiency of copper is calculated using the standard model.

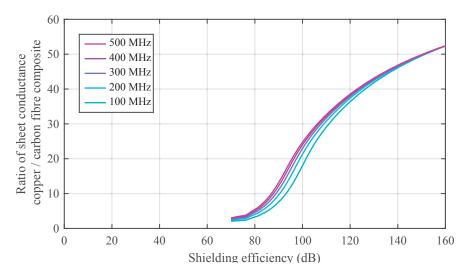


**Figure 4.16** Ratio of sheet conductance versus shielding efficiency of copper to carbon fibre composite. Shown data for carbon fibre composite is based on the model derived from measurement data. The shielding efficiency of copper is calculated using the standard model. The advantage of the reduced eddy current to shielding efficiency ratio of carbon fibre composites increases with shielding requirements and frequency.

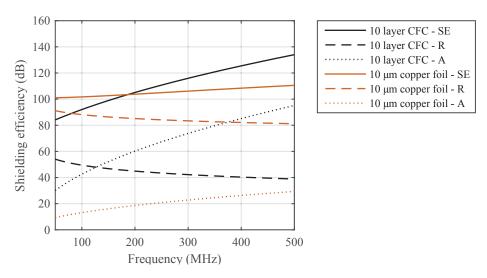


**Figure 4.17** Comparison of reflective shielding (R) and absorptive shielding (A) for a 10 layer carbon fibre composite and a 10 µm copper foil. Whereas the overall shielding efficiency (SE) of copper is dominated by reflective shielding, the shielding efficiency of carbon fibre composites depends more on absorption. This dependency increases with frequency. Data shown is predicted from the model in equation 4.26.

## 4.6 Conclusion

Lower conductive but thicker materials provide a higher shielding efficiency to sheet conductance ratio and are therefore advantageous for PET/MRI shielding. This fundamental advantage is due to the fact that absorption increases exponentially with thickness, whereas sheet conductance increases linearly. Thus, lower conductivity can be overcompensated by increasing thickness. In consequence, the most important parameters to control PET/MRI shielding efficiency and sheet conductance are conductivity and thickness. Electric and magnetic susceptibility are unsuitable to enhance PET/MRI shielding efficiency, because electrical susceptibility is overwhelmed by conductivity, and magnetic susceptibility is restricted to zero by MRI requirements.

In practice, the realisable advantage of lower conductivity materials is mainly limited by the thickness and the availability of materials with respective conductive properties. For PET/MRI, the acceptable thickness is mainly limited by construction space and the gamma transparency of the material, if the shield is placed in front of the gamma detectors. Exactly at this point, carbon fibre composites become interesting for PET/MRI.

The calculated conductivity of carbon fibre composites is about 3000 times lower than that of copper and thus allows the construction of reasonable thin shields with sufficient shielding efficiency. The conductivity of common metals and alloys usually exceeds 10 % of the conductivity of copper, which is too high to improve the shielding efficiency to sheet conductance ratio significantly. For the same reasons, also conductive paints, e.g. silver filled acrylics, can perform only slightly better than copper. Typical silver paint coatings are specified to provide 80 dB to 100 dB of shielding in the MRI frequency range at a specified sheet conductance of 40 S and 25 µm thickness. The calculated conductivity of such a coating is  $1.6 \times 10^6$  S m<sup>-1</sup>, which is about 3% of the conductivity of copper. In consequence, the shielding efficiency of such coatings within the MRI frequency range remains dominated by reflective shielding rather than absorption.

Presented results relate to the TEM shielding efficiency of planar shields with infinite extent. Those restrictions were useful to enable the analysis of experimental data, but in practice those conditions are rarely met. The results are therefore not suitable for precise, application specific shielding efficiency calculations, but they revealed the fundamental advantage of lower conductive shielding materials for PET/MRI. The fact that the shielding efficiency of such materials is significantly more affected by absorption suggests additional application specific advantages, as less power is reflected. In case of RF enclosures, all RF power emitted within has to be absorbed and thus less reflection and more absorption are likely to increase the overall shielding efficiency of the enclosure. Furthermore, this could reduce resonance effects within the enclosure.

The advantages of carbon fibre composites for PET/MRI go far beyond their electromagnetic properties. Rather, it is the combination of electromagnetic shielding with mechanical stiffness, gamma transparency and optical opaqueness that makes carbon fibre composites attractive for PET/MRI. The high mechanical strength and stiffness facilitates the construction of self-supporting housings within the MRI bore, whereas the high gamma transparency and light-tightness are important for the encapsulation of the gamma detector. All those properties have been incorporated in the presented housing design.

The shown fabrication process is one of many possible fabrication processes for carbon fibre composites. However, the process turned out to be beneficial, because it allowed the fabrication of housings as well as flat test specimens. Furthermore, it can be used with virtually any sheet material and thus allows not only the systematic investigation and improvement of shielding materials, but also their quick implementation within a full system. The low required tooling costs make it easily applicable for prototypes and research.

The modular housing concept was very beneficial during the development. Having separate modules with replaceable housing allowed a successive development of the carbon fibre composites in parallel to the other development activities of the Hyperion II<sup>D</sup> system. In combination with the versatile fabrication process, composites including a copper foil layer provided a backup scenario in case the carbon fibre composites would not fulfil the RF shielding requirements. Without having this backup scenario, it would probably not have been possible to include carbon fibre shielding in the Hyperion II<sup>D</sup> scanner.

## 4.7 Outlook

Carbon fibre composites include an enormous variety of material compositions. The kind of fibres, textile structure and embedding matrix offers countless research and optimization opportunities.

An interesting aspect would be to study the influence of the fibre orientation on shielding efficiency. In particular, the extent to which additional fibre angles can improve shielding efficiency and if the strong decrease of reflectivity with frequency is related to it.

Furthermore, the conductivity of the composite could be adjusted to trade-off the desired shielding efficiency, thickness and sheet conductance. Different kind of fibres and coated fibres could be used to increase the conductivity of the composite, e.g. metal-coated fibres or carbon nano tube fibres. In this context, also the conductivity of the matrix could be varied, e.g. by adding conductive filler to the matrix or by using conductive polymers.

All those approaches require a reliable experimental quantification. The results obtained with the used TEM cell are not entirely satisfactory, in particular the limited dynamic range is an issue and requires further optimization. This could potentially be addresses by optimization the TEM cell itself, e.g. impedance matching and suppression of higher modes, as well as the sample preparation, e.g. improving the quality of sample contact surfaces by high conductive, planar coatings.

## Chapter 5

## Optical design of high-resolution depth-of-interaction scintillation detectors

At first glance, the optical design of scintillation detectors is independent of PET/MRI, because the most commonly used scintillator materials for PET, LSO and LYSO, seem to be unaffected by magnetic fields and cause only minor magnetic susceptibility artefacts (Slates et al. 1999a, Yamamoto et al. 2003). This is not self-evident. For example, the light yield of some plastic scintillators have been reported to be susceptible to magnetic fields (Cumalat et al. 1990). Furthermore, other scintillator materials like cerium doped gadolinium oxyorthosilicate (GSO) or cerium doped gadolinium aluminium gallium garnet (GAGG), which are subject to current research, contain ferromagnetic gadolinium and thus might be much more troublesome for PET/MRI in terms of susceptibility artefacts.

However, there is a more implicit impact on detector design, caused by the confined construction space inside an MRI system. The confined construction space forces the PET detector to be placed closer to the scanned object, making it more susceptible to the parallax error. Depth-of-interaction encoding is thus of particular interest for high resolution PET/MRI systems. In addition, the detector should be compact and thin, to make the best use of the available construction space.

Although depth-of-interaction gamma detectors are subject to research for a long time, a truly satisfactory solution has yet to be found. Many of those approaches encode the depth information in the light distribution. The optical design thus is one of the central points of depth-of-interaction scintillation detectors. In the following sections, selected approaches and methods to improve the optical design of scintillation detectors will be assessed.

## 5.1 Introduction

Up to now, most PET detectors are based on pixelated scintillation detectors. The basic design of pixelated scintillation detectors are two-dimensional arrays of cuboid scintillator elements, optically separated by reflectors, and read out at one side by an array of photodetectors. One of the main reasons for the popularity of such detectors is their intrinsic spatial encoding: ideally, each time a scintillator element is hit by a gamma particle it lights up and can thus be identified.

This approach is most straightforward, if each scintillator element is coupled one-to-one to a photodetector. However, in practice the pitch of the photodetector array is often less than the pitch of the scintillator array. Pixelated scintillation detectors thus often require a lightguide between the scintillator and the photodetector array. The lightguide distributes the scintillation light of each scintillator element to a number of photodetectors, such that the hit crystal can be identified based on the resulting light distribution. In the simplest case, the lightguide is an optical transparent plate, e.g. a glass plate.

Most commonly, each scintillator element is polished and covered by a good specular reflector, to increase the light yield and uniformity. However, such plain scintillator arrays provide almost no depth information (Yang et al. 2009b). To add depth information, a wide variety of modifications and different approaches have been investigated. A basic overview of depth-of-interaction approaches is summarized in Table 5.1.

Very good results have been achieved with double-sided readout of pixelated scintillator arrays. Depending on the surface properties of each crystal, the amount of photons received by each readout side is depth-dependent. By its very nature, a double-sided readout requires a second layer of photodetectors. In consequence, it also requires more construction space, power and cooling, which is all undesirable, in particular for PET/MRI. Moreover, one of the photodetectors will be placed in front of the detector, which results in additional gamma scattering and attenuation.

With the advent of thin, solid-state based photodetector, it became possible to simply stack multiple detector layers (McElroy et al. 2005, Moehrs et al. 2006). Although straight forward, this approach basically suffers from the same drawbacks as the doublesided readout, but it might be advantageous in terms of temporal resolution and simplified optical design, because of thin crystal layers. Furthermore, the use of distinct layers might improve the detection and correction of Compton scattering within the detector, because the deposited energy in each layer is measured independently.

For monolithic detectors, double-sided and single-sided readouts schemes have been implemented to encode depth information. Although sub-millimetre spatial resolution has been shown with thin monolithic scintillators (España et al. 2014), monolithic scintillators suffer from a very wide light-spread and non-trivial calibration.

The wide light-spread of monolithic detectors usually requires very low dark-count rates in order to avoid excessive dead-time of the detector, which commonly results in extensive cooling of solid-state detectors. If in addition also very low trigger thresholds for time-of-flight measurements are required, detector temperatures of  $-25.0 \pm 0.1$  °C have been reported (Borghi et al. 2015). Although such conditions are reasonably achievable in a laboratory environment, they require considerable effort to be implemented on system level.

**Table 5.1** Overview of depth-of-interaction approaches. A large variety of approaches have been investigated, which emphasizes the importance of measuring the interaction depth for PET. However, until now, none of the approaches could clearly prevail, since all approaches suffer from side-effects to a certain degree.

Approach	Reference
Two-sided readout of pixelated scintillator arrays	
- $0.5 \mathrm{mm}$ to $0.7 \mathrm{mm}$ pitch LSO arrays	James et al. 2009
- 1 mm pitch LSO arrays	Yang et al. 2009a
- Trapezoidal LSO array	Yang et al. 2011
Detector sandwich	
- MADPET-II, double-layer APD readout	McElroy et al. 2005
- Multi-layer monolithic LSO with SiPM readout	Moehrs et al. 2006
Monolithic detectors	
- single-sided readout	Lerche et al. 2005
- double-sided readout	Maas et al. 2009
Scintillator slabs, kind of semi-monolithic detector	
- Trapezoidal slat	Xiaoli Li et al. 2010
- Trapezoidal slat crystal	Miyaoka et al. 2011
<ul> <li>Stacked phoswich approach</li> <li>Three layer, LSO, GSO and BGO</li> <li>Raytest ClearPET, dual-layer, LYSO and LuYAP</li> <li>GE Healthcare eXplore VISTA, dual-layer, LYSO and GSO</li> </ul>	Seidel et al. 1999 Sempere Roldan et al. 2007 Wang et al. 2006
- Dual-layer GSO with different dopant conectrations	Okumura et al. 2015
Continuous phoswich approach	
- Partially phosphor-coated LSO	Du et al. 2009
<ul> <li>Staggered approach, pixelated arrays with relative offsets</li> <li>Double-layer LSO arrays with 1.8 mm pitch on PS-PMT</li> <li>LYSO arrays with 1.2 mm to 1.6 mm pitch on SiPM array</li> <li>LYSO array with 1.27 mm pitch on digital SiPM array</li> <li>Four-layer, successive x-y-x shift, 1.565 mm pitch LSO arrays</li> </ul>	Liu et al. 2001 Thompson et al. 2012 Stortz et al. 2015 Ito et al. 2010
Stacked approach	
- Four-layer, partial reflectors and light-sharing	Nishikido et al. 2013
Partial light sharing	
- Single layer, triangular structured reflectors	Lee and Lee 2015
Single-sided readout of pixelated scintillator arrays - LSO array with roughened surfaces and specular reflector	Yang et al. 2009b

Since monolithic detectors have by their very nature no intrinsic spatial structure, the precise calibration of monolithic detectors requires a reference scan, for example with a known gamma ray beam profile. This process can be very time-consuming, e.g. if a very narrow pencil beam is used. Furthermore, in system calibration can be impeded in case of small bore diameters. More advanced calibration methods are subject to research (Borghi et al. 2015, España et al. 2013), but it still has to be proven that those methods are reasonable to be used for calibrating entire PET scanners.

Furthermore, the quality of the scintillator material (e.g. inclusions or voids) directly influences the obtainable results, which might result in yield problems. Monolithic scintillators thus promise to be an interesting alternative to pixelated scintillators, but they are still facing a number of issues that have to be investigated.

A very different approach is the so-called phoswich approach. The phoswich approach encodes the depth information by different decay times of the scintillation pulses. This can be achieved by various methods, for example by different kind of scintillator materials, different dopant concentrations, or by partially coating scintillators with a phosphor. Depth information can thus be added to an already existing two-dimensional encoding scheme. Since no light sharing between multiple photodetectors is required, a one-to-one coupling to photodetectors remains feasible, which is advantageous to avoid excessive dead time and additionally simplifies the identification of Compton scattering within the detector. Though, additional effort is required to measure the decay time of each scintillation pulse, for example by direct sampling of the waveform or by applying multiple integration intervals (Roncali et al. 2012). Not all kinds of photodetectors and readout systems are capable to do so. For example, the current implementation of the digital SiPM measures only one integral value of photon counts, but not their temporal distribution. Phosphor coatings avoid the use of different scintillator materials, but the coating can reduce the light yield, energy and timing resolution (Schmall et al. 2014). So far, two commercial, small-animal PET scanners have been realized with a dual-layer phoswich approach, the GE Healthcare eXplore VISTA and Raytest ClearPET.

Easier to implement and calibrate are stacked and staggered approaches. The basic idea of stacked and staggered approaches is to combine multiple pixelated scintillator arrays, so that each crystal maps to an individual spot in the position histogram. For the stacked approach, this is usually achieved by modifying the reflectors for each layer and thus distribute the light of each layer slightly different. For the staggered approach, each layer is offset, e.g. by half a crystal pitch, and no reflector modifications are required. The main advantage of the stacked and staggered approach is that they only require a single-sided readout and that the intrinsic spatial encoding of pixelated scintillator arrays is maintained. Though, the separability of spots in the position histogram usually degrades, because the number of spots per area increases with the number of layers. The stacked and staggered approach are limited to a set of few discrete layers. So far up to four-layers have been successfully implemented (Nishikido et al. 2013).

A depth encoding with partial light sharing can also be implemented by partially removing the reflector between crystals, e.g. by using triangular shaped reflectors (Lee and Lee 2015). Such approaches promise a continuous depth encoding with single sided readout, although such configuration might be very difficult to fabricate for very fine pitched scintillator arrays.

Like most state-of-the-art PET systems, the Hyperion  $II^{D}$  system is designed with single-sided readout and pixelated scintillator arrays. Favour was given to a pixelated scintillator design, because of its empirically proven feasibility on system level. This already limited the choice of depth-of-interaction approaches. Furthermore, phoswich approaches are difficult to realize with the current implementation of the digital SiPM. Thus, for the Hyperion  $II^{D}$  system, the choice of depth-of-interaction approaches is basically limited to staggered, stacked and partial-light sharing approaches. From a practical point of view, the staggered approach appears easiest to be implemented, because common plain scintillator arrays can be reused, rather than requiring arrays with specific reflector arrangements.

In the course of my work I dealt with various aspects of scintillation detectors, including experimental studies as well as optical simulations. Some of them will be addressed in the following four sections. At first, a brief experimental study of a common staggered and a novel stacked approach is presented. Secondly, a novel method to measure the light distribution of individual crystals in a scintillator array with sub-channel resolution is shown, using the specific capabilities of the digital SiPM. Third, optical simulations are incorporated to amend the experimental investigations. Finally, optical simulations are used to investigate a novel reflectorless pixelated scintillator configuration, which potentially could provide a continuous depth encoding with single-sided readout and avoid the use of inter-crystal reflectors.

# 5.2 Feasibility study of dual-layer, pixelated scintillation detectors using a digital SiPM and single-sided readout

## 5.2.1 Introduction

This brief feasibility study of dual-layer pixelated scintillation detectors aimed to assess a potential depth-of-interaction encoding for the Hyperion II<sup>D</sup> PET/MRI insert. It was carried out at the very beginning of the project, shortly after the digital SiPM became available.

Three different detector configurations were experimentally investigated: a plain scintillator array, a dual-layer staggered array and a novel stacked array approach. The basic design of these three configurations is outlined in figure 5.1.

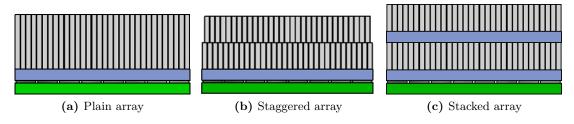


**Figure 5.1** Schematic view of plain, staggered and stacked scintillator arrays. Whereas the plain array (a) is a single regular array of scintillator elements separated by a reflective film, the stacked and staggered arrays are composed of two such arrays. The arrays of the staggered array (b) are shifted by half a crystal pitch in x- and y-directions. The arrays of the stacked array (c) are aligned flush, but separated by an additional light guide.

The plain array is used as a reference for a single-layer array without depth-encoding. Although the dual-layer staggered approach is basically well known, the scintillator array used here has a crystal pitch of only 1 mm. The finer the crystal pitch, the more scintillator elements per area have to be encoded in the position histogram, which will decrease their separability. This motivated to stack two scintillator arrays on top of each other, flush aligned but separated with an additional lightguide. The light of the upper array should thus spread further while maintaining the same position in the position histogram.

## 5.2.2 Experimental investigation

Three different detectors were constructed as follows:

First, a plain array. The plain array is composed of  $32 \times 32$  polished LYSO crystals with 1 mm pitch, mounted on a 2 mm thick light guide. The size of each crystal is  $0.9225 \times 0.9225 \times 12 \text{ mm}^3$ . Individual crystals are separated by a 65 µm thick specular reflector film (3M Vikuiti<sup>TM</sup> ESR), similar as the outer top and side surfaces are covered with. The reflector and the scintillators are bonded full-face with a transparent acrylic adhesive with a refractive index of 1.47 (Dymax OP-29).

Second, a staggered array. The staggered array is composed of two scintillator arrays and a bottom light guide. Both arrays were mounted on top of each other with half a crystal pitch offset in x- and y-directions. For that purpose, a plain scintillator array was cut into two halves, the upper half 5.2 mm thick and the lower half 6.6 mm thick. The different thickness was chosen to balance the gamma interaction probability between both layers. Furthermore, the top layer will be closer to the field-of-view and it is thus advantageous to keep it thinner to reduce the parallax effect. Subsequently, the staggered array was mounted on a 2 mm thick light guide.

Third, the stacked array. The stacked array is composed of two scintillator arrays as used for the staggered array, but stacked without an offset and separated by an additional light guide. The light guide between the two arrays is 2 mm thick, whereas

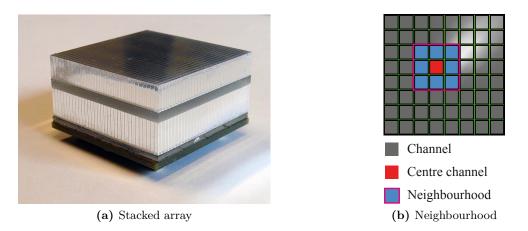


**Figure 5.2** (a) Stacked array without outer reflectors. The upper layer is 5.2 mm and the bottom layer is 6.6 mm thick. The upper layer was chosen to be thinner to distribute the gamma detection probability equally. The upper lightguide is 2 mm and the bottom lightguide is 1 mm thick. (b) Illustration of neighbourhood definition used for positioning.

the light guide between the bottom layer and the photodetector is 1 mm thick. Thus, the light of the upper array should spread out wider than the light of the bottom array. A picture of the mounted stacked array is shown in figure 5.2 (a).

All three arrays were successively mounted on a  $8 \times 8$  channel digital SiPM array (PDPC DPC6400-22-44) with 4 mm pitch. The digital SiPMs were operated at 3.3 V over-voltage and the noisiest 10% of cells were disabled. The trigger threshold was set to 2 photons per channel and the validation interval was set to 45 ns.

All light guides were made of borosilicate glass plates with a refractive index of 1.55. The scintillator arrays, light guides and photodetectors were mounted with an optical clear thermoplastic compound (Cargille Meltmount<sup>TM</sup>, ND = 1.582).

In order to evaluate the three detector configurations, all three arrays were successively irradiated with a  $^{22}$ Na point source from the top. The source was placed approximately 20 cm above each array.

In addition, each layers of the stacked array was irradiated from the side. To perform coincident measurements, an additional reference detector was used. The reference detector consisted of four  $4 \times 4 \times 16 \text{ mm}^3$  LYSO crystals wrapped in PTFE tape, mounted on an additional digital SiPM array. Selective irradiation was implemented by electronic collimation of the gamma beam using coincident measurement data and aligning the <sup>22</sup>Na point source as illustrated in figure 5.4. Measurements were carried out in a light-tight box at approximately 23 °C ambient temperature.

Measurement data was post-processed with Matlab. For each coincident event an xand y-position were calculated as

$$\begin{split} x &= \sum p_n \cdot x_n, \quad n \in neighbourhood \\ y &= \sum p_n \cdot y_n, \quad n \in neighbourhood , \end{split}$$

where  $p_n$  represents the photon count value and  $x_n$  and  $y_n$  the centre position of the channel n. Only the channel with the highest photo count value per event and the adjacent eight channels, which are defined as a *neighbourhood*, are included. Figure 5.2 (b) illustrates the neighbourhood principle for a digital SiPM array. Events with incomplete neighbourhood data are discarded in the analysis.

The cause of incomplete neighbourhood data is that the digital SiPM is a selftriggering device. Basically, each channel has to receive a certain amount of light within a given time to initiate a readout process. At the time of the experiment, there was no common trigger logic for an entire digital SiPM array implemented. Channels further away from the main channel receive little light, which decreases their trigger probability. Moreover, the trigger network is implemented by a logic tree structure, which logically combined certain cell areas. In consequence, the trigger threshold is affected by statistical variations as well as inhomogeneous light distributions.

Furthermore, missing channels can be caused by dark noise and subsequent dead time. Thus, not all channels are sensitive all time, and in consequence not all channels are present for all events. In practice, the problem is even more complicated by the fact, that  $2 \times 2$  channels are grouped on one silicon die and share a common trigger and readout logic. If one of the four channel on a die triggers, all four channels are read out. This saves logic elements, in particular for the time-stamper, and thus increases the fill-factor of the device. The drawback of this approach is, that if even only one channel triggers on noise, all four channels are affected by the subsequent dead-time. A more detailed analysis of this problem and the effect on PET performance can be found in Schug et al. 2015c.

The obtained x- and y-positions are summarized in two dimensional histograms with a bin size of  $50 \times 50 \,\mu\text{m}^2$ , an empirical value fine enough to render the specific features of the position histograms and coarse enough to avoid noisy and unnecessary large data sets. Measurement data was corrected for non-linearity but no gain calibration was applied. Gain calibration has been omitted primarily for the sake of simplicity and obtained results showed no compelling necessity to apply it later on to demonstrate the basic operating principle of the investigated detector configurations.

In case of the stacked array, the light distribution was additionally analysed for a depth effect. For this purpose, the ratio of the maximum photo count value to its neighbourhood was calculated for each event and used as measure of the width of the light distribution. This measure behaves inversely to the width of the light distribution, i.e. lower values indicate a broader light distribution, since less light is deposited on the centre channel.

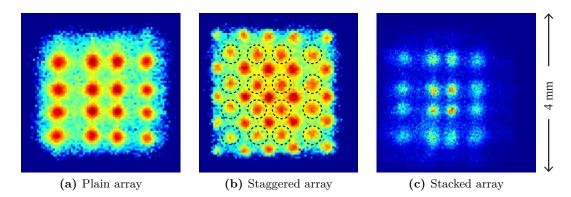


**Figure 5.3** Measured position histograms of plain, staggered and stacked array. (a) Each of the 16 spots of the plain array correspond to a single crystal. (b) In case of the staggered array, two similar patterns are overlaid but shifted by half a crystal pitch in x- and y-directions. The spots belonging to the bottom crystal layer are marked with dashed circles. (c) The position histogram of the stacked array shows a similar structure as the plain array. No depth information is apparent from the position histogram. Shown data is normalized and shown on a logarithmic scale. The intensity variations of the spots of the stacked array can be attributed to a loss of sensitivity because of the used triggering scheme, i.e. the chance to obtain complete data sets tends to be lower for the crystals along the channel borders. This is in particular an issue of the stacked array, because the width of the light distribution depends on the hit layer. In addition, the spots of the stacked array appear to be shifted down to the left, which indicates that the stacked array is more susceptible to photodetector imperfections, i.e. the insensitive areas caused by detector borders and bond gaps.

### 5.2.3 Results

Figure 5.3 (a-c) summarizes the obtained position histograms. Each figure shows a  $4 \times 4 \text{ mm}^2$  detail of the positioning histogram of the respective detector configuration. The shown area corresponds to a single digital SiPM channel.

For the plain array, the position histogram in figure 5.3 (a) shows 16 individual spots, each corresponding to a single crystal. All spots are clearly separated, thus position encoding for this type of scintillator array is straightforward.

For the staggered array, there are on average twice as many crystals located above one digital SiPM channel. As expected, the position histogram of the staggered array in figure 5.3 (b) shows clearly more spots. In total, 41 spots can be identified. Sixteen of those spots belong to the bottom layer array. The remaining 25 spots belong to the top layer array. The number of spots belonging to the top layer is 25 rather than 16, because the top layer is shifted by half a crystal pitch. Thus,  $5 \times 5$  crystals of the top layer overlap in the area of one digital SiPM channel, although the edge and corner crystals overlap only by 50% and 25%, respectively. Positioning and layer identification is thus possible using the obtained 2D-position histograms only. The calibration data for crystal identification can be derived from the measurement data without requiring a dedicated calibration scan or special equipment. For the stacked array, the position histogram in figure 5.3 (c) shows 16 spots, similar to the position histogram of the plain array. This indicates, that the calculated crystal positions of

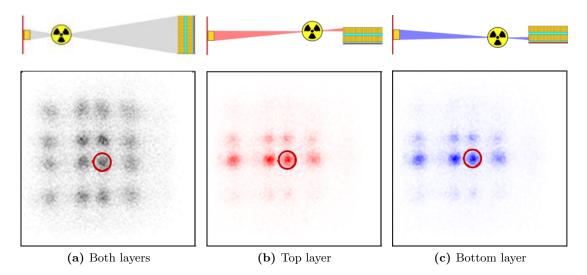


**Figure 5.4** Measured  $4 \times 4 \text{ mm}^2$  position histograms of stacked array for (a) both, (b) top and (c) bottom irradiation. Electronic collimation was used to separate the top and the bottom layer. Because of the electronic collimation, the effective irradiation beam is very narrow in these cases and only a narrow range of crystals is hit. The colour coding indicates the electronic collimation configuration used. Figure by Dueppenbecker et al. 2011b, © 2011 IEEE

the top and bottom layer superimpose as intended. Figure 5.4 confirms this. Here, the stacked array was irradiated from the side. To avoid the use of a collimated gamma beam, electronic collimation was used to separate the top and bottom, i.e. the reference detector, the source and the layer of interest are aligned in line and only coincident events are included in the analysis.

As shown in figure 5.4 (b,c), the position histograms of both layers are aligned with each other. Thus, the x- and y-positions of each crystal can be determined from the superimposed position histogram. However, the hit crystal layer remains unknown.

In order to obtain information about the hit crystal layer, the width of the light distribution was analysed. A single spot of the position histogram was selected for the analysis. The respective spot is marked with a red circle in figure 5.4. For all events belonging to this spot, the ratio of the amount of light measured by the centre channel to the sum of light measured by its neighbour channels was calculated as an indicator of the width of the light distribution. The result, shown in figure 5.5, reveals that the width of the light distributions differs for each layer. As intended by the additional light guide, the scintillation light originating from the top layer spreads wider than the light from the bottom layer. Thus, the hit crystal layer can be identified based on the width of the light distribution.

However, the separation is not perfect, because the histograms of the top and bottom layer overlap. There might be different reasons for this. One the one hand, Compton scattering might cause scintillation processes in multiple crystals and layers and thus widen the light spread. On the other hand there are statistical variations in the amount

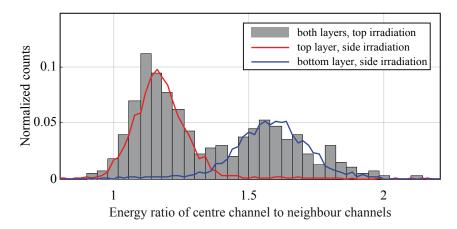


Figure 5.5 Measured energy ratio of centre channel to neighbour channels, which is used as indicator for the width of the light distribution. The used measure behaves inverse to the width of the light distribution, thus a lower values indicate a wider light spread. As expected, the light of the top layer spreads wider, resulting in comparatively less energy on the centre channel. Thus, the hit layer can be identified using the width of the light distribution. Figure by Dueppenbecker et al. 2011b, © 2011 IEEE.

of photons received per channel, which directly influences the measured width of the light spread.

#### 5.2.4 Discussion

Presented results demonstrate the basic feasibility of dual-layer, high-resolution, pixelated scintillation detectors based on digital SiPMs. Whereas the staggered approach is purely based on the position histograms, the stacked approach combines straight forward position encoding with additional depth-of-interaction information obtained from the shape of the light distribution. This has the advantage that the distances between the individual spots in the position histogram remains larger than for the staggered approach and thus improves the separability of the x- and y-positions. Yet, the position accuracy seems to be slightly degraded compared to the plain array, as the spots are compressed in a smaller area. However, neither the light guides of the plain nor the stacked approach were optimized. A disadvantage of the stacked approach is the additional light guide, as it increased the height of the detector and requires an additional gluing layer.

A clear advantage of both approaches is their straightforward encoding. In contrast to most monolithic approaches, neither the staggered nor the stacked approach require a dedicated calibration apparatus, e.g. pencil beam scanning. Calibration data can be obtained from regular measurement data, which is a very beneficial property, in particular for system integration.

Based on the obtained results, it is difficult to predict the performance on system level, e.g. energy and time resolution were not further investigated. Furthermore, the used encoding scheme could decrease the sensitivity of the detector, because it requires for each event data sets with a complete neighbourhood. Events with missing channels are discarded and thus decrease the sensitivity of the detector. However, the ratio of affected events is difficult to determine. There might be systematic variations because of the location of the crystal relative to the digital SiPM channels as well as the layer. Furthermore, the chosen operating parameters of the digital SiPM will impact the achievable performance, e.g. a higher trigger threshold might reduce the risk of losing events because of dark counts, but at the same time might increase the risk of losing information of channels with low photon counts.

The presented investigations were carried out with respect to the development of the Hyperion  $II^D$  system, but in a very early phase. At this time, the design of the digital SiPM for the Hyperion  $II^D$  system was still under development and only limited experience with the operation of the digital SiPM was available. It thus was unclear how the final digital SiPM design would perform and if and how the quality of the digital SiPM might vary for larger batch sizes. In consequence, a conservative single layer approach was chosen for the Hyperion  $II^D$  system.

Besides the basic feasibility, this study showed that the light distribution contains more information than directly observable from the position histograms. Understanding the light distribution is therefore a key for developing further high resolution detectors. This motivated to learn more about the light distribution and led to a novel method to measure the light distribution more precisely, utilizing the unique properties of the digital SiPM, which will be presented in the following section.

# 5.3 A method for measuring the sub-channel light distribution of digital SiPM based scintillation detectors

### 5.3.1 Introduction

As demonstrated in the previous section, the light distribution contains multiple information. Basically, most geometrical and optical improvements of scintillation detectors finally aim to shape the light distribution. Thus, knowing and understanding the light distribution is a prerequisite for the systematic improvement of scintillation detectors. This immediately raises the question, how the light distribution can be properly measured.

An example light distribution as routinely obtained for a single event in a plain scintillator array is shown in figure 5.6. The resolution of the gained information corresponds to the detector pitch of 4 mm, which is rather coarse compared to the 1 mm scintillator pitch. In effect, this coarse sampling acts as low-pass filter and blurs the details of the actual light distribution. It represents only an average of the light distribution per channel, but more local effects are hidden. This is unsatisfactory, in

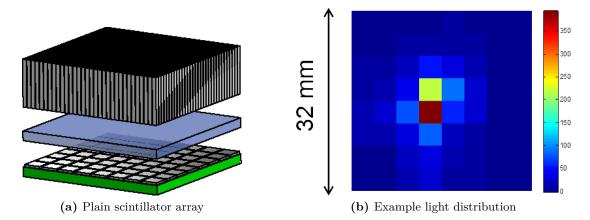


**Figure 5.6** (a) Plain scintillator array with light guide and photodetector array with 4 mm pitch. (b) An example measured light distribution of a single scintillation event. The resolution of the light distribution corresponds to the pitch of the photodetector array. Figures by Dueppenbecker et al. 2011a, © 2011 IEEE.

particular because SPAD array based photo detectors are composed of a much finer grid of photodiodes and thus in principle contains the required information.

Like common analogue SiPMs, the digital SiPM consists of an array of photodiodes, operated in Geiger-mode. But in contrast to the analogue SiPM, the digital SiPM monitors and reads out the break down of each photodiode individually. In principle, the digital SiPM thus records the light distribution on single photodiode level. Unfortunately, this information is available only inside the digital SiPM itself. To reduce the output bandwidth, the number of hit cells is summed up digitally per event and only the sum of hit cells is output. A direct readout of the full light distribution is thus not possible.

However, the digital SiPM provides another very useful feature: each single photodiode can be enabled and disabled by programming a so called inhibit pattern. As shown in figure 5.7, each cell logic contains a memory bit to enable or disable the respective cell. For regular use, a uniquely determined inhibit pattern is programmed, which disables a certain ratio of the most noisy cells to reduce the dark count rate and the dead time. The inhibit pattern is routinely programmed each time after powering up the digital SiPM. For programming, the cell activation pattern is bitwise shifted in via a serial digital interface. This only takes few operations and the entire inhibit pattern of a digital SiPM can be reprogrammed within a couple of milliseconds. The inhibit information itself is stored in a volatile memory registers next to each photodiode and can be reprogrammed as often as desired.

At first glance, the obvious approach to utilize the cell inhibit feature for sub-channel measurements is to successively activate small cell areas and thus measure the amount of light at that area. Using this approach, even single photodiode cells can be read out

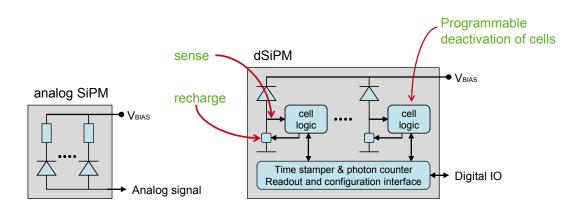


**Figure 5.7** Digital SiPM cell logic. In contrast to conventional SiPMs, each SPAD of the digital SiPM is controlled and read out individually. This includes the possibility to deactivate individual cells. Figure by Dueppenbecker et al. 2011a, © 2011 IEEE.

individually. Unfortunately, the majority of light information is lost. In consequence, it becomes difficult to calculate the origin of the gamma interaction.

This problem could be partially overcome if the position and energy of the gamma interaction is known a priori, e.g. if single scintillator elements are selectively irradiated with a monoenergetic radiation beam. However, selective gamma irradiation is troublesome in practice. In principle, a pencil beam can be used, but the formation of a sufficient thin beam requires an appropriate collimator, precise alignment and usually a strong radiation sources to compensate for the narrow solid angle. But even then, detector scatter is inevitable, which will impact the amount of deposited energy and spread the interaction volume. Furthermore, one has to account for noise, e.g the dark count rate, but also the intrinsic radioactivity of the scintillator material.

For investigating depth-of-interaction effects, the practical challenges increase even more, because the point of gamma interaction is randomly distributed. Lateral irradiation can not circumvent this deficiency, because then the x- and y-positions of the interaction have to be determined.

It thus requires an approach that maintains the positioning and energy information of single events. These considerations led to the following approach of selectively deactivating small cell areas and thus measure the light distribution indirectly.

### 5.3.2 Measurement method and application

As explained above, selective cell activation is unsuitable to measure the light distribution on sub-channel level. But what happens, if the principle is inverted into cell deactivation? If only a small area of the detector is deactivated, there should remain sufficient information to calculate the interaction position as usual. Yet, the measured photon count values will be slightly lower, namely by the amount of light that would regularly be detected by the deactivated detector area — which is precisely the information sought. Thus, by subtracting the photon count value of the deactivated pattern from the photon count value of the regular patter, the amount of light hitting the deactivated area can be calculated.

For a single measurement, however, the respective regular value is unknown. Thus, the experiment has to be repeated, once with the regular and once with the partially deactivated detector. Furthermore, measured photon count values are subject to statistical fluctuation, e.g. the amount of photons falling on a certain area will vary, as well as their probability to be detected. Thus, in order to separate the desired information from statistical noise, the measurement has to be repeated for a plurality of equal events. From that, the average amount of light can be calculated for the respective area. If this process is repeated for all areas of interest, the results can be composed to a light distribution map.

To show the feasibility of this method, a light distribution measurement of a single scintillator crystal within a plain scintillator array was performed.

A plain array as described in the previous section was used,  $32 \times 32$  LYSO crystals with 1 mm pitch and 12 mm length, separated by a specular reflector film. The scintillator array was mounted with a 2 mm borosilicate light guide to an  $8 \times 8$  channel digital SiPM array with 4 mm pitch, similar to the Philips Digital Photon Counting DPC-6400-22 array. Each digital SiPM channel is composed of 6400 photodiodes<sup>1</sup>, arranged in an array of  $64 \times 100$  cells. The size of each cell is about  $60 \times 32 \,\mu\text{m}^2$ , resulting in an active area of  $3.8 \times 3.2 \,\text{mm}^2$  per channel. The remaining area of each channel is occupied by digital logic and electrical bonding areas.

For the regular inhibit map, the most noisy 10% of channels were disabled. An example of such a map for a single channel is shown in figure 5.8 (a). Starting from the regular inhibit map, additional areas were successively disabled to implement the sub-channel sampling. A rectangular area of  $8 \times 20$  cells was chosen as sampling area, which corresponding to an area of approximately  $475 \times 640 \,\mu\text{m}^2$ . This pattern was row-and column-wise shifted and combined with the regular inhibit pattern, so that the entire area of each channel is successively covered. Thus, 40 individual inhibit patterns for sampling were calculated for each channel. An example pattern of a single channel and the first of the 40 inhibit sampling patterns is shown figure 5.8 (b).

To obtain the light distribution of an entire sensor tile, this process has to be repeated for all channels, which could be done sequentially, but to shorten the measurement time each sampling pattern is applied simultaneously to all 64 channels. Figure 5.8 (c) shows an example inhibit map, where the same sampling pattern is applied to all 64 channels.

The scintillator array was operated with the same measurement equipment as described in section 5.2.2. The digital SiPMs were operated at 3.3 V over-voltage, the

<sup>&</sup>lt;sup>1</sup>Actually, each channel consists of 6396 photodiodes. The area of the 4 centre cells of each channel are used for digital logic. However, logically they exist and can be programmed, but without having any functionality.

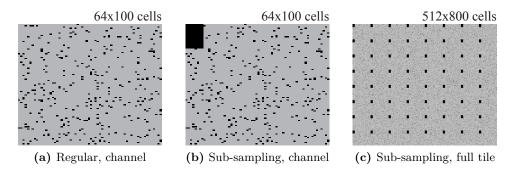


**Figure 5.8** Example inhibit patterns. Gray indicates activated cells and black deactivated cells. (a) The regular inhibit pattern disables 10 % of the most noisy cells. (b) For sampling the light distribution, additional areas are deactivated. The sampling pattern is successively shifted row- and column-wise to cover the entire sensitive area of each channel. (c) To shorten the measurement time, the sampling pattern is applied simultaneously to all 64 channels.

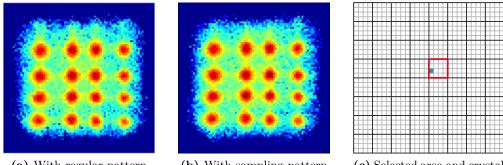
trigger threshold was set to 2 photons per channel and the validation interval was set to 45 ns. The measurement set-up was operated in a light-tight box with a ventilation system in a laboratory room with air conditioning. The ambient temperature of the detector was approximately 21 °C. Data was collected for the regular and the 40 sampling inhibit patterns and post-processed with Matlab. Only coincident events were used. The measurement time was about 100 min per each of the 40 inhibit patterns.

During post-processing, position histograms were calculated using the same positioning algorithm as described in section 5.2.2, including the neighbourhood criterion. From the position histograms, events belonging to a single crystal were selected and the respective energy histogram was computed. Based on the energy histogram, the position of the 511 keV photopeak was determined by fitting a Gaussian distribution. For all measurements with sampling inhibit patterns, the position of the photopeak was subtracted from the regular photopeak position. The result was saved as light distribution matrix.

### 5.3.3 Results

Figure 5.9 (a,b) shows two example position histograms, one recorded with the regular inhibit pattern and one with a sampling pattern. Both position histograms show 16 clearly separated spots, each corresponding to a single scintillator crystal. This measurement confirms that the additional deactivation of cells does not hinder crystal identification, which is a necessary condition for further data analysis.

In the next step, events belonging to a single spot are selected and the energy histograms for all channels and each sampling pattern are calculated. An example energy histogram is presented in figure 5.10. At first glance, the difference in the photo peak position is hardly apparent, but fitting a Gaussian distribution to it reveals the slightly



(a) With regular pattern

(b) With sampling pattern

(c) Selected area and crystal

Figure 5.9 Position histogram with regular inhibit pattern and sampling pattern. Visually they are the same and both allow the separation of spots and identification of related crystals.

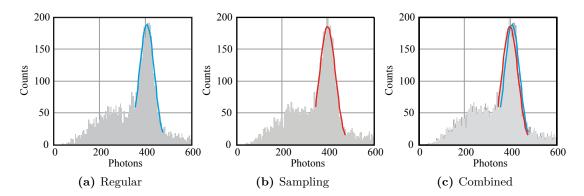


Figure 5.10 Computing principle of sub-channel photon counts. The regular energy histogram is very similar to the energy histogram with the sampling pattern. Only the superposition of both reveals the slight decrease in photon count values when the sampling pattern is applied. The difference in the photo peak position correspond to the amount of light that would regularly be measured by the sampling area.

lower photon count values measured with the sampling pattern. The results of all energy differences are collected in the light distribution matrix.

Figure 5.11 shows the obtained light distribution matrix. For clarification, the light distribution matrix is overlaid on a picture of the sensor tile. Gray areas mark insensitive areas. Most light is concentrated on the centre channel and its direct neighbours, but within a channel the light intensity is inhomogeneously distributed. The measured photon counts per channel vary by an order of magnitude. In addition, the bond gaps and their disruption of the sensitive areas are striking.

### 5.3.4 Discussion

The example shown demonstrates, how by successive deactivation of small cell areas the digital SiPM can be used to measure the light distribution with sub-channel resolution. There are two main advantages of this method. First, it can be applied to original detector assemblies without hardware modifications. No dedicated measurement equipment is required, the required modifications are all done by programming the

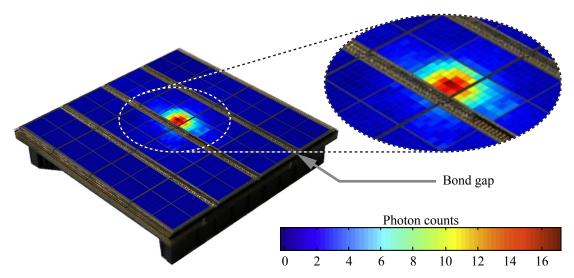


**Figure 5.11** Measured sub-channel light distribution in overlay with a picture of the sensor tile. The presented detail corresponds to the neighbourhood criterion as used for positioning. The majority of light is focused on the neighbourhood area. Gray areas mark insensitive areas, e.g. the bond gaps, which are required for electrical connections.

sampling inhibit patterns via software. Second, it allows the use of regular positioning schemes and thus circumvents the use of selective irradiation, e.g. with a pencil beam. Thereby, more detailed information about the light distribution of the real detectors can be obtained.

The example shown reveals, how the light distribution varies even within a single channel. This becomes particularly evident for the centre channel. Yet, in many practical applications a homogeneous light distribution is assumed, e.g. for the saturation correction or the triggering scheme of the digital SiPM. In consequence, such methods should be applied with caution.

The knowledge of the light distribution could be used for the design of future photodetectors. On the one hand, the pitch and fill factor could be optimized to best match the light distribution. On the other hand, it could be used to improve the design of position sensitive detectors. There already exist a number of position sensitive photodetectors, e.g. different variations of position sensitive APDs and SiPMs (Fischer and Piemonte 2013, Li et al. 2014, Schmall et al. 2012, Schulz et al. 2013). They all include an intrinsic position encoding to reduce the number of output channels. However, the intrinsic position encoding implicitly assumes a certain light distribution. Thus, knowing and understanding the light distribution is a key to further improve such detectors.

However, also the presented method has some weaknesses. First, it measures an average light distribution, rather than the light distribution of single events. Second, it still requires a working positioning scheme. The positioning scheme itself thus might influence the measured result, e.g. if events are discarded because not all neighbour channels triggered. Such events will also be discarded from the calculation of the light

distribution and thus the obtained light distribution might be biased, e.g. in the case of systematic lower trigger probabilities for certain events. Third, the measurement time can be very long and increases linearly with the number of sampling areas. The measurement time for the shown example was about 100 min per inhibit pattern, thus more than two days to measure all 40 sample pattern. This clearly limits the application of the method, e.g. for series of measurements with different detector configurations. Furthermore, the long measurement time bears the risk, that the test environment changes during the measurements, e.g. temperature variations, and thus might influence the detector. However, the measurement time neither depends on the number of channels nor the number of scintillator elements.

Inevitably, the properties of the digital SiPM will influence the measured photon count values, e.g. the photon detection efficiency, permanently deactivated or defect cells, optical crosstalk or noise will influence the results. In consequence, the quantitative significance of this method is difficult to assess. It is thus primarily intended as tool to investigate the shape of the light distribution and to demonstrate how the cell deactivation feature of the digital SiPM can be utilized beyond dark count rate reduction.

### 5.4 Optical simulation of pixelated scintillation detectors

### 5.4.1 Introduction

The two previous sections presented two experimental examples of detector research. In the course of this work, a lot of practical experience could be gained, in particular how to operate and handle digital SiPMs and fine-pitched scintillator arrays. This was very helpful for the development of the Hyperion II<sup>D</sup> system. However, hands-on experience also revealed a number of shortcomings.

First of all, experimental approaches make it difficult to separate problems, because the characteristics of the scintillator configuration and the photodetector superimpose. In consequence, the number of parameters and interdependencies complicate the interpretation of measured data. An example of this is the trigger logic of the digital SiPM. Its configuration directly influences the trigger probability. In consequence, the number of missing channels and the amount of observable information varies, although the scintillator configuration is the same. But also external parameters, like the temperature, can directly influence the measurement results and can be hard to control.

Second, by its very nature, experimental approaches are limited to realizable ideas. Future concepts, which might appear unreasonable with currently available technologies, are thus difficult to investigate. The same applies to probes. Certain effects are difficult to observe directly, e.g. the different interactions of gamma photons with matter. Conversely, effects that are unavoidable in the experiment can be excluded from simulations, e.g. Compton scattering.

Finally, experimental investigations of new detector configurations are very costly and time-consuming. For each new configuration a detector has to be build up and tested. The materials as well as the assembly of scintillation detectors are expensive and the reuse of components is often limited, e.g. if parts like the scintillators and reflectors are permanently bonded. Proper machining and gluing of scintillator materials requires special tools and experience. Therefore, even small modifications can be very costly and time-consuming.

All the above limitations clearly show the need to complement experimental work with appropriate models and simulations.

Optical simulations of scintillation detectors have a long track record and are subject to research for more than 20 years. Numerous optical simulation tools have been used for simulating scintillation detectors, e.g. DETECT2000 (Cayouette et al. 2003), Litrani (Gentit 2002), ZEMAX and Geant4/GATE (Agostinelli et al. 2003, Allison et al. 2006 / Jan et al. 2011, 2004), as well as custom written software tools. All of them are based on Monte Carlo approaches in combination with ray-tracing or particle tracking.

However, scintillation detectors are not purely optical devices, they rather are converters of gamma photons to optical photons. In most cases, Compton scattering will influence the deposition of energy within the scintillator. For example, the ratio of photoelectric to Compton interaction probability for 511 keV gamma photons in LSO is merely 52 % (Shao et al. 1996). Thus, a proper simulation model for scintillation detectors should include the interaction of gamma photons with matter.

Exactly this combination is provided by the Geant4/GATE simulation package. Geant4 is a simulation environment to simulate and track the interaction of high energy particles through matter, including gamma and optical photon processes as well. The Geant4 environment is essentially a framework of software libraries written in C++. It is thus often used in combination with GATE (Geant4 Application for Emission Tomography), which provides a more user friendly interface via an interactive console and text based script files. Geant4 as well as GATE are open-source, free-of-charge. Both are well documented in the respective user manuals and are supported by an active developer and user community.

From personal experience, there is a rather negative preconception about the reliability of optical simulations, which somehow is also reflected by the number of publications. There exist countless publications on experimental investigations, but rather few on corresponding optical simulations. In order to understand and classify the preconceptions about optical simulations, the following section will outline the main challenges of optical simulations. Subsequently, the usability of optical simulations shall be assessed by simulating the three detector configurations of section 5.2 with Geant4/GATE.

Publication	Subject of investigation
Bea et al. 1994	Simulating the light collection efficiency of roughened BGO crystals using the GEANT3 software package.
Rothfuss et al. 2004	Simulation of LSO single crystals and arrays, separated by dif- fuse reflector, using DETECT2000.
Bauer et al. 2009	Use the ZEMAX ray-tracing software for simulating the position histogram of an LSO block detector with $12 \times 12$ $2.5 \times 2.5 \times 20 \text{ mm}^3$ crystal elements, which are partially separated by a specular reflector film and air.
Bonifacio et al. 2010	Using GEANT4/GATE to simulate the light collection of LYSO crystals embedded in a white epoxy matrix.
Janecek and Moses 2010	Simulation of light collection efficiency of BGO crystals with different surface treatments using Geant4/GATE with optically measured surface properties.
Laan et al. 2010	Simulation of a monolithic $10 \times 20 \times 10 \text{ mmHg}^3$ LYSO scintillator block with diffuse reflectors on an APD array using Geant4/GATE.
Fan et al. 2012	Optical simulation of a $9 \times 9$ array of $2.1 \times 2.1 \times 10 \text{ mm}^3$ LYSO crystals, partially separated by a reflective film and coupled to four photomultiplier tubes, using Geant4/GATE.
Roncali and Cherry 2013	Simulation of light transport in scintillators based on 3D char- acterization of crystal surfaces, using a custom Monte Carlo simulation.
Roncali et al. 2014	Simulation of timing properties of phosphor-coated scintillators using custom written simulation tool.
Berg et al. 2015	Optimizing the surface structure for light transport in $3.34 \times 3.34 \times 20 \text{ mm}^3$ LYSO crystals with partially roughened surfaces for time-of-flight PET, using a custom written Monte Carlo photon tracking tool.

Table 5.2 Review of optical simulations of scintillation detectors for PET.

#### 5.4.2 Main challenges of optical simulations

Table 5.2 provides a brief overview of publications addressing the optical simulation of scintillation detectors for PET. In summary, these studies show that there is a justified interest in simulating optical photon transport in scintillation detectors and that optical simulations are feasible. However, those studies also point out a number of challenges for proper optical simulations.

One of the main issues noted by most of those studies is the difficulty to model optical surfaces accurately. In particular, roughened surfaces turned out to be troublesome, whereas polished surfaces showed good agreement with measurement data. This is mainly caused by two reasons. On the one hand, most simulation tools lack to model the micro-structure of surfaces properly. On the other hand, it is difficult to determine the respective model parameters. Both problems are mutually dependent, because model and parameters have to match. The commonly used UNIFIED model (Levin and Moisan 1996), which is also used by Geant4/GATE, models optical boundary processes by a set of probabilities for different kinds of reflection, e.g. the probability of a photon to undergo specular or diffuse reflection. A lookup table is used to specify the respective reflection probabilities in dependency of the photon energy, but the incident angle is neglected. The incident angle is merely used to calculate the reflection and refraction angles.

For each boundary event, the incident angle is calculated as the angle between the incident photon and the surface normal. By default, the surface normal of the macroscopic geometry is used. The only implemented opportunity to account for the microstructure of surfaces are micro-facets. Micro-facets model the microscopic surface normal as deviations from the macroscopic surface normal. The UNIFIED model always uses micro-facets with normally distributed surface normals, characterized by the standard deviation  $\sigma_{\alpha}$ . Microscopic height variations of the surface are entirely neglected. Thus, if the actual surface structure differs, it can not be accurately modelled by the UNIFIED model.

The other problem is how proper surface parameters can be determined from experimental data. Janecek and Moses (2008) measured the angular-dependant reflectivity of several surface treatments by using a hemispherical scintillator and scanning it with a laser beam. Unfortunately, the experimental effort is very high and up to now only a small set of parameters for BGO with different kinds of surface treatments has been published. Later on, the source code of Geant4/GATE was modified to include the results by using lookup-tables (Janecek and Moses 2010). Roncali and Cherry (2013) characterized the microscopic surface structure of LSO crystals with an atomic force microscope. The topography maps obtained were subsequently used to derive reflectance properties in the form of lookup-tables. Both approaches improved the agreement of simulation to measurement data, in particular for rough surfaces.

In summary, the problem of modelling surfaces properly is still not solved, but it is mainly an issue for roughened surfaces, whereas polished surfaces showed mostly good results.

Another issue often mentioned is simulation time, e.g. computing times of the order of weeks are reported (Bauer et al. 2009). It is inevitable, that the number of events to track is about four orders of magnitude higher than for gamma particle tracking only. This number simply originates from the scintillation yield of common scintillator materials, which is about 25 000 to 32 000 photons per MeV for L(Y)SO, each subject to multiple interactions and boundary processes. Thus, compared to non-optical simulations, the simulation time can be expected to increase by a factor of 10 000 to 100 000 for the same problem. Furthermore, more details of the detector have to be modelled, e.g. thin glue layers, reflectors and structures, which significantly increases the number of geometric objects and boundary processes. In the case of simulating gamma ray interactions, such details can often be simplified or even be neglected.

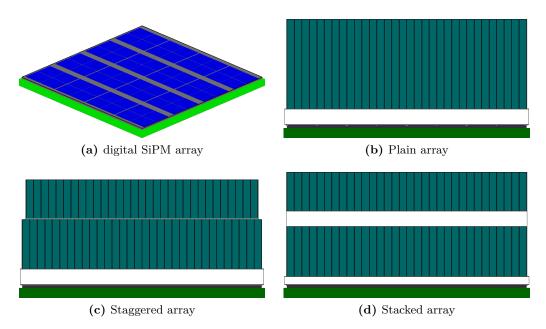


**Figure 5.12** Simulated detector geometries. (a) Digital SiPM array. Blue areas mark the sensitive areas of the detector. (b) Cross-section of plain scintillator array with lightguide and sensor tile. (c) Staggered array with offset arrays of different thickness. (d) Stacked array without offset, but with additional light guide.

### 5.4.3 Practical assessment of optical simulations

The following examples are intended to assess the usability of Geant4/GATE optical simulations for the development of pixelated scintillation detectors. For this purpose, experimental reference data is required. In section 5.2, the plain, stacked and staggered approach were experimentally investigated. Those investigations represent a typical use case and similar configurations are regular research objectives. It was therefore most convenient to rebuild and simulate those detector configurations with Geant4/GATE to compare experimental and simulated data. For this, the geometry of the digital SiPM array, the plain, the staggered and stacked scintillator array were transferred into a GATE geometry description. A graphical overview of those configurations is shown in figure 5.12. Dimensions and materials were set as described in section 5.2 for the experimental set-up.

Basically, the geometry description of a detector with optical photon transport is the same as for a detector without optical photon transport. However, for simulations including optical photon transport, special attention is required for proper volume placement. Volumes within Geant4/GATE are hierarchically ordered and must neither overlap nor exceed their parent volume. Violating this criterion will cause false simulation results and can abort simulation runs, but it also can be a silent error, i.e. the simulations runs without reporting an error, but with unpredictable results. Nevertheless, neighbouring volumes must be exactly flush, because only if they touch each other optical transitions between the two volumes can be defined. In case of high energy particles, this is less critical, because a very thin interlayer impacts high energy interactions only marginally, but for optical photon transport it is crucial.

To simplify the geometry definition, some details of the simulation model differ from the experimental configuration, in particular the reflector coverage. The basic volume of the scintillator array is a solid box, specified as reflector. In this box, an array of box volumes is defined as optical transparent glue, and each of those glue volumes contains a solid box defined as scintillator material. This simplifies the textual description and reduces the number of surface definitions. However, because of the used fabrication method, the reflector in fact is composed of multiple reflector sheets, each covered by a glue layer. Thus in the model, each crystal is optically perfectly separated from neighbouring pixels, whereas in the experiment there exists a small leakage path. However, the width of the glue gap is merely 7 µm. Compared to the crystal width of 0.9225 mm, this is less than 1 %. Furthermore, the depth of the gap is about 65 µm, which further decrease the probability of a photon to pass through the gap. Compared to the amount of light sharing caused by the light guides, the effect of light leakage through the gaps is considered to be negligible.

All surfaces are defined as *dielectric-dielectric* boundaries, with two exception: the surfaces towards the sensitive area of the digital SiPM and the reflector is defined as *dielectric-metal*. First is a prerequisite for optical photon detection within Geant4/GATE, whereas second is required to define a specular reflector within Geant4/GATE. However, defining the surface towards the reflector as dielectric-metal boundary has the side effect that no optical photon can pass this boundary. This is a principle weakness of the available surface definitions of Geant4/GATE, because in fact the used reflector foil in not totally opaque. The reflectivity of the reflector is set to 95 % at 420 nm. Photons that are not reflected are absorbed.

To reduce the number of simulated photons, the scintillation yield of the scintillator was reduced and the photon detection efficiency of the digital SiPM increased. The photon detection efficiency is set to 100%. The scintillation yield of the scintillator is set to 10000 (instead of 32000) photons per MeV to account for the photon detection efficiency and the fill factor of the digital SiPM. The intrinsic energy resolution of the scintillator is assumed to be 8.1% at 511 keV.

The surface structure of all surfaces is defined as ground with a micro-facet mean angle of  $\sigma_{\alpha} = 1.3^{\circ}$ , which was found to correspond to a mechanically polished surface.

Simulations were executed on a computer cluster running Scientific Linux 6.x with GATE V6.2, Geant4 09.05 patch 02 and CLHEP 2.1.1.0. Most nodes in the cluster are Intel Xeon X5675 processors with 3.06 GHz clock frequency. The analysis of simulation results was carried out in analogy to section 5.2, including the neighbourhood criterion.

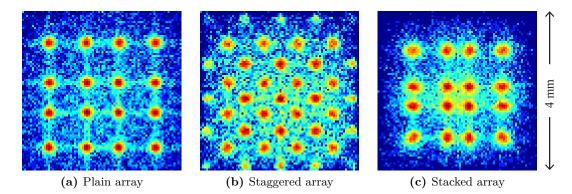


Figure 5.13 Simulated position histograms of plain, staggered and stacked scintillator array. Shown details correspond to a  $4 \times 4 \text{ mm}^2$  excerpt of the position histogram, corresponding to the area of a single digital SiPM channel.

#### Results

Figure 5.3 shows details of the resulting position histograms. The simulated position histograms basically show the same structure as the experimental ones, e.g. the number of spots and their alignment is consistent. However, there are differences in intensity and deformations, in particular for the stacked array.

In analogy to the experimental investigation, the simulated data of the stacked array was analysed for a depth-of-interaction effect. The selective irradiation of the top and bottom layer in the simulation was implemented by disabling the scintillation property the respective other layer. Figure 5.14 reveals a similar depth dependency of the light distribution as observed in the experimental data. However, the energy ratio of the centre channel to neighbour channels is about 1.3 to 1.5 times higher than in the experimental data. Thus, more light was detected by the centre channel.

The average computation time per detected gamma was 3.45 s, 4.08 s and 3.87 s for the plain, staggered and stacked array, respectively. On average 3506 gamma interactions per mm<sup>2</sup> were simulated. The simulation of each  $4 \times 4 \text{ mm}^2$  position histogram thus consumed more than two days of computation time. However, each simulation run was split into 250 jobs and submitted in parallel to the computer cluster. The actual throughput time was thus rather 15 min to 30 min per position histogram.

### 5.4.4 Discussion

The simulated position histograms reveal the same basic structure as the experimental ones, showing that the simulation environment itself is functional. Yet, there are differences between simulated and experimental data.

The intensity of spots varies and is less homogeneous for experimental data, in particular for the stacked array, which indicates a loss of sensitivity. This can be attributed to the self-triggering nature of the digital SiPM. Whereas simulated datasets are always

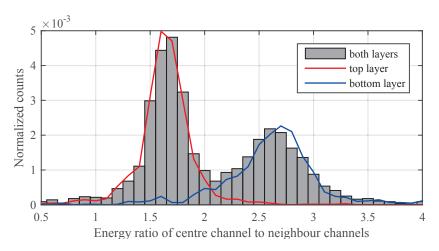


**Figure 5.14** Simulated energy ratio of centre channel to neighbour channels. Like the measurement presented in figure 5.5, the simulation data also shows a characteristic width of the light distribution for the top and bottom layer. The observed ratio is higher than the measured ratio, which can indicate that in fact the light spreads out more than in the simulation model. In contrast to the measurement, the separation of top and bottom layer events was achieved by disabling the scintillation property of the other layer for each simulation run.

complete, experimental data sets lacks of missing channels. This is in particular an issue of the stacked array, because the light distribution of the stacked array depends on the hit layer. Obviously, the chosen amount of light sharing is not optimal to trigger all channels reliably.

No particular effort was put on optimizing the optical material and surface parameters. The good agreement of the basic structure can be attributed to the fact that all optical surfaces were polished surfaces and that the shaping of the light distribution is mainly defined by the geometry of the detector assembly.

The problem of imperfect surface modelling certainly still is an issue, but it likewise affects all experimental approaches. Many detector designs thus probably rely on trial and error as well as experience, rather than on knowledge of the surface properties. The argument against using optical simulations because of inaccurate surface specifications is thus rather weak. Optical simulations at least offer an opportunity to reveal this knowledge gap and verify potential solutions.

The default installation of Geant4/GATE lacks to model a specular reflector with a certain transmission probability. The offered dielectric-metal boundary is a perfect optical barrier, which is insufficient to model the commonly used specular reflector films, because they are not perfect optical barriers. Thus, the amount of light sharing within the arrays is probably higher, which would explain the higher light ratio of the centre channel observed for the stacked array. Interestingly, comments inside the source code point out how to change the absorption into a transmission, but as absorption is required for the detection of optical photons this was not a viable option. However, in principle this could be easily incorporated into the source code of Geant4. The computational effort of optical simulations certainly is high. However, the problem can be easily split into multiple independent computation tasks, which can be executed in parallel. With reasonable sized computer clusters the throughput time of optical simulations can thus be easily reduced to less than an hour. Fortunately, there are no licence fees for Geant4/GATE, optical simulations can thus be easily scaled and transferred to available computing resources. As computing power is becoming ever more easily available and marketable, the possibilities to investigate new detector configurations by means of optical simulations expand. At the time of writing, one hour of computing time was available at less than  $0.1 \in$  per hour (e.g. Amazon EC2, \$0.075 per hour). Based on that, the costs of each of the shown simulation runs can be estimated to be less than  $10 \in$ . This is a dramatic advantage compared to an experimental setup, which easily costs 100 to 1000 times more.

Far more time consuming was the setup and configuration of the simulation model. Although GATE allows a rather user friendly interface to Geant4, the modelling of more complex geometries for optical simulations can be intricate and error-prone. In particular the accurate flush alignment via script files is error prone and difficult to debug. Furthermore, GATE provides only a sub-set of the geometric objects of Geant4 and the import of CAD models is not possible. Similar, the definition of surfaces can be cumbersome if the number of geometric objects increases. For each boundary the surface has to be defined via the script files. There is no opportunity to set a default surface and a missing surface definition does not result in an error, but in a perfectly flat dielectric-dielectric boundary.

## 5.5 Reflectorless pixelated scintillator arrays

#### 5.5.1 Introduction

Up to now, neither pixelated nor monolithic approaches are fully satisfactory. Whereas plain pixelated arrays lack measuring the depth-of-interaction, monolithic scintillators lack the intrinsic position encoding. This led to the consideration of how the advantages of both approached could be combined. In the following, a scintillator configuration, named reflectorless pixelated scintillator array, is investigated. Shown investigations are based on the previously described Geant4/GATE simulation framework.

Reflectorless pixelated scintillator arrays aim to combine the inherent two-dimensional position resolution of pixelated scintillators with the depth-of-interaction capability of monolithic scintillators, while maintaining single-sided-readout. Their basic idea is to combine individual scintillator elements in an optical transparent matrix and utilize the different refractive indices of scintillator and matrix materials to shape the lightdistribution.

There are mainly two motives for reflectorless pixelated scintillator arrays:

First, avoiding the reflector increases the sensitivity of scintillator arrays. The scintillator arrays used in this work are specified to have an inter-crystal gap of 77.5  $\mu$ m, which is composed of an 65  $\mu$ m reflective film and two glue layers. Thus, a plain array with 1 mm pitch is only about 85 % of scintillator material. This ratio is even worse for finer pitches array, e.g. 76 % for a 0.6 mm array. To compensate for the sensitivity loss, the height of the arrays would have to be increased, but increasing the height of the arrays is disadvantageous because the parallax error and construction height would increase as well. Both should be avoided, in particular for PET/MRI.

Second, removing the reflector will break up the optical barrier between crystals and thus increase light sharing. Nonetheless, because of the high refractive index of common scintillator materials, total reflections still should preserve the pixelated structure for optical photon transport. Here, the refractive index of the scintillator and matrix material plays a crucial role. The refractive index of LSO and LYSO is about 1.8, whereas the refractive index of common glues is close to 1.5. According to Snell's law, photons passing a boundary from a medium with refractive index  $n_1$  to a medium of refractive index  $n_2$  are refracted:

$$\frac{\delta_1}{\delta_2} = \frac{n_2}{n_1} \tag{5.1}$$

The critical angle for total reflection of an optical photon passing from a medium with refractive index  $n_1$  to a medium with refractive index  $n_2$  thus calculates as

$$\delta_c = \arcsin \frac{n_2}{n_1} \,. \tag{5.2}$$

In case of the transition from the L(Y)SO with a refractive index of about 1.8 to the glue layer with a refractive index of about 1.5, total reflection occurs at incident angles above 56.44°. Thus, a scintillator crystal should perform as light guide for a great portion of the light even without an additional reflector.

In the following, Geant4/GATE optical simulations are used to investigate the feasibility and potential use of such arrays for PET scintillation detectors.

### 5.5.2 Methods

The basic configuration investigated here is an array of  $32 \times 32$  cuboid scintillators with a pitch of 1 mm. Each scintillator element is  $0.993 \times 0.993 \times 20 \text{ mm}^3$ , resulting in a gap of 7 µm between adjacent scintillators. The dimensions used are adapted from a manufacture specification to which such arrays can be produced. The scintillator array is embedded in an optical clear glue matrix of dimensions  $32.1 \times 32.1 \times 20.1 \text{ mm}^3$ , wherein the bottom surface of the glue matrix is in-plane with the bottom surface of the scintillator array. The centre of the bottom surface is aligned to the point of origin, the z-axis pointing to the top of the scintillators.

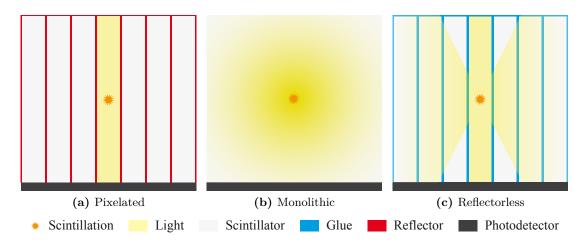


**Figure 5.15** Basic operating principle of (a) pixelated, (b) monolithic and (c) reflectorless scintillator configuration. The reflectorless approach combines the intrinsic two-dimensional spatial resolution with the light-sharing information of the monolithic approach.

The scintillator properties were adapted from the previous section. The refractive index of the scintillator was set to 1.82 and the refractive index of the glue matrix was set to 1.5. The scintillation yield of the scintillator was set to 26 000 photon per MeV and an intrinsic energy resolution of 9%. To make the investigation independent of a specific photo detector geometry, the bottom surface of each scintillator element is defined as perfect photodetector. Thus a grid of  $32 \times 32$  photodetectors covers the bottom surface of the array. The surface between the glue matrix and the surrounding is defined as perfect absorber to exclude the effect of external reflectors. The surface between the scintillators and the glue matrix is defined as *dielectric-dielectric* boundary with mechanically polished surface with a micro-facet distribution of  $\sigma_{\alpha} = 1.3^{\circ}$  and specular lobe reflection only.

Instead of using a 511 keV gamma ray source, an electron source with a kinetic energy of 511 keV was placed within the scintillator. Thus, the depth-of-interaction is precisely known and adjustable. Furthermore, scattering of gammas is eliminated and all energy is deposited at one well known position. The source was successively placed at five zpositions ranging from 2 mm to 18 mm in 4 mm steps, with the origin of z on the bottom side of the scintillator. The x- and y-position was constant 0.5 mm, respectively. By default, 1000 events per position were simulated.

The reflectorless scintillator array is based on total reflections at the scintillator to glue border and vice versa, the optical properties of this border are thus of main interest to adjust the properties of such arrays. In particular the refractive index of the glue and the surface structure are the main parameters to modify the resulting light distribution. Starting from the basic configuration, two variations were investigated. First, the influence of the refractive index of the glue was investigated by increasing its refractive index in two steps to 1.6 and 1.7, respectively. Second, the surfaces between the scintillators and the optical matrix was successively changed to an ideal flat and a roughened surface. For the *ideal* surface  $\sigma_{\alpha}$  was set to zero, resulting in a perfectly planar surface. For the roughened surface the angular distribution of the micro-facets was increased to 12°. The value was adopted from Janecek and Moses 2010.

For comparison, a monolithic scintillator configuration is simulated. Therefore, the basic configuration is modified by increasing the scintillator width and depth to 1 mm. Thus, the scintillator array is treated as an optical homogeneous medium by the simulation software, effectively representing a  $32 \times 32 \times 20 \text{ mm}^3$  monolithic scintillator, embedded in a glue layer. To avoid the influence of boundary reflections, the surface between the scintillator with the glue layer is surrounded by a perfect optical absorber.

To characterize the shape of the light distribution, the *light spread* s is defined as

$$s = \sum_{i=0}^{N} p_i \sqrt{(x_i - x_m)^2 + (y_i - y_m)^2},$$
(5.3)

where *i* is the index of the respective detector element,  $x_i$  and  $y_i$  the respective centre position of the detector element and  $x_m$  and  $y_m$  the centre position of the detector element with the highest photon count.

### 5.5.3 Results

Figure 5.16 shows the simulated light distribution of the reflectorless scintillator arrays with different kinds of glue and an exemplary light distribution of a monolithic array. Shown data is normalized by the number of detected photons for each event. The shape of the light-distribution changes with interaction depth and the effect increases with the refractive index of the glue. Though, most light is focused on the centre crystal and the crossing row and column. The x- and y-position of the scintillation can thus be readily obtained. In case of the monolithic scintillator, this is hardly possible.

The corresponding measures of the light spread and mean sum of detected photons is shown in figure 5.17. They confirm the visual impression of increased light spread for higher refractive glues. However, the observed spread does not increase monotonically with the interaction depth. This can be explained by the limited size of the scintillator array and photodetector array. Below the critical angle, optical photons escapes the centre crystal and hit the side surfaces of the array. As those photons are not detected, they can not contribute to the light spread. In consequence, this effect is more pronounced and appears earlier for lower refractive indexes of the glue. Monolithic detector are not affected by this effect and thus the light spread of the monolithic scintillator increases as expected monotonously.

The other opportunity to modify the light distribution is to modify the surface structure of the crystals. Figure 5.18 shows the influence of the surface roughness on the light distribution. The results of an ideal and a polished surface are almost the same.

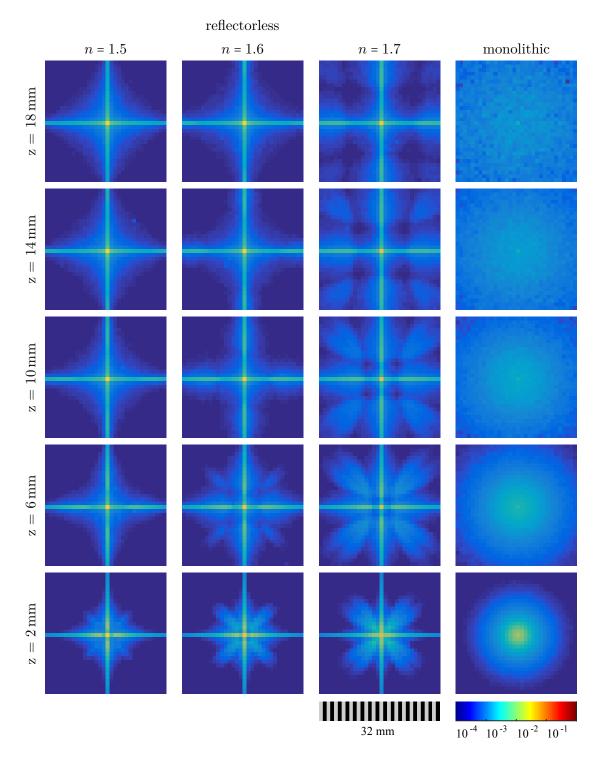


**Figure 5.16** Normalized light distribution of reflectorless arrays with different refractive indices and a monolithic scintillator block. The refractive index of the glue layer directly influenced the amount and shape of the light distribution. Although there is no reflector between the crystals, the light is focused on the centre crystal and the crossing row and column crystals. In contrast to the monolithic scintillator, the x- and y-position of the scintillation origin is thus clearly observable.

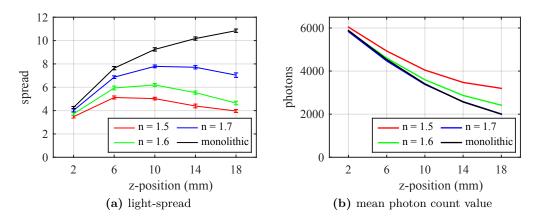


**Figure 5.17** Light spread and mean photon count values at different refractive indices. (a) The light-spread, here utilized as indicator of a depth-of-interaction effect, increases with the refractive index of the glue. The closer the refractive index of the glue is to the refractive index of the scintillator material, the closer the resulting light-distribution becomes to the light distribution of a monolithic scintillator block. (b) Similar, the photon count value get closer to that of a monolithic detector. Error bars indicate the FWHM deviated from the empirical standard deviation of the calculated light spread.

Thus, the approach to improve the polishing of the crystal surfaces will not improve the results. Quite different, roughening the surface results in a clearly more diffuse spread of the light.

The visual impression is confirmed by the calculated light spread, as shown in figure 5.19. In the case of the roughened surface, the light spread increases monotonically with the interaction depth. Thus, the roughened surface provides a better indicator for the interaction depth than a polished surface. Additionally, the mean sum of detected photons is higher than for the ideal and polished surface treatments.

### 5.5.4 Discussion

Due to its design principle, reflectorless scintillator arrays provide a higher gamma sensitivity than conventional pixelated scintillator arrays. This is advantageous, in particular for very fine pitched arrays, as they are required for very high-resolution PET scanners. In addition, pixelated scintillator arrays also have a fabrication advantage, because the glue sticks better to scintillators than reflectors and only half the number of gluing layers are required.

Simulation results have shown that depth-of-interaction information can be obtained from reflectorless scintillator arrays. For polished crystals, the effect depends on the ratio of the refractive indices of the scintillator and the optical matrix and showed to increase with the refractive index of the glue. However, the effect is weaker than with a monolithic scintillator, thus it is not assured if this effect can be practically used with current photodetectors. Furthermore, it is questionable if such highly refractive glues are realizable and feasible for the fabrication of fine pixelated scintillator arrays. Most

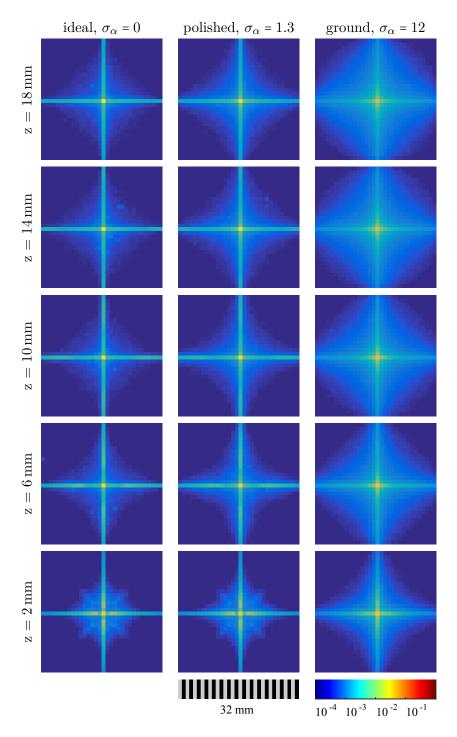


**Figure 5.18** Light distribution of reflectorless scintillator array with different surface treatments. The refractive index of the glue was kept constant at 1.5. The light-spread increases with the roughness of the crystal surface.

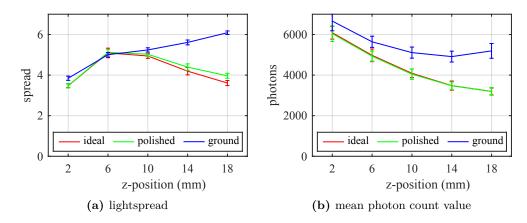


Figure 5.19 Light spread and mean photon count values at different surface treatments. (a) Whereas the difference between an ideal and a polished surface is rather small, the roughened surface results in a higher and continuous increase of the light spread with interaction-depth. (b) The mean photon sum of the ideal and the polished is almost the same, but the roughened surface increase the number of detected photons. Error bars indicate the FWHM deviated from the empirical standard deviation of the calculated light spread.

epoxy or acrylic based glues have a refractive index of about 1.5. High refractive index glues are subject to research, e.g. glues loaded with titanium dioxide (Wu et al. 2007).

The other opportunity to adjust the light sharing is to roughen the surface of the crystals. Thus, reflection and refraction become more diffuse. A positive side effect of the roughened surface is the increased light yield. The light yield improving effect of roughened surfaces is basically known, e.g. Berg et al. 2015, and can be explained by the fact that photons initially travelling into the wrong direction get a higher probability to be reflected towards the photodetector. However, the modelling of rough surfaces is known to be inaccurate. The results presented here can thus be used only as an indicator. Perfectly polished surfaces are likely to be less suited for reflectorless scintillator arrays with depth-of-interaction encoding, but roughened surfaces potentially can provide this.

The selected measure of light-spread is an unoptimized indicator of the interaction depth. Better results could probably be achieved with pattern matching algorithms, as they are, e.g., used for monolithic detectors. Here it is chosen because of its simplicity and straight forward implementation.

## 5.6 Conclusion

Although the depth-of-interaction problem is subject to research for a long time, no fully satisfactory solution has been found so far. Same applies to the here presented approaches.

The staggered approach showed good results and a further layer increase and pitch decrease appears possible. With today's experience with the digital SiPM, this ap-

proach seems to be very feasibly to be implemented on system level. The stacked approach with an additional light guide showed that this approach is basically feasible and provided an interesting comparison with simulation data, but it seems to be difficult to extend this approach to further layers. Furthermore, the additional light guide costs construction space, which makes altogether the stacked approach less favourable.

The experimental investigation of depth-of-interaction effects in scintillation detectors is costly and troublesome. The common approach to irradiate scintillator laterally represents a very ideal case. In practice, most gamma photons will hit the scintillator more frontally. Resulting Compton scattering might thus deteriorate the actual obtainable depth resolution. However, experimentally, Compton scattering is unavoidable, but can be avoided in simulations.

One of the main issues of the optical design of scintillation detectors remain the difficulties to characterize optical surface parameters. This affects both, experimental and simulation work, although it might be more prominent in simulation work, because parameters have to be stated explicitly and deviations from measurement results appear more obvious. A particular problem of the optical simulations with Geant4/GATE is that the model used itself is not accurate, i.e. the used parameters are unable to reflect the properties of real surfaces.

Both problems could be solved by using optical measurement data and lookup tables instead of model based parameters However, the experimental effort to obtain the required data is high and it is costly, thus up to now only very limited data sets are available. The use of measuring the mechanical microstructure of surfaces with an atomic force microscope seems to be easier to realize. However, the translation of surface structures to actual optical properties is not self-evident, e.g. it still assumes a closed surface without undercuts and sub-surface cracks.

Furthermore, Geant4/GATE lacks to model a specular reflector with partial transmission. Such a surface is of high interest to model the behaviour of commonly used specular reflector films, which are very good reflectors, but not entirely opaque. Part of the observed deviations between measurement and simulation results might be related to this. In principle, this should be easily implementable to somebody who is familiar with the source code of Geant4/GATE.

The short-comes of optical simulations can be also seen as a chance to better understand the optical processes. For example, the influence of a partial transparency of the reflector could be easily assessed with simulations. Experimentally, the transparency is difficult to control or to eliminate. Thus, the short-comes of optical simulations can at least help to identify false assumptions and help to understand the optical processes in scintillators better.

The computation time of optical simulations in relation to the effort required for experimental work, preparation and extraction of simulation parameters appears less significant with the availability of high performance computer cluster. Thus, further work should focus on improving the simulation model and collection of proper surface and material properties, rather than focusing on improving simulation runtime.

# Chapter 6

# Conclusion

The simultaneous integration of PET and MRI promises to combine superior anatomical and functional information into a single examination, but poses a number of engineering challenges. Simultaneous PET/MRI was basically made possible by the advent of solid-state photodetectors. Yet, a successful integration of PET and MRI requires much more than the replacement of photomultiplier tubes. Choosing the right photodetector technology, minimizing cross-modality interference and making the best use of the confined construction space inside an MRI scanner remains crucial to compromise neither image quality nor usability.

This thesis set out to asses three specific engineering aspects of simultaneous PET/MRI. All of them are related to the development of the Hyperion  $II^D$  PET/MRI insert, the world's first digital SiPM based PET/MRI system. First of all, an MRI-compatible digital SiPM detector stack has been developed to evaluate the feasibility of the digital SiPM for simultaneous PET/MRI. Second, the minimization of eddy currents induced in RF shields has been addressed by the development of a carbon fibre composite based housing, with a particular focus on the quantification of the RF shielding properties of carbon fibre composites. Third, the depth-of-interaction problem of scintillation detectors has been addressed by different approaches to improve the optical design of pixelated scintillation detectors experimentally as well as by using optical simulations.

## 6.1 Empirical findings

The digital SiPM showed to be very well suited for simultaneous PET/MRI. Its direct digitization and high functional integration not only facilitates a very compact detector design, but it also makes the digital SiPM very resistant to external electromagnetic distortions. Within this thesis, no evidence was found that the digital SiPM itself is affected by the MRI environment. All observed MRI interference effects could be attributed to the detector infrastructure. The detector stack presented in chapter 3 was developed and optimized with a view to an unrestricted simultaneous operation of PET and MRI. As shown, if the detector infrastructure is properly designed, the full

performance of the digital SiPM, including its time-of-flight capabilities, can be utilized for simultaneous PET/MRI.

Most severe interference effects on PET were caused by MRI gradient induced supply voltage variations, which initially degraded energy and time measurements. Although this issue could be identified and solved by redesigning circuit boards, the impact of those voltage variations on the switching characteristic of the FPGA core logic is important to note, because other digital devices might likewise be affected by the MRI system, although actual effect could be more concealed, i.e. increased jitter might deteriorate the bit error rates of high speed communication links. Gradient induced supply voltage variations should thus be carefully considered for further developments. Likewise, the effect of static magnetic fields on voltage regulators should be carefully considered for further developments, because operating voltages might deviate from their specified values. Although the root cause of the observed voltage variations could not be fully clarified, they are likely to be caused by the Hall effect and thus might increase at higher field strengths.

The avoidance of  $B_0$  distortions and the minimization of RF interference are still two of the main challenges for the design of MRI-compatible electronic devices. The basic problem remains that many electronic components contain nickel or iron in their surface finish or lead frames. In particular, this applies to multi-layer chip capacitors, which are required for proper RF decoupling, but whose electrodes are commonly made of nickel. This results in a design conflict between minimizing RF interference and  $B_0$ distortions. Available dedicated non-magnetic capacitors suffer from low capacitance density and thus result in larger case sizes, more construction space and higher lead inductance. This situation is unlikely to change, as long as the overall demand for non-magnetic components remains low.

Up to now, most PET/MRI systems incorporate copper shields to minimize RF interference. However, copper shields can be troublesome for PET/MRI, because the high conductivity of copper makes them susceptible to eddy currents. In chapter 4, it is analytically shown that lower conductivity but thicker materials provide a higher RF shielding efficiency to sheet conductance ratio. The conductivity of carbon fibre composites is about 1000 times lower than the conductivity of copper. Reasonably thick carbon fibre composites in the order of 1 mm thus combine good RF shielding efficiency with low sheet conductance.

In contrast to copper based RF shields, no particular structuring of the shield is required to reduce eddy currents. The RF shielding efficiency and sheet conductance of carbon fibre composites has been experimentally verified and modelled within the frequency range of commonly used MRI systems. Within the analysis range, experimental and model data are in excellent agreement, although the experimental quantification of shielding efficiencies at MRI frequencies remains difficult, because of the long wavelength and the high dynamic range required. It are not only the electromagnetic properties that make carbon fibre composites beneficial for PET/MRI. It is rather the combination of electromagnetic properties with mechanical stiffness, high gamma transparency and optical opaqueness that makes carbon fibre composites attractive for PET/MRI. The combination of those parameters was used to develop the housing concept for the Hyperion II<sup>D</sup> system. It allows a modular design of the detector and the RF shielding can be quickly replaced for testing. Furthermore, the fabrication method shown is very versatile and can be easily adapted to other scanner geometries and materials compositions.

With rising resolution and sensitivity demands, the parallax error becomes an increasingly important issue for the design of PET detectors. In particular for PET/MRI systems, where the PET detector is placed closer to the scanned object, methods to measure the depth-of-interaction are of special interest. Although there exist various approaches to determine the depth-of-interaction, up to now no fully satisfactory approach has been found.

The approaches and methods presented in chapter 5 focus on pixelated scintillator arrays with single sided readout, as they are in line with the concept of the Hyperion  $II^{D}$  system. It is experimentally shown, that a two layer staggered approach with 1 mm crystal pitch LYSO arrays and digital SiPM single sided readout is feasible. In addition, a novel staggered approach that utilizes the shape of the light distribution rather than the position histogram to distinguish crystal layers is presented. Although the presented stacked approach might be very susceptible to sensitivity variations because of missing channels, it demonstrates that the shape of the light distribution of pixelated scintillators contains more information than the position histogram reveals.

Utilizing the cell programming feature of the digital SiPM, a novel method to measure the light distribution of individual crystals within a scintillator array with sub-channel resolution has been developed. It clearly reveals, that the shape of the light distribution contains more detail than can be resolved with a 4 mm channel pitch photodetector. In contrast to an often made assumption, the light distribution within a channel is inhomogeneous, which, for example, directly affects the actual trigger probability of the digital SiPM, but it might also impact methods for saturation correction. Furthermore, significant parts of the light distribution are lost because of insensitive areas between the channels.

Additionally, the experimental investigation of depth-of-interaction scintillation detectors shows a number of practical issues, e.g. the actual gamma interaction positions can be hardly determined, Compton scattering is inevitable and experiments often are costly and time consuming. Optical simulations can help to overcome these issue and accelerate the development of new detector concepts. In particular, the Geant4/GATE framework is very well suited for the simulation of scintillation detectors, because it includes the transport of optical photons as well as gamma photons. Although the models and parameters used still have imperfections, the basic results of the experimental investigation of the plain, stacked as well as the staggered configuration could be reproduced. Because of the large number of tracked photons and interactions, the computational demands for optical simulations are still high, but as the problem can be very well split up into parallel tasks and computing power is becoming cheaper and ever more easily availably this appears to be less of an issue.

Based on optical simulations, scintillator arrays without inter-crystal reflectors are proposed. They might offer a solution for the extraction of continuous depth-ofinteraction information, based on the shape of the light distribution, but still provide the ability to identify the crystal positions from common measurement data. As the operating principle is based mainly on total reflections, the refractive index of the materials used and the surface structures are key parameters for this configuration. Furthermore, reflectorless scintillator arrays increase the sensitivity and simplify the fabrication process and thus might be in particular beneficial for very fine pitched scintillator arrays.

### 6.2 Further research and development prospectives

One of the main issues for the system integration of the digital SiPM was the cooling of the detector. Although the digital SiPM in principle is less sensitive to temperature variations, its high functional integration might be a disadvantage for cooling, because it places additional logic elements and thus power consumption next to the photodiodes. Moreover, the power consumption and heat load depends on activity. Thus, part of the temperature insensitivity of the digital SiPM is harmed and a reliable cooling system is required. A digital SiPM with less power consumption and lower cooling requirements would therefore be highly desirable.

As shown in chapter 5, the light distribution of pixelated scintillation detectors with light sharing is much finer shaped than the currently available photodetector pitch. A finer channel pitch than 4 mm would thus be desirable for high-resolution preclinical scanners, but also for future clinical systems with one-to-one coupling. In this context, also a combination of the single SPAD readout principle of the digital SiPM with an intrinsic position calculation method, as for example used in position sensitive photodetectors, would be very interesting.

The current implementation of the digital SiPM measures only one integral photon count value. To enhance the application range of the digital SiPM for alternative depth-of-interaction methods, information about the temporal distribution of incident photons can contain valuable information, e.g. to implement phoswich detectors. This could, for example, be achieved with multiple integration windows.

The concept of using a detector stack composed of multiple circuit boards that connect to a common readout board certainly simplified the development and investigation of interference effects. However, for further integration and to make best use of the high functional integration of the digital SiPM in terms of construction space, at least the functionality of the interface board and the SPU should be combined to reduce the overall height of the detector. A total height of less than 10 mm for the detector electronics, including the cooling, would be reasonable.

Although all these issues might be technically at least partially realizable, their actual implementation requires further research and investments. Here, the high functional integration of the digital SiPM might turn out to be disadvantageous, because even small modifications require a full production run and are thus costly. Furthermore, the digital SiPM is covered by multiple patents and thus until now commercially only available from a single supplier.

Because of the lack of non-magnetic components, reasonably MRI-compatible electronic designs should anticipate a certain amount of ferromagnetic components. In particular, the targeted use of a few ferromagnetic components might be even beneficial to compensate diamagnetic distortions caused by the scintillators. Although a precise match might be rather complex to implement because of unspecified magnetic properties and ferromagnetic saturation, future PET/MRI developments could potentially gain from balancing magnetic properties rather than focusing on avoiding ferromagnetic materials.

The minimization of RF interference relies on proper electronic design as well as proper RF shielding. Carbon fibre composites show a number of advantages for PET/MRI, but their application is not free of pitfalls, e.g. making reliable electrical contact to it and pinholes that may cause optical leakage. Methods to improve the electrical contact by surface treatments, eventually with conductive coatings or using conductive polymers are thus of high interest.

The concept of the reflectorless scintillator array requires experimental verification. In addition, the concept could be extended to reflectorless stacked or staggered configurations and thus combine multiple light sharing mechanisms to improve the depth encoding. Furthermore, the impact of the outer reflector has to be included, i.e. commonly a high reflective material instead of a black coating is preferred to increase the light yield, but will cause additional reflections and modifies the resulting light distribution. In this context, also the required number of photodetector channels and the confinement of the light spread to small areas should be investigated, to optimize the required photosensitive area and related dead time.

## 6.3 Outlook

During the duration of this thesis, two commercial human size simultaneous PET/MRI systems have been presented: in 2010 Siemens Healthcare presented the APD based Biograph mMR and in 2014 GE Healthcare presented the SiPM based Signa PET/MR. Simultaneous PET/MRI thus basically became available for clinical practice. With the

presented state of knowledge, there is much evidence that human size simultaneous PET/MRI systems are also realizable with the digital SiPM, probably even with better performance.

However, the development and the operation of simultaneous PET/MRI systems remains expensive. Whether PET/MRI will establish or not thus strongly depends on its future applications and the realizable benefits for patients, clinicians and healthcare providers. In order to answer this question properly, it will require more research and experience on the application side. It thus remains exciting to see how simultaneous PET/MRI will develop, but the technical foundation for future PET/MRI systems is already laid.

# Bibliography

- Agostinelli, S. et al. (2003). 'Geant4—a simulation toolkit'. In: Nuclear Instruments and Methods in Physics Research Section A: Accelerators, Spectrometers, Detectors and Associated Equipment 506.3, pp. 250–303. DOI: 10.1016/S0168-9002(03)01368-8.
- Allison, J. et al. (2006). 'Geant4 developments and applications'. In: *IEEE Transactions on Nuclear Science* 53.1, pp. 270–278. DOI: 10.1109/TNS.2006.869826.
- ASTM D4935-10 (2010). Standard Test Method for Measuring the Electromagnetic Shielding Effectiveness of Planar Materials.
- Badic, M. and M.-J. Marinescu (2002). 'The failure of coaxial TEM cells ASTM standards methods in H.F. range'. In: *IEEE International Symposium on Electromagnetic Compatibility*. Vol. 1. 2. IEEE, pp. 29–34. DOI: 10.1109/ISEMC.2002.1032442.
- Bailey, D. L., D. W. Townsend, P. E. Valk, and M. N. Maisey (2005). Positron Emission Tomography: Basic Sciences. Springer London.
- Bauer, F., J. Corbeil, M. Schmand, and D. Henseler (2009). 'Measurements and Ray-Tracing Simulations of Light Spread in LSO Crystals'. In: Nuclear Science, IEEE Transactions on 56.5, pp. 2566–2573. DOI: 10.1109/TNS.2009.2030411.
- Bea, J., A. Gadea, L. Garcia-Raffi, J. Rico, B. Rubio, and J. Tain (1994). 'Simulation of light collection in scintillators with rough surfaces'. In: Nuclear Instruments and Methods in Physics Research Section A: Accelerators, Spectrometers, Detectors and Associated Equipment 350.1-2, pp. 184–191. DOI: 10.1016/0168-9002(94)91162-2.
- Berg, E., E. Roncali, and S. R. Cherry (2015). 'Optimizing light transport in scintillation crystals for time-of-flight PET: an experimental and optical Monte Carlo simulation study'. In: *Biomedical Optics Express* 6.6, pp. 2220–2230. DOI: 10.1364/ BOE.6.002220.
- Beyer, T. and D. W. Townsend (2006). 'Putting 'clear' into nuclear medicine: a decade of PET/CT development.' In: European journal of nuclear medicine and molecular imaging 33.8, pp. 857–61. DOI: 10.1007/s00259-006-0137-z.
- Bloch, F. (1946). 'Nuclear induction'. In: *Physical Review* 70.7-8, pp. 460-474. DOI: 10.1103/PhysRev.70.460.
- Bonifacio, D. A. B., N. Belcari, S. Moehrs, M. Moralles, V. Rosso, S. Vecchio, and A. Del Guerra (2010). 'A Time Efficient Optical Model for GATE Simulation of a LYSO Scintillation Matrix Used in PET Applications'. In: *IEEE Transactions on Nuclear Science* 57.5, pp. 2483–2489. DOI: 10.1109/TNS.2010.2062536.
- Borghi, G., V. Tabacchini, S. Seifert, and D. R. Schaart (2015). 'Experimental Validation of an Efficient Fan-Beam Calibration Procedure for k-Nearest Neighbor Position

Estimation in Monolithic Scintillator Detectors'. In: *IEEE Transactions on Nuclear Science* 62.1, pp. 57–67. DOI: 10.1109/TNS.2014.2375557.

- Brown, M. A. and R. C. Semelka (2010). MRI: Basic Principles and Applications. 4th. Wiley-Blackwell.
- Brownell, G. and W. Sweet (1953). 'Localization of brain tumors with positron emitters'. In: *Nucleonics* 11, pp. 40–45. DOI: 10.1001/jama.1955.02950310009002.
- Brunner, S., L. Gruber, J. Marton, K. Suzuki, and A. Hirtl (2013). 'New approaches for improvement of TOF-PET'. In: Nuclear Instruments and Methods in Physics Research Section A: Accelerators, Spectrometers, Detectors and Associated Equipment, pp. 3–6. DOI: 10.1016/j.nima.2013.05.028.
- Buck, A. K., K. Herrmann, T. Stargardt, T. Dechow, B. J. Krause, and J. Schreyögg (2010). 'Economic evaluation of PET and PET/CT in oncology: evidence and methodologic approaches.' In: *Journal of nuclear medicine technology* 38.1, pp. 6–17. DOI: 10.2967/jnumed.108.059584.
- Budinger, T. F. (1983). 'Time-of-Flight Positron Emission Tomography: Status Relative to Conventional PET'. In: Journal of Nuclear Medicine 24.1, pp. 73–78.
- Burger, C., G. Goerres, S. Schoenes, A. Buck, A. Lonn, and G. Von Schulthess (2002).
  'PET attenuation coefficients from CT images: Experimental evaluation of the transformation of CT into PET 511-keV attenuation coefficients'. In: *European Journal of Nuclear Medicine* 29.7, pp. 922–927. DOI: 10.1007/s00259-002-0796-3.
- Carlson, J. W. (1994). Apparatus and method for shielding MRI RF antennae from the effect of surrounding objects.
- Catana, C., Y. Wu, M. S. Judenhofer, J. Qi, B. J. Pichler, and S. R. Cherry (2006). 'Simultaneous acquisition of multislice PET and MR images: initial results with a MR-compatible PET scanner'. In: *Journal of Nuclear Medicine* 47.12, pp. 1968–1976.
- Catrysse, J., M. Delesie, and W. Steenbakkers (1992). 'The influence of the test fixture on shielding effectiveness measurements'. In: *IEEE Transactions on Electromagnetic Compatibility* 34.3, pp. 348–351. DOI: 10.1109/15.155853.
- Cayouette, F., D. Laurendeau, and C. Moisan (2003). 'DETECT2000: an improved Monte-Carlo simulator for the computer aided design of photon sensing devices'. In: *Proc. SPIE 4833, Applications of Photonic Technology 5*, pp. 69–76. DOI: 10.1117/ 12.474315.
- Chaudhari, A. J., A. a. Joshi, Y. Wu, R. M. Leahy, S. R. Cherry, and R. D. Badawi (2009). 'Spatial Distortion Correction and Crystal Identification for MRI-Compatible Position-Sensitive Avalanche Photodiode-Based PET Scanners'. In: *IEEE Transactions on Nuclear Science* 56.3, pp. 549–556. DOI: 10.1109/TNS.2009.2018841.
- Chepel, V. Y. (1993). 'A new liquid xenon scintillation detector for positron emission tomography'. In: Nuclear Tracks and Radiation Measurements 21.1, pp. 47–51. DOI: 10.1016/1359-0189(93)90044-A.

- Conti, M. (2011). 'Focus on time-of-flight PET: the benefits of improved time resolution'. In: European Journal of Nuclear Medicine and Molecular Imaging 38.6, pp. 1147–1157. DOI: 10.1007/s00259-010-1711-y.
- Cosmus, T. C. and M. Parizh (2011). 'Advances in Whole-Body MRI Magnets'. In: *IEEE Transactions on Applied Superconductivity* 21.3, pp. 2104–2109. DOI: 10.1109/ TASC.2010.2084981.
- Cumalat, J., H. Cheung, J. Hassed, B. Smith, and A. Bross (1990). 'Effects of magnetic fields on the light yield of scintillators'. In: Nuclear Instruments and Methods in Physics Research Section A: Accelerators, Spectrometers, Detectors and Associated Equipment 293.3, pp. 606–614. DOI: 10.1016/0168-9002(90)90331-Y.
- Degenhardt, C., G. Prescher, T. Frach, A. Thon, R. de Gruyter, A. Schmitz, and R. Ballizany (2009). 'The digital Silicon Photomultiplier - A novel sensor for the detection of scintillation light'. In: *IEEE Nuclear Science Symposium Conference Record.* IEEE, pp. 2383–2386. DOI: 10.1109/NSSMIC.2009.5402190.
- Degenhardt, C., B. Zwaans, T. Frach, and R. De Gruyter (2010). 'Arrays of digital silicon photomultipliers - Intrinsic performance and application to scintillator readout'. In: *IEEE Nuclear Science Symposium Conference Record*, pp. 1954–1956. DOI: 10.1109/NSSMIC.2010.5874115.
- Delso, G., S. Furst, B. Jakoby, R. Ladebeck, C. Ganter, S. G. Nekolla, M. Schwaiger, and S. I. Ziegler (2011). 'Performance Measurements of the Siemens mMR Integrated Whole-Body PET/MR Scanner'. In: *Journal of Nuclear Medicine* 52.12, pp. 1914– 1922. DOI: 10.2967/jnumed.111.092726.
- Du, H., Y. Yang, J. Glodo, Y. Wu, K. Shah, and S. R. Cherry (2009). 'Continuous depthof-interaction encoding using phosphor-coated scintillators'. In: *Physics in Medicine* and Biology 54.6, pp. 1757–1771. DOI: 10.1088/0031-9155/54/6/023.
- Dueppenbecker, P. M., J. Wehner, W. Renz, S. Lodomez, D. Truhn, P. K. Marsden, and V. Schulz (2012a). 'Gradient transparent RF housing for simultaneous PET/MRI using carbon fiber composites'. In: *IEEE Nuclear Science Symposium and Medical Imaging Conference*. IEEE, pp. 3478–3480. DOI: 10.1109/NSSMIC.2012.6551793.
- Dueppenbecker, P. M., B. Weissler, P. Gebhardt, D. Schug, J. Wehner, P. K. Marsden, and V. Schulz (2016). 'Development of an MRI-compatible digital SiPM detector stack for simultaneous PET/MRI'. In: *Biomedical Physics & Engineering Express* 2.1, p. 015010. DOI: 10.1088/2057-1976/2/1/015010.
- Dueppenbecker, P. M., R. Haagen, S. Lodomez, P. K. Marsden, and V. Schulz (2011a). 'A method for measuring the sub-pixel light distribution of scintillation detectors with digital SiPMs'. In: *IEEE Nuclear Science Symposium and Medical Imaging Conference*. IEEE, pp. 2301–2302. DOI: 10.1109/NSSMIC.2011.6153866.
- Dueppenbecker, P. M., S. Lodomez, R. Haagen, P. K. Marsden, and V. Schulz (2011b).'Investigation of a sub-millimeter resolution PET detector with depth of interaction encoding using digital SiPM single sided readout'. In: *IEEE Nuclear Science Sympo-*

*sium and Medical Imaging Conference*. IEEE, pp. 2252–2253. DOI: 10.1109/NSSMIC. 2011.6152490.

- Dueppenbecker, P. M., B. Weissler, P. Gebhardt, D. Schug, J. Wehner, P. K. Marsden, and V. Schulz (2012b). 'Development of an MRI compatible digital SiPM based PET detector stack for simultaneous preclinical PET/MRI'. In: *IEEE Nuclear Science Symposium and Medical Imaging Conference*, pp. 3481–3483. DOI: 10.1109/NSSMIC. 2012.6551794.
- España, S., K. Deprez, R. Van Holen, and S. Vandenberghe (2013). 'Fast calibration of SPECT monolithic scintillation detectors using un-collimated sources'. In: *Physics in Medicine and Biology* 58.14, pp. 4807–4825. DOI: 10.1088/0031-9155/58/14/4807.
- España, S., R. Marcinkowski, V. Keereman, S. Vandenberghe, and R. Van Holen (2014).
  'DigiPET: sub-millimeter spatial resolution small-animal PET imaging using thin monolithic scintillators.' In: *Physics in Medicine and Biology* 59.13, pp. 3405–3420. DOI: 10.1088/0031-9155/59/13/3405.
- Fan, P., J. Chen, Q. Wei, T. Xu, Y. Xia, S. Wang, Y. Liu, and T. Ma (2012). 'Optical simulation of a 9×9 LYSO block detector with PQS technology using GATE'.
  In: *IEEE Nuclear Science Symposium Conference and Mecial Imaging Conference*, pp. 2590–2593. DOI: 10.1109/NSSMIC.2012.6551592.
- Finlay, C. C. et al. (2010). 'International Geomagnetic Reference Field: the eleventh generation'. In: *Geophysical Journal International* 183.3, pp. 1216–1230. DOI: 10. 1111/j.1365-246X.2010.04804.x.
- Fischer, P. and C. Piemonte (2013). 'Interpolating silicon photomultipliers'. In: Nuclear Instruments and Methods in Physics Research Section A: Accelerators, Spectrometers, Detectors and Associated Equipment 718, pp. 320–322. DOI: 10.1016/j.nima. 2012.10.120.
- Frach, T., G. Prescher, C. Degenhardt, R. De Gruyter, A. Schmitz, and R. Ballizany (2009). 'The digital silicon photomultiplier - Principle of operation and intrinsic detector performance'. In: *IEEE Nuclear Science Symposium Conference Record* (NSS/MIC), pp. 1959–1965. DOI: 10.1109/NSSMIC.2009.5402143.
- Frach, T., G. Prescher, C. Degenhardt, and B. Zwaans (2010). 'The digital silicon photomultiplier - System architecture and performance evaluation'. In: *IEEE Nuclear Science Symposium Conference Record (NSS/MIC)*, pp. 1722–1727. DOI: 10.1109/ NSSMIC.2010.5874069.
- Garlick, P. B., P. K. Marsden, A. C. Cave, H. G. Parkes, R. Slates, Y. Shao, R. W. Silverman, and S. R. Cherry (1997). 'PET and NMR dual acquisition (PANDA): Applications to isolated, perfused rat hearts'. In: *NMR in Biomedicine* 10.3, pp. 138–142. DOI: 10.1002/(SICI)1099-1492(199705)10:3<138::AID-NBM474>3.0.CO;2-H.
- Gebhardt, P., B. Weissler, M. Zinke, F. Kiessling, P. K. Marsden, and V. Schulz (2012). 'FPGA-based singles and coincidences processing pipeline for integrated dig-

ital PET/MR detectors'. In: *IEEE Nuclear Science Symposium and Medical Imaging Conference*. IEEE, pp. 2479–2482. DOI: 10.1109/NSSMIC.2012.6551565.

- Gentit, F. X. (2002). 'Litrani: A general purpose Monte-Carlo program simulating light propagation in isotropic or anisotropic media'. In: Nuclear Instruments and Methods in Physics Research, Section A: Accelerators, Spectrometers, Detectors and Associated Equipment 486.1-2, pp. 35–39. DOI: 10.1016/S0168-9002(02)00671-X.
- Grazioso, R., N. Zhang, J. Corbeil, M. Schmand, R. Ladebeck, M. Vester, G. Schnur, W. Renz, and H. Fischer (2006). 'APD-based PET detector for simultaneous PET/MR imaging'. In: Nuclear Instruments and Methods in Physics Research, Section A: Accelerators, Spectrometers, Detectors and Associated Equipment 569.2, pp. 301–305. DOI: 10.1016/j.nima.2006.08.121.
- Hong, K. J., Y. Choi, J. H. Jung, J. Kang, W. Hu, H. K. Lim, Y. Huh, S. Kim, J. W. Jung, K. B. Kim, M. S. Song, and H.-w. Park (2013). 'A prototype MR insertable brain PET using tileable GAPD arrays'. In: *Medical Physics* 40.4, p. 042503. DOI: 10.1118/1.4793754.
- Hong, S. J., H. G. Kang, G. B. Ko, I. C. Song, J.-T. Rhee, and J. S. Lee (2012). 'SiPM-PET with a short optical fiber bundle for simultaneous PET-MR imaging.' In: *Physics* in Medicine and Biology 57.12, pp. 3869–83. DOI: 10.1088/0031-9155/57/12/3869.
- Ito, M., J. S. Lee, S. I. Kwon, G. S. Lee, B. Hong, K. S. Lee, K.-S. Sim, S. J. Lee, J. T. Rhee, and S. J. Hong (2010). 'A Four-Layer DOI Detector With a Relative Offset for Use in an Animal PET System'. In: *IEEE Transactions on Nuclear Science* 57.3, pp. 976–981. DOI: 10.1109/TNS.2010.2044892.
- James, S. S., Y. Yang, Y. Wu, R. Farrell, P. Dokhale, K. S. Shah, and S. R. Cherry (2009). 'Experimental characterization and system simulations of depth of interaction PET detectors using 0.5 mm and 0.7 mm LSO arrays'. In: *Physics in Medicine and Biology* 54.14, pp. 4605–4619. DOI: 10.1088/0031-9155/54/14/015.
- Jan, S., D. Benoit, E. Becheva, T. Carlier, F. Cassol, P. Descourt, T. Frisson, L. Grevillot, L. Guigues, L. Maigne, C. Morel, Y. Perrot, N. Rehfeld, D. Sarrut, D. R. Schaart, S. Stute, U. Pietrzyk, D. Visvikis, N. Zahra, and I. Buvat (2011). 'GATE V6: a major enhancement of the GATE simulation platform enabling modelling of CT and radiotherapy'. In: *Physics in Medicine and Biology* 56.4, pp. 881–901. DOI: 10.1088/0031– 9155/56/4/001.
- Jan, S. et al. (2004). 'GATE: a simulation toolkit for PET and SPECT'. In: Physics in Medicine and Biology 49.19, pp. 4543–4561. DOI: 10.1088/0031-9155/49/19/007.
- Janecek, M. and W. W. Moses (2008). 'Measuring light reflectance of BGO crystal surfaces'. In: *IEEE Transactions on Nuclear Science* 55.5, pp. 2443–2449. DOI: 10. 1109/TNS.2008.2003253.
- Janecek, M. and W. W. Moses (2010). 'Simulating Scintillator Light Collection Using Measured Optical Reflectance'. In: *IEEE Transactions on Nuclear Science* 57.3, pp. 964–970. DOI: 10.1109/TNS.2010.2042731.

- Judenhofer, M. S., C. Catana, B. K. Swann, S. B. Siegel, W.-I. Jung, R. E. Nutt, S. R. Cherry, C. D. Claussen, and B. J. Pichler (2007). 'PET/MR images acquired with a compact MR-compatible PET detector in a 7-T magnet.' In: *Radiology* 244.3, pp. 807–814. DOI: 10.1148/radiol.2443061756.
- Kapłon, Ł. et al. (2014). 'Plastic scintillators for positron emission tomography obtained by the bulk polymerization method'. In: *Bio-Algorithms and Med-Systems* 10.1, pp. 27–31. DOI: 10.1515/bams-2013-0108.
- Kolb, A., H. F. Wehrl, M. Hofmann, M. S. Judenhofer, L. Eriksson, R. Ladebeck, M. P. Lichy, L. Byars, C. Michel, H. P. Schlemmer, M. Schmand, C. D. Claussen, V. Sossi, and B. J. Pichler (2012). 'Technical performance evaluation of a human brain PET/MRI system'. In: *European Radiology* 22.8, pp. 1776–1788. DOI: 10. 1007/s00330-012-2415-4.
- Laan, D. J. J. van der, D. R. Schaart, M. C. Maas, F. J. Beekman, P. Bruyndonckx, and C. W. E. van Eijk (2010). 'Optical simulation of monolithic scintillator detectors using GATE/GEANT4.' In: *Physics in Medicine and Biology* 55.6, pp. 1659–75. DOI: 10.1088/0031-9155/55/6/009.
- Lee, M. S. and J. S. Lee (2015). 'Depth-of-interaction measurement in a single-layer crystal array with a single-ended readout using digital silicon photomultiplier'. In: *Physics in Medicine and Biology* 60.16, pp. 6495–6514. DOI: 10.1088/0031-9155/ 60/16/6495.
- Lerche, C., J. Benlloch, F. Sanchez, N. Pavon, B. Escat, E. Gimenez, M. Fernandez, I. Torres, M. Gimenez, A. Sebastia, and J. Martinez (2005). 'Depth of  $\gamma$ -ray interaction within continuous crystals from the width of its scintillation light-distribution'. In: *IEEE Transactions on Nuclear Science* 52.3, pp. 560–572. DOI: 10.1109/TNS.2005. 851424.
- Levin, a. and C. Moisan (1996). 'A more physical approach to model the surface treatment of scintillation counters and its implementation into DETECT'. In: *IEEE Nuclear Science Symposium*. Vol. 2, pp. 702–706. DOI: 10.1109/NSSMIC.1996.591410.
- Li, C., S. Wang, L. Huo, Y. Wang, K. Liang, R. Yang, and D. Han (2014). 'Position Sensitive Silicon Photomultiplier With Intrinsic Continuous Cap Resistive Layer'. In: *IEEE Transactions on Electron Devices* 61.9, pp. 3229–3232. DOI: 10.1109/TED. 2014.2336171.
- Liu, H., T. Omura, M. Watanabe, and T. Yamashita (2001). 'Development of a depth of interaction detector for γ-rays'. In: Nuclear Instruments and Methods in Physics Research Section A: Accelerators, Spectrometers, Detectors and Associated Equipment 459.1-2, pp. 182–190. DOI: 10.1016/S0168-9002(00)00939-6.
- Maas, M. C., D. R. Schaart, D. J. J. van der Laan, P. Bruyndonckx, C. Lemaître, F. J. Beekman, and C. W. E. van Eijk (2009). 'Monolithic scintillator PET detectors with intrinsic depth-of-interaction correction'. In: *Physics in Medicine and Biology* 54.7, pp. 1893–1908. DOI: 10.1088/0031-9155/54/7/003.

- Maramraju, S. H., S. D. Smith, S. Rescia, S. Stoll, M. Budassi, P. Bhadrecha, B. Ravindranath, P. Vaska, C. Woody, and D. Schlyer (2012). 'Evaluation of cross-modality electromagnetic interactions in a shielded PET/MRI system'. In: *IEEE Nuclear Science Symposium and Medical Imaging Conference (NSS/MIC)*, pp. 2500–2505. DOI: 10.1109/NSSMIC.2011.6152677.
- Maramraju, S. H., S. D. Smith, S. S. Junnarkar, D. Schulz, S. Stoll, B. Ravindranath, M. L. Purschke, S. Rescia, S. Southekal, J.-F. Pratte, P. Vaska, C. L. Woody, and D. J. Schlyer (2011). 'Small animal simultaneous PET/MRI: initial experiences in a 9.4 T microMRI.' In: *Physics in Medicine and Biology* 56.8, pp. 2459–80. DOI: 10.1088/0031-9155/56/8/009.
- McElroy, D., W. Pimpl, B. Pichler, M. Rafecas, T. Schuler, and S. Ziegler (2005). 'Characterization and readout of MADPET-II detector modules: validation of a unique design concept for high resolution small animal PET'. In: *IEEE Transactions on Nuclear Science* 52.1, pp. 199–204. DOI: 10.1109/TNS.2004.843114.
- Melcher, C. L. (2000). 'Scintillation crystals for PET.' In: Journal of Nuclear Medicine 41.6, pp. 1051–1055.
- Melcher, C. and J. Schweitzer (1992). 'Cerium-doped lutetium oxyorthosilicate: a fast, efficient new scintillator'. In: *IEEE Transactions on Nuclear Science* 39.4, pp. 502– 505. DOI: 10.1109/23.159655.
- Miyaoka, R. S., X. Li, W. C. Hunter, and T. K. Lewellen (2011). 'A trapezoidal slat crystal (TSC) PET detector'. In: *IEEE Nuclear Science Symposium*. IEEE, pp. 3665– 3668. DOI: 10.1109/NSSMIC.2011.6153691.
- Moehrs, S., A. Del Guerra, D. J. Herbert, and M. a. Mandelkern (2006). 'A detector head design for small-animal PET with silicon photomultipliers (SiPM).' In: *Physics* in Medicine and Biology 51.5, pp. 1113–27. DOI: 10.1088/0031-9155/51/5/004.
- Moses, W. W. (2011). 'Fundamental Limits of Spatial Resolution in PET.' In: Nuclear instruments & methods in physics research. Section A, Accelerators, spectrometers, detectors and associated equipment 648 Supple, S236–S240. DOI: 10.1016/j.nima. 2010.11.092.
- Nishikido, F., N. Inadama, E. Yoshida, H. Murayama, and T. Yamaya (2013). 'Fourlayer DOI PET detectors using a multi-pixel photon counter array and light sharing method'. In: Nuclear Instruments and Methods in Physics Research Section A: Accelerators, Spectrometers, Detectors and Associated Equipment. DOI: 10.1016/j.nima. 2013.08.031.
- Okumura, S., S. Yamamoto, H. Watabe, N. Kato, and H. Hamamura (2015). 'Development of dual-layer GSO depth-of-interaction block detector using angled optical fiber'. In: Nuclear Instruments and Methods in Physics Research Section A: Accelerators, Spectrometers, Detectors and Associated Equipment 781, pp. 65–70. DOI: 10.1016/j.nima.2015.01.102.

- Olcott, P., E. Kim, K. Hong, B. J. Lee, A. M. Grant, C.-M. Chang, G. Glover, and C. S. Levin (2015). 'Prototype positron emission tomography insert with electrooptical signal transmission for simultaneous operation with MRI'. In: *Physics in Medicine and Biology* 60.9, pp. 3459–3478. DOI: 10.1088/0031-9155/60/9/3459.
- Peng, B. J., Y. Wu, S. R. Cherry, and J. H. Walton (2014). 'New shielding configurations for a simultaneous PET/MRI scanner at 7T'. In: *Journal of Magnetic Resonance* 239, pp. 50–56. DOI: 10.1016/j.jmr.2013.10.027.
- Peng, B. J. (2011). 'Studies of the Interactions of the MRI System with the PET Insert and Deriving MRI-based Attenuation Map for PET Image Reconstruction'. PhD thesis. UC Davis.
- Phelps, M. E., E. J. Hoffman, N. a. Mullani, and M. M. Ter-Pogossian (1975). 'Application of annihilation coincidence detection to transaxial reconstruction tomography.' In: Journal of Nuclear Medicine 16.3, pp. 210–224.
- Pichler, B., E. Lorenz, R. Mirzoyan, W. Pimpl, F. Roder, M. Schwaiger, and S. Ziegler (1997). 'Performance test of a LSO-APD PET module in a 9.4 Tesla magnet'. In: *IEEE Nuclear Science Symposium*, pp. 1237–1239. DOI: 10.1109/NSSMIC.1997.670533.
- Pichler, B. J., M. S. Judenhofer, C. Catana, J. H. Walton, M. Kneilling, R. E. Nutt, S. B. Siegel, C. D. Claussen, and S. R. Cherry (2006). 'Performance Test of an LSO-APD Detector in a 7-T MRI Scanner for Simultaneous PET/MRI'. In: *Journal of Nuclear Medicine* 47.4, pp. 639–647.
- Poole, M., R. Bowtell, D. Green, S. Pittard, A. Lucas, R. Hawkes, and A. Carpenter (2009). 'Split gradient coils for simultaneous PET-MRI.' In: *Magnetic Resonance in Medicine* 62.5, pp. 1106–11. DOI: 10.1002/mrm.22143.
- Roncali, E. and S. R. Cherry (2013). 'Simulation of light transport in scintillators based on 3D characterization of crystal surfaces'. In: *Physics in Medicine and Biology* 58.7, pp. 2185–2198. DOI: 10.1088/0031-9155/58/7/2185.
- Roncali, E., J. E. Phipps, L. Marcu, and S. R. Cherry (2012). 'Pulse shape discrimination and classification methods for continuous depth of interaction encoding PET detectors.' In: *Physics in Medicine and Biology* 57.20, pp. 6571–85. DOI: 10.1088/0031– 9155/57/20/6571.
- Roncali, E., J. P. Schmall, V. Viswanath, E. Berg, and S. R. Cherry (2014). 'Predicting the timing properties of phosphor-coated scintillators using Monte Carlo light transport simulation.' In: *Physics in Medicine and Biology* 59, pp. 2023–39. DOI: 10.1088/0031-9155/59/8/2023.
- Rothfuss, H., M. Casey, M. Conti, N. Doshi, L. Eriksson, and M. Schmand (2004).
  'Monte Carlo simulation study of LSO crystals'. In: *IEEE Transactions on Nuclear Science* 51.3, pp. 770–774. DOI: 10.1109/TNS.2004.829753.
- Schaart, D. R., S. Seifert, R. Vinke, H. T. van Dam, P. Dendooven, H. Löhner, and F. J. Beekman (2010). 'LaBr(3):Ce and SiPMs for time-of-flight PET: achieving 100

ps coincidence resolving time.' In: *Physics in Medicine and Biology* 55.7, N179–N189. DOI: 10.1088/0031-9155/55/7/N02.

Schelkunoff, S. A. (1943). Electromagnetic Waves. D. Van Nostrad Company Inc.

- Schenck, J. F. (1996). 'The role of magnetic susceptibility in magnetic resonance imaging: MRI magnetic compatibility of the first and second kinds.' In: *Medical Physics* 23.6, pp. 815–850. DOI: 10.1118/1.597854.
- Schlyer, D., P. Vaska, D. Tomasi, C. Woody, S. H. Maramraju, S. Southekal, J. F. Pratte, S. Junnarkar, S. Solis-Najera, S. Krishnamoorthy, A. Kriplani, and S. Stoll (2007). 'A simultaneous PET/MRI scanner based on RatCAP in small animals'. In: *IEEE Nuclear Science Symposium Conference Record.* Vol. 5, pp. 3256–3259. DOI: 10.1109/NSSMIC.2007.4436833.
- Schmall, J. P., J. Du, Y. Yang, P. a. Dokhale, M. McClish, J. Christian, K. S. Shah, and S. R. Cherry (2012). 'Comparison of large-area position-sensitive solid-state photomultipliers for small animal PET.' In: *Physics in Medicine and Biologyedicine and biology* 57.24, pp. 8119–34. DOI: 10.1088/0031-9155/57/24/8119.
- Schmall, J. P., E. Roncali, E. Berg, V. Viswanath, J. Du, and S. R. Cherry (2014). 'Timing properties of phosphor-coated polished LSO crystals'. In: *Physics in Medicine and Biology* 59.15, N139–51. DOI: 10.1088/0031-9155/59/15/N139.
- Schug, D., J. Wehner, P. M. Dueppenbecker, B. Weissler, P. Gebhardt, B. Goldschmidt, A. Salomon, F. Kiessling, and V. Schulz (2015a). 'PET performance and MRI compatibility evaluation of a digital, ToF-capable PET/MRI insert equipped with clinical scintillators'. In: *Physics in Medicine and Biology* 60.18, pp. 7045–7067. DOI: 10.1088/0031-9155/60/18/7045.
- Schug, D., J. Wehner, P. M. Dueppenbecker, B. Weissler, P. Gebhardt, B. Goldschmidt, T. Solf, F. Kiessling, and V. Schulz (2015b). 'ToF Performance Evaluation of PET Modules With Digital Silicon Photomultiplier Technology During MR Operation'. In: *IEEE Transactions on Nuclear Science* PP.99, pp. 1–1. DOI: 10.1109/TNS.2015. 2396295.
- Schug, D., J. Wehner, B. Goldschmidt, C. Lerche, P. M. Dueppenbecker, P. Hallen, B. Weissler, P. Gebhardt, F. Kiessling, and V. Schulz (2015c). 'Data Processing for a High Resolution Preclinical PET Detector Based on Philips DPC Digital SiPMs'. In: *IEEE Transactions on Nuclear Science* PP.99, pp. 1–10. DOI: 10.1109/TNS.2015. 2420578.
- Schulz, R. B., V. C. Plantz, and D. R. Brush (1988). 'Shielding theory and practice.' In: *IEEE Transactions on Electromagnetic Compatibility* 30.3, pp. 187–201. DOI: 10. 1109/15.3297.
- Schulz, V., Y. Berker, A. Berneking, N. Omidvari, F. Kiessling, A. Gola, and C. Piemonte (2013). 'Sensitivity encoded silicon photomultiplier-a new sensor for high-resolution PET-MRI.' In: *Physics in Medicine and Biology* 58.14, pp. 4733– 4748. DOI: 10.1088/0031-9155/58/14/4733.

- Schulz, V., B. Weissler, P. Gebhardt, T. Solf, C. W. Lerche, P. Fischer, M. Ritzert, V. Mlotok, C. Piemonte, B. Goldschmidt, S. Vandenberghe, A. Salomon, T. Schaeffter, and P. K. Marsden (2012). 'SiPM based preclinical PET/MR insert for a human 3T MR: First imaging experiments'. In: *IEEE Nuclear Science Symposium and Medical Imaging Conference (NSS/MIC)*, pp. 4467–4469. DOI: 10.1109/NSSMIC. 2011.6152496.
- Seidel, J., J. Vaquero, S. Siegel, W. Gandler, and M. Green (1999). 'Depth identification accuracy of a three layer phoswich PET detector module'. In: *IEEE Transactions on Nuclear Science* 46.3, pp. 485–490. DOI: 10.1109/23.775567.
- Sempere Roldan, P., E. Chereul, O. Dietzel, L. Magnier, C. Pautrot, L. Rbah, D. Sappey-Marinier, A. Wagner, L. Zimmer, M. Janier, V. Tarazona, and G. Dietzel (2007). 'Raytest ClearPET<sup>TM</sup>, a new generation small animal PET scanner'. In: Nuclear Instruments and Methods in Physics Research Section A: Accelerators, Spectrometers, Detectors and Associated Equipment 571.1-2, pp. 498–501. DOI: 10.1016/j.nima.2006.10.143.
- Shao, Y., S. R. Cherry, K. Farahani, K. Meadors, S. Siegel, R. W. Silverman, and P. K. Marsden (1997). 'Simultaneous PET and MR imaging.' In: *Physics in medicine* and biology 42.10, pp. 1965–1970. DOI: 10.1088/0031-9155/42/10/010.
- Shao, Y. S. Y., S. R. Cherry, S. Siegel, and R. W. Silverman (1996). 'A study of intercrystal scatter in small scintillator arrays designed for high resolution PET imaging'. In: *IEEE Transactions on Nuclear Science* 43.3, pp. 1938–1944. DOI: 10.1109/23. 507250.
- Shaw, N. R., R. E. Ansorge, and T. A. Carpenter (2005). 'Commissioning and Testing of Split Coil MRI System for Combined PET-MR'. In: *Proc. Intl. Soc. Mag. Reson* . *Med.* 13 (2005) 13.4, pp. 2005–2005.
- Slates, R. B., K. Farahani, Y. Shao, P. K. Marsden, J. Taylor, P. E. Summers, S. Williams, J. Beech, and S. R. Cherry (1999a). 'A study of artefacts in simultaneous PET and MR imaging using a prototype MR compatible PET scanner'. In: *Physics in Medicine and Biology* 44.8, pp. 2015–2027. DOI: 10.1088/0031-9155/44/8/312.
- Slates, R., S. Cherry, A. Boutefnouchet, Y. Shao, M. Dahlbom, and K. Van Farahani (1999b). 'Design of a small animal MR compatible pet scanner'. In: *IEEE Transac*tions on Nuclear Science 46.3, pp. 565–570. DOI: 10.1109/23.775580.
- Spanoudaki, V., D. McElroy, K. Zell, and S. Ziegler (2005). 'Effect of Temperature on the Stability and Performance of an LSO-APD PET Scanner'. In: *IEEE Nuclear Science Symposium Conference Record*. Vol. 5, pp. 3014–3017. DOI: 10.1109/NSSMIC. 2005.1596965.
- Stickel, J., J. Qi, and S. Cherry (2007). 'Fabrication and characterization of a 0.5-mm lutetium oxyorthosilicate detector array for high-resolution PET applications'. In: *Journal of Nuclear Medicine*, pp. 115–121.

- Stortz, G., C. J. Thompson, F. Retiere, A. L. Goertzen, P. Kozlowski, E. Shams, J. D. Thiessen, M. D. Walker, and V. Sossi (2015). 'Characterization of a Small Animal PET Detector Block Incorporating a Digital Photon Counter Array'. In: *IEEE Transactions on Nuclear Science* 62.3, pp. 1–1. DOI: 10.1109/TNS.2015.2414653.
- Ter-Pogossian, M. M., M. E. Phelps, E. J. Hoffman, and N. a. Mullani (1975). 'A positron-emission transaxial tomograph for nuclear imaging (PETT).' In: *Radiology* 114.1, pp. 89–98. DOI: 10.1148/114.1.89.
- Thoen, H., V. Keereman, P. Mollet, R. Van Holen, and S. Vandenberghe (2013). 'Influence of detector pixel size, TOF resolution and DOI on image quality in MRcompatible whole-body PET'. In: *Physics in Medicine and Biology* 58.18, pp. 6459– 6479. DOI: 10.1088/0031-9155/58/18/6459.
- Thompson, C., G. Stortz, A. Goertzen, E. Berg, F. Retière, P. Kozlowski, L. Ryner, V. Sossi, and X. Zhang (2012). 'Comparison of single and dual layer detector blocks for pre-clinical MRI-PET'. In: Nuclear Instruments and Methods in Physics Research, Section A: Accelerators, Spectrometers, Detectors and Associated Equipment 702, pp. 56–58. DOI: 10.1016/j.nima.2012.07.062.
- Townsend, D. W. (2009). 'Combined PET / CT : the historical perspective'. In: Seminars in Ultrasound, CT, and MRI 29.4, pp. 232-235. DOI: 10.1053/j.sult.2008. 05.006.Combined.
- Vandenberghe, S. and P. K. Marsden (2015). 'PET-MRI: a review of challenges and solutions in the development of integrated multimodality imaging'. In: *Physics in Medicine and Biology* 60, R115–R154. DOI: 10.1088/0031-9155/60/4/R115.
- Vaska, P., A. Bolotnikov, G. Carini, G. Camarda, J. F. Pratte, F. a. Dilmanian, S. J. Park, and R. B. James (2005). 'Studies of CZT for PET applications'. In: *IEEE Nuclear Science Symposium Conference Record* 5, pp. 2799–2802. DOI: 10.1109/ NSSMIC.2005.1596916.
- Wang, Y., J. Seidel, B. M. W. Tsui, J. J. Vaquero, M. G. Pomper, and V. D.-r. S.-a. Pet (2006). 'Performance Evaluation of the GE Healthcare eXplore VISTA Dual-Ring Small-Animal PET Scanner'. In: *Journal of Nuclear Medicine* 47.11, pp. 1891–1900.
- Wehner, J., B. Weissler, P. M. Dueppenbecker, P. Gebhardt, B. Goldschmidt, D. Schug, F. Kiessling, and V. Schulz (2015). 'MR-compatibility assessment of the first preclinical PET-MRI insert equipped with digital silicon photomultipliers.' In: *Physics in Medicine and Biology* 60.6, pp. 2231–2255. DOI: 10.1088/0031-9155/60/6/2231.
- Wehner, J., B. Weissler, P. M. Dueppenbecker, P. Gebhardt, D. Schug, W. Ruetten, F. Kiessling, and V. Schulz (2014). 'PET/MRI insert using digital SiPMs: Investigation of MR-compatibility'. In: Nuclear Instruments and Methods in Physics Research, Section A: Accelerators, Spectrometers, Detectors and Associated Equipment 734, pp. 116–121. DOI: 10.1016/j.nima.2013.08.077.
- Wehrl, H. F., M. Hossain, K. Lankes, C.-C. Liu, I. Bezrukov, P. Martirosian, F. Schick, G. Reischl, and B. J. Pichler (2013). 'Simultaneous PET-MRI reveals brain function

in activated and resting state on metabolic, hemodynamic and multiple temporal scales.' In: *Nature Medicine* 19.9, pp. 1184–9. DOI: 10.1038/nm.3290.

- Weinreb, J. C., R. A. Bell, G. D. Clarke, L. K. Hedges, J. B. Kneeland, and R. R. Price (2004). Magnetic Resonance Imaging (MRI) Quality Control Manual: 2004. American College of Radiology.
- Weissler, B., P. Gebhardt, P. M. Dueppenbecker, J. Wehner, D. Schug, C. W. Lerche, B. Goldschmidt, A. Salomon, I. Verel, E. Heijman, M. Perkuhn, D. Heberling, R. M. Botnar, F. Kiessling, and V. Schulz (2015). 'A Digital Preclinical PET/MRI Insert and Initial Results'. In: *IEEE Transactions on Medical Imaging* 34.11, pp. 2258–2270. DOI: 10.1109/TMI.2015.2427993.
- Weissler, B., P. Gebhardt, C. W. Lerche, J. Wehner, T. Solf, B. Goldschmidt, J. E. Mackewn, P. K. Marsden, F. Kiessling, M. Perkuhn, D. Heberling, and V. Schulz (2014). 'MR compatibility aspects of a silicon photomultiplier-based PET/RF insert with integrated digitisation.' In: *Physics in Medicine and Biology* 59.17, pp. 5119–39. DOI: 10.1088/0031-9155/59/17/5119.
- Weissler, B., P. Gebhardt, P. M. Dueppenbecker, B. Goldschmidt, A. Salomon, D. Schug, J. Wehner, C. Lerche, D. Wirtz, W. Renz, K. Schumacher, B. Zwaans, P. Marsden, F. Kiessling, and V. Schulz (2012a). 'Design concept of world's first preclinical PET/MR insert with fully digital silicon photomultiplier technology'. In: *IEEE Nuclear Science Symposium and Medical Imaging Conference*. IEEE, pp. 2113–2116. DOI: 10.1109/NSSMIC.2012.6551484.
- Weissler, B., P. Gebhardt, M. Zinke, F. Kiessling, and V. Schulz (2012b). 'An MR-compatible singles detection and processing unit for simultaneous preclinical PET/MR'. In: *IEEE Nuclear Science Symposium and Medical Imaging Conference*, pp. 2759–2761. DOI: 10.1109/NSSMIC.2012.6551628.
- Wu, S., G. Zhou, and M. Gu (2007). 'Synthesis of high refractive index composites for photonic applications'. In: *Optical Materials* 29.12, pp. 1793–1797. DOI: 10.1016/j. optmat.2006.10.002.
- Wu, Y., C. Catana, R. Farrell, P. a. Dokhale, K. S. Shah, J. Qi, and S. R. Cherry (2009). 'PET Performance Evaluation of an MR-Compatible PET Insert.' In: *IEEE Transactions on Nuclear Scienceuclear science* 56.3, pp. 574–580. DOI: 10.1109/TNS. 2009.2015448.
- Xiaoli Li, W. C. J. Hunter, T. K. Lewellen, and R. S. Miyaoka (2010). 'Design of a trapezoidal slat crystal (TSC) PET detector for small animal PET/MR imaging'. In: *IEEE Nuclear Science Symposuim and Medical Imaging Conference*. IEEE, pp. 2598– 2601. DOI: 10.1109/NSSMIC.2010.5874258.
- Yamamoto, S., K. Kuroda, and M. Senda (2003). 'Scintillator selection for MRcompatible gamma detectors'. In: *IEEE Transactions on Nuclear Science* 50.5, pp. 1683–1685. DOI: 10.1109/TNS.2003.817375.

- Yamamoto, S., T. Watabe, H. Watabe, M. Aoki, E. Sugiyama, M. Imaizumi, Y. Kanai, E. Shimosegawa, and J. Hatazawa (2012). 'Simultaneous imaging using Si-PM-based PET and MRI for development of an integrated PET/MRI system.' In: *Physics in Medicine and Biology* 57.2, N1–13. DOI: 10.1088/0031-9155/57/2/N1.
- Yang, Y., S. S. James, Y. Wu, H. Du, J. Qi, R. Farrell, P. A. Dokhale, K. S. Shah, K. Vaigneur, and S. R. Cherry (2011). 'Tapered LSO arrays for small animal PET'. In: *Physics in Medicine and Biology* 56.1, pp. 139–153. DOI: 10.1088/0031-9155/ 56/1/009.
- Yang, Y., J. Qi, Y. Wu, S. St James, R. Farrell, P. a. Dokhale, K. S. Shah, and S. R. Cherry (2009a). 'Depth of interaction calibration for PET detectors with dual-ended readout by PSAPDs'. In: *Physics in Medicine and Biology* 54.2, pp. 433–445. DOI: 10.1088/0031-9155/54/2/017.
- Yang, Y., Y. Wu, and S. R. Cherry (2009b). 'Investigation of Depth of Interaction Encoding for a Pixelated LSO Array With a Single Multi-Channel PMT'. In: *IEEE Transactions on Nuclear Science* 56.5, pp. 2594–2599. DOI: 10.1109/TNS.2009. 2016094.
- Yoon, H. S., G. B. Ko, S. I. Kwon, C. M. Lee, M. Ito, I. Chan Song, D. S. Lee, S. J. Hong, and J. S. Lee (2012). 'Initial Results of Simultaneous PET/MRI Experiments with an MRI-Compatible Silicon Photomultiplier PET Scanner'. In: *Journal of Nuclear Medicine* 53.4, pp. 608–614. DOI: 10.2967/jnumed.111.097501.